U.S. DEPARTMENT OF COMMERCE
National Technical Information Service

PB-276 633

Application of High-Gradient Magnetic Separation to Fine Particle Control

Research Triangle Inst, Research Triangle Park, N C

Prepared for

Industrial Environmental Research Lab, Research Triangle Park, N C

Nov 77

EPA-600/2-77-230
November 1977

PB 276 633

Environmental Protection Technology Series

APPLICATION OF HIGH-GRADIENT MAGNETIC SEPARATION TO FINE PARTICLE CONTROL

UNITED STATES ENVIRONMENTAL PROTECTION AGENCY

REPRODUCED BY
NATIONAL TECHNICAL
INFORMATION SERVICE
U. S. DEPARTMENT OF COMMERCE
SPRINGFIELD, VA. 22161

RESEARCH REPORTING SERIES

Research reports of the Office of Research and Development, U.S. Environmental Protection Agency, have been grouped into five series. These five broad categories were established to facilitate further development and application of environmental technology. Elimination of traditional grouping was consciously planned to foster technology transfer and a maximum interface in related fields. The five series are:

1. Environmental Health Effects Research
2. Environmental Protection Technology
3. Ecological Research
4. Environmental Monitoring
5. Socioeconomic Environmental Studies

This report has been assigned to the ENVIRONMENTAL PROTECTION TECHNOLOGY series. This series describes research performed to develop and demonstrate instrumentation, equipment, and methodology to repair or prevent environmental degradation from point and non-point sources of pollution. This work provides the new or improved technology required for the control and treatment of pollution sources to meet environmental quality standards.

EPA REVIEW NOTICE

This report has been reviewed by the U.S. Environmental Protection Agency, and approved for publication. Approval does not signify that the contents necessarily reflect the views and policy of the Agency, nor does mention of trade names or commercial products constitute endorsement or recommendation for use.

This document is available to the public through the National Technical Information Service, Springfield, Virginia 22161.

TECHNICAL REPORT DATA
(Please read Instructions on the reverse before completing)

1. REPORT NO. EPA-600/2-77-230	2.	3. RECIPIENT'S ACCESSION NO. PB276633
4. TITLE AND SUBTITLE Application of High-Gradient Magnetic Separation to Fine Particle Control		5. REPORT DATE November 1977
		6. PERFORMING ORGANIZATION CODE
7. AUTHOR(S) C. H. Gooding, T. W. Sigmon, and L. K. Monteith		8. PERFORMING ORGANIZATION REPORT NO.
9. PERFORMING ORGANIZATION NAME AND ADDRESS Research Triangle Institute P.O. Box 12194 Research Triangle Park, North Carolina 27709		10. PROGRAM ELEMENT NO. 1AB012; ROAP 21ADL-029
		11. CONTRACT/GRANT NO. 68-02-1879
12. SPONSORING AGENCY NAME AND ADDRESS EPA, Office of Research and Development Industrial Environmental Research Laboratory Research Triangle Park, NC 27711		13. TYPE OF REPORT AND PERIOD COVERED Final; 6/75-8/77
		14. SPONSORING AGENCY CODE EPA/600/13

15. SUPPLEMENTARY NOTES IERL-RTP project officer for this report is Dennis C. Drehmel, Mail Drop 61, 919/541-2925.

16. ABSTRACT The report gives results of an assessment of the potential use of high-gradient magnetic separation (HGMS) as a means of collecting gas stream particulates. The assessment included both experiments and analyses of theoretical models. Phase I included evaluations of theoretical explanations of HGMS and published reports of liquid system applications. A bench-scale apparatus was constructed, and HGMS experiments were conducted using redispersed dust from a basic oxygen furnace. High efficiency collection of fine particulates was achieved with both high throughput and reasonable projected energy rqeuirements relative to conventional devices. In Phase II, experiments were scaled up to 0.8 cu m/s (1700 CFM). Dusts from basic oxygen and electric arc furnaces were redispersed and collected. Results show that submicron particles can be collected with 90-plus % efficiency using applied magnetic flux densities of 0.2-0.4 T. With superficial gas velocities up to 11 m/s, the pressure drop across the HGMS device was typically less than 1.5 kPa (6 in. H2O). Even lower fields can be used successfully at the expense of higher pressure drop or reduced throughput.

17. KEY WORDS AND DOCUMENT ANALYSIS

a. DESCRIPTORS	b. IDENTIFIERS/OPEN ENDED TERMS	c. COSATI Field/Group
Air Pollution Dust Magnetic Separators	Air Pollution Control Stationary Sources Particulate High-gradient Magnetic Separation	13B 11G

18. DISTRIBUTION STATEMENT Unlimited	19. SECURITY CLASS *(This Report)* Unclassified	21. NO. OF PAGES 153
	20. SECURITY CLASS *(This page)* Unclassified	22. PRICE PC A08 - A01

EPA Form 2220-1 (9-73)

DISCLAIMER

This report has been reviewed by the Industrial Environmental Research Laboratory, U.S. Environmental Protection Agency, and approved for publication. Approval does not signify that the contents necessarily reflect the views and policies of the U.S. Environmental Protection Agency, nor does mention of trade names or commercial products constitute endorsement or recommendation for use.

EPA-600/2-77-230
November 1977

APPLICATION OF HIGH-GRADIENT MAGNETIC SEPARATION TO FINE PARTICLE CONTROL

by

C.H. Gooding, T.W. Sigmon, and L.K. Monteith

Research Triangle Institute
P.O. Box 12194
Research Triangle Park, N.C. 27709

Contract No. 68-02-1879
ROAP No. 21ADL-029
Program Element No. 1AB012

EPA Project Officer: Dennis C. Drehmel

Industrial Environmental Research Laboratory
Office of Energy, Minerals, and Industry
Research Triangle Park, N.C. 27711

Prepared for

U.S. ENVIRONMENTAL PROTECTION AGENCY
Office of Research and Development
Washington, D.C. 20460

1a

ABSTRACT

Experiments were conducted and theoretical models were analyzed to assess the potential use of high gradient magnetic separation (HGMS) as a means of collecting gas stream particulates.

Viable alternatives to the conventional particulate collection technologies are continually being sought to improve the efficiency and reduce the cost of fine particle emission control. HGMS has been demonstrated in prior research and commercial applications to be an effective and economical method of removing small paramagnetic particles from selected liquid process streams.

In Phase I of this study existing theoretical explanations of HGMS and published reports of liquid-system applications were evaluated. A bench-scale apparatus was constructed, and HGMS experiments were conducted using redispersed dust from a basic oxygen furnace. High-efficiency collection of fine particles was achieved with a high throughput and with reasonable projected energy requirements relative to conventional devices.

In Phase II the experiments were scaled up to a 0.8 m^3/s (1700 CFM) capacity unit. Dusts from basic oxygen and electric arc furnaces were redispersed and collected. The results show that submicron particles can be collected with greater than 90 percent efficiency using applied magnetic flux densities of 0.2 to 0.4 T. With superficial gas velocities up to 11 m/s, the pressure drop across the HGMS device was typically less than 1.5 kPa (6 in. H_2O). Even lower fields can be used successfully at the expense of higher pressure drop or reduced throughput.

A theoretical model was utilized to correlate the experimental data and to evaluate the economic and collection-efficiency trade-offs associated with operating parameter variations. The analysis indicates that HGMS has a good potential for successful application to selected full-scale fine particulate emission sources with reasonable capital and operating costs.

This report is submitted in fulfillment of Contract No. 68-02-1879 by Research Triangle Institute under the sponsorship of the U. S. Environmental Protection Agency. The report covers the period June 30, 1975 to August 29, 1977, and work was completed as of September 29, 1977.

CONTENTS

Page

Abstract.. ii

Figures... vi

Tables.. ix

Acknowledgments x

SECTION

1. Introduction and Summary........................... 1
2. Conclusions.. 3
3. Recommendations 5
4. Background Development............................. 7
   - Basic concept of the process.................... 7
   - HGMS development and experience.................. 9
   - Theoretical aspects of the process............... 12
   - Potential applications of HGMS to fine particle emission control.................... 33
5. Experimental Work.................................. 35
   - Basis of experiment design....................... 35
   - Summary of Phase I experiments and results...... 37
   - Description of Phase II apparatus and experiments............................ 48
6. Pilot-Scale Experimental Results................... 59
   - Supportive matrix and particle data.............. 59
   - Comparison of results with theoretical models... 65
   - Discussion of individual parameter effects...... 89
   - Operating difficulties........................... 99
7. Economic Comparison of HGMS and Conventional Control Technology.............................. 103
   - Basis of economic comparison..................... 103
   - Cost and energy estimates for conventional technology.................................. 104

Page

Cost and energy estimates for HGMS.............. 105
Comparison of HGMS and conventional technology.................................. 111
9. References... 115
10. Bibliography... 123
Appendix... 125

FIGURES

Number		Page
1	Schematic representation of a high gradient magnetic separator	8
2	Critical trajectory of particle impacting on a cylindrical collector	14
3	Inertial impaction efficiency as a function of Stokes number in potential flow	15
4	Interception efficiency in potential flow	16
5	Geometric basis of HGMS trajectory model	18
6	Magnetic force contours around a ferromagnetic cylinder oriented perpendicular to the magnetic field	20
7	Dimensionless capture radius from Watson's trajectory model	22
8	Lines of constant capture radius with inertial forces included	27
9	Force balance on collected particle with no magnetic field	28
10	Differential matrix segment	32
11	Experimental apparatus used in preliminary HGMS experiments	38
12	Results of bench-scale HGMS tests with packing density of 0.0088	42
13	Results of bench-scale HGMS tests with packing density of 0.0132	43
14	Results of bench-scale HGMS tests with packing density of 0.0174	44
15	Bench-scale variation in collection efficiency and pressure drop with matrix loading	46
16	Schematic representation of pilot-scale HGMS facility	51
17	HGMS matrix construction and cleaning apparatus	53
18	Photomicrographs of stainless steel wool matrix fibers	60
19	Photomicrographs of stainless steel wool matrix fibers	61
20	Photomicrographs of stainless steel wool matrix fibers	62
21	Magnetization curves of steel wool material and in-situ matrix	64

Figures (continued)

Number		Page
22	Magnetization curve of basic oxygen furnace dust.......	66
23	Magnetization curve of electric arc furnace dust.......	67
24	Zero-field pilot-scale results with BOF dust (F=0.005, L=15 cm)..	69
25	Zero-field pilot-scale results with BOF dust (F=0.010, L=15 cm)..	70
26	Zero-field pilot-scale results with BOF dust (F=0.005, L=30 cm)..	71
27	Zero-field pilot-scale results with EAF dust (F=0.005, L=15 cm)..	72
28	Lines of constant capture radius with inertial forces included and A=2.0.................................	74
29	Pilot-scale HGMS results with BOF dust (B_0=0.05 T).....	75
30	Pilot-scale HGMS results with BOF dust (B_0=0.10 T).....	76
31	Pilot-scale HGMS results with BOF dust at elevated temperature..	77
32	Pilot-scale HGMS results with BOF dust (B_0=0.20 T).....	78
33	Pilot-scale HGMS results with BOF dust (F=0.010).......	79
34	Pilot-scale HGMS results with BOF dust (L=30 cm).......	80
35	Pilot-scale HGMS results with BOF dust (duplicates of earlier runs)......................................	81
36	Pilot-scale HGMS results with BOF dust (replicate runs)..	82
37	Pilot-scale HGMS results with EAF dust (B_0=0.10 T).....	83
38	Pilot-scale HGMS results with EAF dust (B_0=0.20 T).....	84
39	Pilot-scale HGMS results with both dusts at B_0=0.40 T..	85
40	Pilot-scale variation in BOF collection efficiency and matrix pressure drop with matrix loading..............	86
41	Pilot-scale variation in EAF collection efficiency and matrix pressure drop with matrix loading..............	87
42	Comparison of collection efficiency results of replicate runs.....................................	90
43	Correlation of matrix pressure drop with gas velocity, matrix packing density and matrix length..............	92

Figures (continued)

Number		Page
44	Experimental effect of matrix length on collection efficiency with and without an applied magnetic field..	94
45	Experimental effect of matrix packing density on collection efficiency with and without an applied field..	95
46	Experimental effect of applied magnetic field on the collection efficiency of both dusts..................	97
47	Illustration of the theoretical effect of increasing gas velocity..................................	98
48	Experimental effects of gas velocity on collection efficiency with and without an applied magnetic field..	100
49	Reported and estimated power requirements for iron-bound solenoids of various configuration.............	108
50	Lines of constant capture radius with inertial forces included and A=1.5................................	110
A-1	Coordinate system for HGMS single-fiber model..........	128

TABLES

Number		Page
1	Potential Applications of HGMS to Fine Particle Emission Control	34
2	Estimated Magnet Power Requirements for Several Field/Velocity Combinations	36
3	Ranges of Operating Parameters - Phase I Experiments	41
4	Preliminary Economic Analysis for HGMS Applied to BOF Dust Control	47
5	Comparison of Pitot Traverse Results	54
6	Experiment Design for Pilot-Scale HGMS	58
7	Values of the Near Field Correction Parameter	63
8	Pooled Statistics on Particle Penetration	91
9	Design and Cost Summary of Conventional BOF Control Equipment	106
10	Cost Estimates for Large Iron-Bound Solenoids Applicable to Fine Particle Control	107
11	Comparison of HGMS and Conventional Technology	112

ACKNOWLEDGMENTS

The authors wish to acknowledge the assistance and support of the following individuals in various segments of this work.

Dr. Dennis C. Drehmel, EPA Project Officer, provided support and direction throughout the project.

Both sources of industrial dust were obtained through the cooperation of Mr. John W. Leming, Jr., Manager of Pollution Abatement of Bethlehem Steel Corporation, Bethlehem, Pa.

Mr. William F. Lawson, Jr., of the USERDA Morgantown Energy Research Center and West Virginia University provided a copy of his unpublished master's thesis. Mr. Lawson's prior theoretical research on HGMS was of critical importance to this work.

Dr. Herbert Hacker, Jr., of Duke University, Durham, N. C. provided experimental determinations of particle and steel wool magnetization.

Mr. R. Duncan Hay of Magnetic Engineering Associates, Cambridge, Mass. made valuable contributions to the Phase I data interpretation and preliminary economic analysis.

Messers. Don Zanders, Billy Bowles, Wally Merritt, and Paul Johnson of Monsanto Research Corporation were very cooperative in providing coordination, operation, and troubleshooting of the EPA wind tunnel utilized in the Phase II experiments.

Other RTI personnel who made major contributions include Dr. Forest O. Mixon, Manager, Process Engineering Department, who provided internal direction as Laboratory Supervisor; Messers. Doug VanOsdell and Martin Lee, who assisted in the design, construction, and operation of the bench-scale apparatus; Mr. Fred Schwarz, who designed and fabricated many components of the sampling equipment for the Phase II experiments; Messers. Bill King, John Sauerbier, and James Armstrong who assisted in the design, construction, and operation of the pilot-scale apparatus.

SECTION 1

INTRODUCTION AND SUMMARY

In the last several years, particulate control technology has been developed to the extent that several methods are now available to control large particle emissions from most industrial sources with an efficiency of greater than 99 percent. Emphasis on particulate control has now shifted toward the fine particle size range, particularly to particles that have diameters between 0.3 and 3 micrometers. These particles are of primary interest because they tend to remain in the atmosphere for long periods of time, thus contributing to atmospheric haze. They also are suspected to be major contributors to numerous air pollution related health problems.

The three major conventional technologies for the control of fine particulate emissions are electrostatic precipitation, wet scrubbing, and fabric filtration. The cost of applying these control methods and the fractional collection efficiency obtained vary according to the specific application. Recent EPA research in particulate emission control has followed two complementary courses: (1) study of the fine particle collection characteristics of the conventional technologies and (2) evaluation of viable alternatives to the conventional technologies. Both of these courses have as their goals the enhancement of fine particulate collection efficiency and the reduction of the capital and operating costs of industrial emission control.

In the last decade research and commercial applications have demonstrated that high gradient magnetic separation (HGMS) is an effective and economical method of removing small paramagnetic particles from selected liquid streams. In Phase I of this study published theoretical and experimental reports of HGMS applications were utilized to evaluate the potential success of the process in removing fine, paramagnetic particles from gas streams. Industrial sources of fine, paramagnetic particles were identified, and the steelmaking basic oxygen furnace (BOF) was selected for initial HGMS evaluation. A bench-scale apparatus was constructed, and HGMS experiments were conducted using redispersed BOF dust. With existing theoretical equations as a guideline, the experimental data were analyzed, and favorable operating conditions were identified. A preliminary economic analysis was made of the full-scale application of HGMS for particulate control on a basic oxygen furnace. The analysis indicated that HGMS could be successfully applied to BOF particulate emission control with reasonable capital cost and energy requirements. Phase I of the study concluded with the design of a pilot-scale apparatus and experimental program to verify and extend the results obtained in the preliminary work.

In Phase II the 0.8 m^3/s (1700 CFM) capacity pilot plant was constructed and operated. A systematic series of experiments was conducted using both BOF dust and dust from an electric arc furnace (EAF). Fractional collection efficiency of BOF dust was measured in conjunction with variations in five important process operating parameters: magnetic field, gas velocity, collection matrix density and length, and gas temperature. A more limited series of tests was run with EAF dust. A theoretical model was utilized to correlate the experimental data and to evaluate the economic and collection efficiency trade-offs associated with operating parameter variations. The economic projections of Phase I were refined, and a comparison was made of the capital cost and energy requirements of HGMS as a particulate control method versus the conventional technologies. Potential design and operating problems of HGMS were also considered.

The following sections of this report present conclusions of the study and recommendations for continued work along with details of the development and theory of the process, a description of the pilot plant used in this work, and the experimental results and analysis.

SECTION 2

CONCLUSIONS

The central purpose of this work was to demonstrate on a small scale the feasibility of applying high gradient magnetic separation to the control of fine particle emissions. Theoretical analysis, bench-scale testing, and pilot-scale testing were conducted, and the following conclusions were drawn.

(1) High gradient magnetic separation has been demonstrated experimentally to be an effective method of collecting submicron particles of relatively high magnetic susceptibility from high-velocity gas streams.

(2) Several industrial processes in the iron and steel industry and the ferroalloy industry produce particulate emissions of sufficiently high magnetic susceptibility to make them potential candidates for the application of HGMS fine particle control.

(3) Preliminary economic analysis based on the pilot-scale HGMS experiments indicates that HGMS could be economically competitive with conventional particulate control technologies. Projected energy requirements for a full-scale application to a basic oxygen furnace are significantly less than those of a comparable electrostatic precipitator and much less than those of a wet scrubber. Projected capital costs based on existing HGMS equipment are somewhat higher than either precipitators or scrubbers. Sufficient data are not currently available on baghouse installations on the candidate processes to allow a comparison of HGMS and this control method.

(4) Current methods of regenerating HGMS collection matrices based on cyclical operation may not be practical in high throughput gas stream systems.

(5) HGMS system designs directed specifically to gas stream applications are needed to reduce projected capital costs and to determine the optimum method of matrix regeneration.

(6) HGMS potentially offers at least two important advantages ver alternate methods of fine particle control. The high gas velocities demonstrated in the pilot-scale experiments indicate much smaller space requirements than either electrostatic precipitators or baghouses, which could lead to a significant reduction in total installed equipment costs. As presently conceived, the process collects the particulate in a dry form and avoids problems with sludge disposal and liquid waste treatment.

(7) An existing theoretical model of the HGMS process provides a valuable tool that can be used to screen potential applications, evaluate alternative system designs, plan experiments, analyze experimental data, and conduct economic analyses.

(8) No inherent health or safety hazards or any other unfavorable environmental impacts are foreseen that might prevent the application of HGMS to fine particle control.

SECTION 3

RECOMMENDATIONS

The successful pilot-scale experiments described in this report indicate a strong potential for the efficient and economically attractive application of HGMS to fine particle control on several industrial processes. Experimental development of the process should be continued to identify the most promising industrial applications and to provide additional data on process performance and economics. To gain the interest and confidence of the industrial community, it is recommended that the next experimental program include pilot-scale field testing of HGMS on a slipstream of one or more industrial processes. To provide flexibility in the choice of field test sites and minimize the cost borne by industrial participants, the pilot plant should be a self-contained relocatable unit. A recommended four-part pilot demonstration is summarized below.

(1) Experiment and System Design

On-site evaluations of candidate sources should be conducted to gather data on the industrial process conditions. Using experimental data and correlations from the work described in this report plus supplemental wind tunnel tests, a relocatable pilot-plant should be designed and constructed. An important part of the equipment design should be the evaluation of alternate magnet systems to determine the configuration most appropriate for a gas stream application. When the equipment design is completed, a compatible plan for the experimental field tests should be drawn up with the concurrence of the industrial participants and the approval of EPA.

(2) Design Verification Tests

Using the pilot plant described in this report, additional tests should be conducted with dusts from candidate sources to select the most promising sources for initial field testing and to assist in the design and material selection for the relocatable pilot-plant. These tests would proceed concurrently with the work recommended in item (1) above. Tests should also be conducted to evaluate alternate matrix materials, configurations, and cleaning methods.

(3) Pilot-Scale Field Demonstration

The relocatable pilot unit should be tested on slipstreams of one or more industrial sources. Tests should be conducted to characterize the performance of HGMS fine particle control with respect to particle source and size; gas humidity, temperature, and velocity; magnetic field strength; and matrix configuration. The performance of the unit under continuous, long-term operation should also be evaluated.

(4) Summary and Conclusions

Using the field data, an analysis of fractional efficiency versus residence time and energy requirements should be performed. Limitations and advantages of the process, problem areas, and safety aspects should also be evaluated. Cost estimates for application of HGMS to the tested industrial sources should be prepared and compared to available data on conventional control technology.

Throughout the recommended project, theoretical and/or semi-empirical modeling of the HGMS process should be continued to aid in experiment design, data interpretation, equipment design and optimization, and process economic evaluation. As a first step in the continued theoretical work, capture radii should be actually calculated (rather than extrapolated from Lawson's work) for conditions that will be incurred in gas stream HGMS applications.

SECTION 4

BACKGROUND DEVELOPMENT

BASIC CONCEPT OF THE PROCESS

Magnetic separation has long been recognized as a method of removing magnetic solids from nonmagnetic solids and fluids. Generally the process has been applied to the removal of relatively large, strongly magnetic solid bodies. The largest commercial application has been the separation of magnetic minerals from ores. Within the last decade a new technique, high gradient magnetic separation (HGMS), has been developed and proven capable of removing very small, weakly magnetic particles from nonmagnetic materials.

The fundamental concept of HGMS is the interaction of the small paramagnetic particles with a ferromagnetic wire in a uniform background magnetic field. The ferromagnetic wire induces regions of highly nonuniform field intensity which results in a net force being exerted on the particles. The magnetic force, in competition with viscous and in some cases inertial and gravitational forces, causes the particles to migrate to the surface of the wire where they are retained until the magnetic force is removed.

In its most simple, practical form, the high gradient magnetic separator consists of a canister packed with fibers of a ferromagnetic material (such as ferritic stainless steel wool) and subjected to a strong external magnetic field (Figure 1). The strong magnetic forces near the edges of the fibers result in very efficient collection of fine paramagnetic particles. Thus the particle-laden fluid is cleansed as it passes through the canister. When the fiber matrix becomes fully loaded, the magnetic field is removed and the particles may be flushed from the matrix.

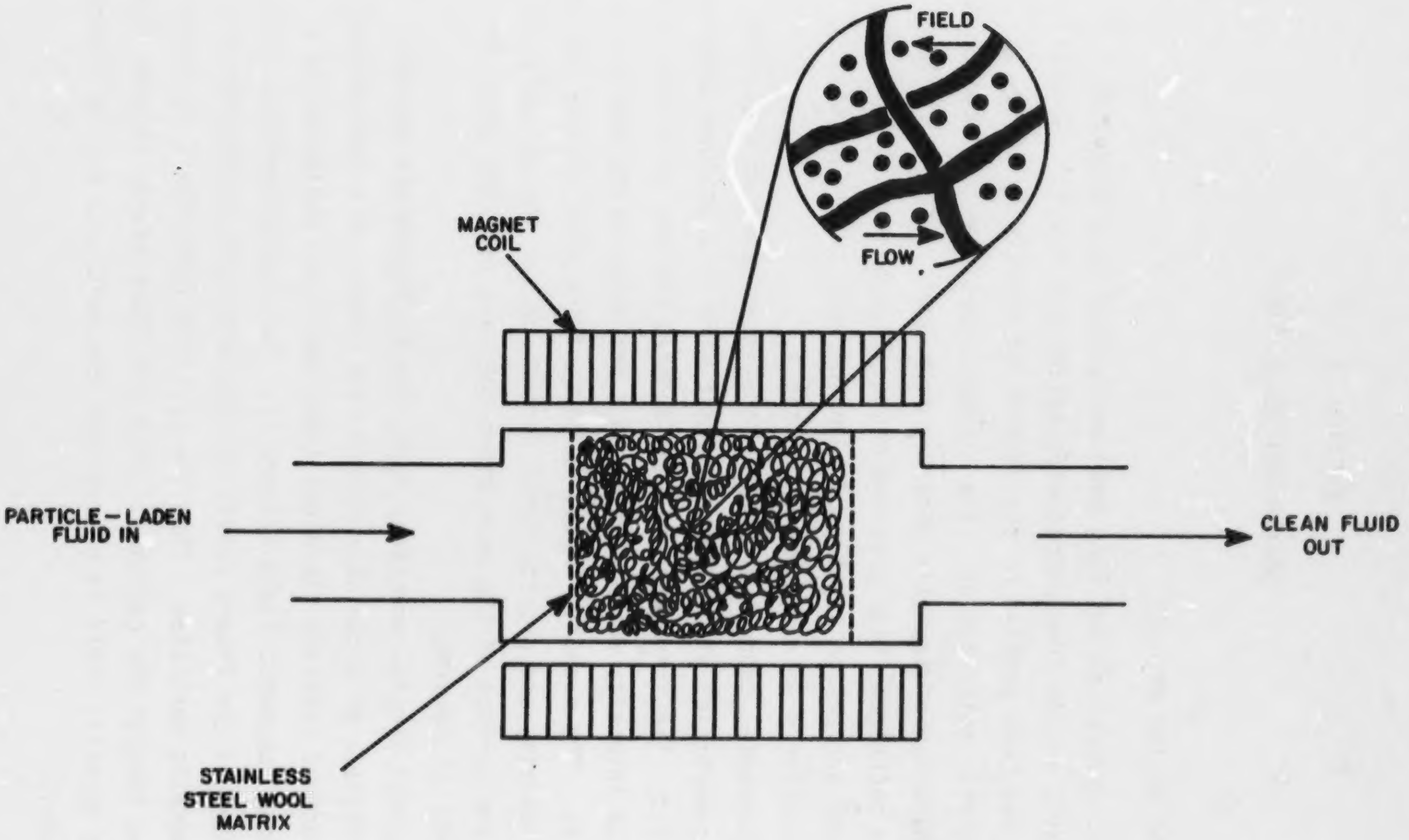
FIELD
FLOW
MAGNET COIL
PARTICLE—LADEN FLUID IN
CLEAN FLUID OUT
STAINLESS STEEL WOOL MATRIX

Figure 1. Schematic representation of a high gradient magnetic separator.

In essence HGMS is a type of enhanced filtration. However, the void volume of the filter matrix is typically much larger than in a conventional filter, allowing very high fluid velocities at relatively low pressure drop.

HGMS DEVELOPMENT AND EXPERIENCE

The chronological development of the high gradient magnetic separation process has been recorded in some detail in recent articles in the open literature [1-5] and will only be summarized here, drawing particularly from the synopses of Oder [4] and Iannicelli [5].

The expansion of magnetic separation into new process areas can be linked to the recognition of two concepts: (1) high field strengths can be utilized to polarize even weakly magnetic materials, and (2) non-uniform magnetic fields can be employed to develop magnetic forces in dipolar materials. The forerunner of modern high gradient magnetic separators is the device developed by Franz in 1937 [6]. Franz's separator utilized stainless steel screens to induce field gradients and yielded good ceramic mineral separations although it employed a field strength of only 0.15 tesla. Around 1955 Jones developed the first high intensity wet magnetic separator [7], which allowed the processing of mineral slurries with fields up to 1.0 tesla. Jones's separator employed grooved steel plates rather than screens, however; and the resulting field gradients were actually lower than those in the Franz device.

In the mid 1960's experimentation was begun at the J. M. Huber Corporation in Georgia to test the use of magnetic separation in removing small paramagnetic color-bodies from kaolin clay [8-10]. Both the Franz and Jones-type machines were tested and proven effective in this application, but the economics of commercialization were not promising. In 1967 Iannicelli constructed a hybrid high gradient-high field unit using a Jones magnet and screens from a Franz device. The hybrid separation significantly upgraded separation efficiency, and for the first time indicated commercial practicality.

In 1968 consultants from the Francis Bitter National Magnet Laboratory at Massachusetts Institute of Technology (MIT) and from Magnetic Engineering Associates (MEA) in Cambridge, Mass., were engaged in the kaolin project. Ferritic (430) stainless steel wool was tested as a collection matrix in the Huber hybrid separator and proved more effective than the larger Franz screens. In addition to the production of large field gradients, the steel wool afforded large surface-to-volume ratio (large collection surface with high porosity) and excellent corrosion resistance.

A 50-cm iron-bound solenoid was subsequently constructed for Huber by MEA, and in 1969 the first commercial clays were produced using high gradient magnetic separation as a wet beneficiation process. Since that time the HGMS process has achieved commercial acceptance in the kaolin industry. Oder reported in 1976 [4] that there was already in the industry installed magnet capacity with a potential for handling 75 percent of the world production of coating quality kaolin clays. The largest HGMS units now in service are iron-bound solenoids with magnetized volumes measuring 2.1 m in diameter by 0.5 m high (direction of flow). The coils are surrounded by a solid iron box 3 to 4 m on a side. Field strengths up to 2 T are typically used with a power consumption of 400 to 500 kW per unit.

Although the only significant commercialization of HGMS to date has been in the kaolin clay industry, interest in the process is growing rapidly [11]. Pilot-scale and laboratory investigations have been conducted in several areas. Other mineral processing applications have received considerable attention [12-16]. In addition to the work on HGMS minerals beneficiation that has been reported in the open literature, there are indications that other proprietary investigations are being conducted [4]. Related to the minerals beneficiation work is the proposed application of HGMS to the removal of iron pyrites from coal to achieve partial desulfurization [17,18]. This concept has been extended to include numerous proposals for ash removal from coal and cleaning of solvent refined and liquefied coals [19-28].

The possible use of HGMS in removing fine suspended solids from steel-making wastewaters is also under active investigation [4,11,29-32]. Other wastewater applications, including municipal sewage treatment, may be amenable to HGMS provided the process stream can be seeded with a magnetic material that will become physically or chemically associated with suspended and/or dissolved particulates [11,33-38].

Medical, pharmaceutical, and food-processing applications of high gradient magnetic separation are also possible. Experiments have been conducted which demonstrate that red blood cells (containing iron-bearing hemaglobin) can be separated without damage from whole blood using HGMS [39]. Oder [4] cites reported interest in other biologically-related areas.

Despite rapid commercialization in the clay industry and numerous experimental studies in other areas during the last several years, HGMS is just beginning to be recognized by the technical community at large as a viable technology of significant potential impact. Kolm [40] suggests that a lack of interdisciplinary communication is the primary factor that has delayed other commercial applications. HGMS extends the applicability of magnetic separation from large particles of a few ferromagnetic compounds to the much broader spectrum of chemical engineering processes involving small paramagnetic particles [2,40].

As new applications are conceived, continued research will undoubtedly be required for HGMS to reach its full potential. A better understanding of the fundamental mechanisms of the process is certainly needed. Magnet design, matrix size and configuration, and matrix cleaning methods must be tailored to specific applications [4,40,41]. The large commercial clay units utilize steel wool matrices of roughly 95 percent porosity, and operate batch-wise with 70-80 percent duty cycles [5]. For other applications, particularly in gas-processing systems, more porous matrices and continuous processing may be required to achieve economic practicality.

Large-scale HGMS devices have been built for continuous operation [[31]. In these units, the matrix is packed into an annular ring. The ring is continuously rotated through the magnetic field zone where paramagnetic particles are removed from the fluid stream. After passing through the separation zone, each segment of the matrix rotates through a zero-field flush zone for removal of the collected particles. While this design shows promise for liquid processing, it might present sealing problems in a gas stream so alternative continuous-processing schemes must be considered. Since the major developments of HGMS technology have occurred over a relatively short time span, it is reasonable to believe that many more important inventive contributions are forthcoming.

THEORETICAL ASPECTS OF THE PROCESS

Various physical phenomena may be responsible for the transport of particles from a fluid stream to the surface of a collector and for holding then on the surface after they strike it. The development of theories for conventional filtration have been adequately described by several sources [42-46]. The most commonly considered mechanisms are inertial impaction, interception, Brownian motion, gravitational settling, and electrostatic attraction. Recent literature is also replete with theoretical arguments specific to the high gradient magnetic separation process [47-65], although little experimental data has been available to adequately confirm or refute their validity.

In the development of theoretical filtration models, several common approaches and assumptions are generally used to obtain mathematical equations which can be solved. First the particles are assumed to be spherical, uniformly distributed in the fluid stream, and moving at the same velocity as the fluid upstream of the collector. The collector is assumed to be a single clean fiber of cylindrical geometry with its axis oriented perpendicular to fluid flow. The collectional efficiency of the fiber, η_f, is then defined theoretically as the ratio of the cross-sectional area of the fluid stream from which particles of a given size are collected (by the mechanism under consideration) to the projected area of the fiber in the direction of flow. Mathematically, this definition is equivalent to the equation

$$\eta_f = \frac{N_c}{2aV_oN} \tag{1}$$

where N_c = number of particles of a given size that are collected per unit length of fiber per unit time,

a = radius of the fiber,

V_o = velocity of the undisturbed fluid stream upstream of the fiber,

N = upstream concentration of particles of the given size (number of particles per unit volume).

Note that if all particles of a given size have the same mass density, Equation (1) can be expressed equivalently in terms of particle mass--i.e. η_f is both the mass and number fractional efficiency.

The following paragraphs discuss filtration mechanisms as they relate to high gradient magnetic separation. The analysis is directed toward ranges of operating parameters that were encountered in the experiments described in Sections 5 and 6. Section 5 also states reasons for operating within these particular parameter ranges.

Inertial Impaction

A fluid approaching a cylindrical body will be diverted from its original path because of the presence of the body. A particle flowing with the fluid will tend to continue its steady, rectilinear motion, and if it has sufficient momentum, will cross the diverging fluid streamlines and impact on the cylinder. To determine the theoretical impaction collection efficiency, it is necessary to determine the initial position of the particle whose centerline trajectory will just touch the collector as illustrated in Figure 2. Trajectory calculations are started at some point sufficiently far upstream (x_∞, y) where the fluid is not yet significantly affected by the presence of the collector. All particles of the same radius and mass density with initial y coordinates less than y_0 will impact, and those with initial y coordinates greater than y_0 will be diverted around the cylinder. Thus by the definition given in Equation (1)

$$\eta_i = y_0/a. \tag{2}$$

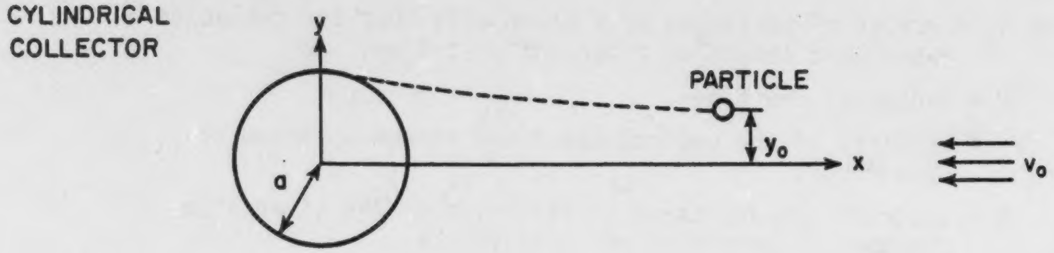

Figure 2. Critical trajectory of particle impacting on a cylindrical collector.

Several authors have determined particle trajectories for this case by integrating the equations of motion [42,44,45]. The results obtained are dependent on the flow field and initial conditions assumed. For all solutions the efficiency of impaction can be written in the form

$$\eta_i = \eta_i\left(K, Re_f, \frac{b}{a}\right) \tag{3}$$

where $K = \frac{2b^2\rho_p V_o}{9\eta a}$, Stokes number

b = particle radius

ρ_p = particle density

η = dynamic viscosity of fluid

$Re_f = \frac{2aV_o\rho}{\eta}$, Reynolds number

ρ = fluid density.

(Note: Using a different normalization scheme some authors [42,45,46] define the Stokes number as one-half the value given above. Care must be taken when using published correlations involving the Stokes number that the correct definition is used.)

Davies [43] has shown that the b/a term in Equation (3) is important only for small Reynolds numbers and very small cylinders -- conditions which are not applicable to this work. However, the relationship of η_i to K is still dependent on the Reynolds number.

For Reynolds numbers on the order of 40 and above, potential flow is often assumed, implying constant fluid density, zero viscosity (negligible boundary layer at the cylinder), and irrotational flow. Under this assumption Langmuir and Blodgett obtained the curve shown in Figure 3 (obtained from Fuchs [44]), which can be well approximated by the equation

$$\eta_i = \frac{K^3}{K^3 + 1.35\, K^2 + 0.21} \qquad (4)$$

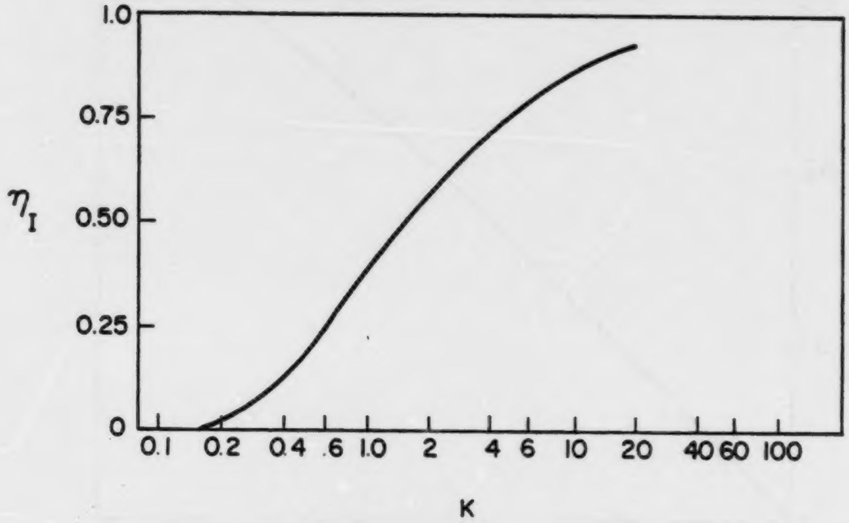

Figure 3. Inertial impaction efficiency as a function of Stokes number in potential flow.

Interception

In the development of the inertial impaction mechanism, it is assumed that no particle strikes the surface of the fiber unless its centerline trajectory is tangent to or intersects the fiber. Actually a particle will contact the surface of the fiber when its trajectory passes at a distance less than b away. This mechanism of capture is termed interception.

If a particle is assumed to have finite size but no mass, it will follow the fluid streamlines around the fiber. The efficiency of interception is therefore defined by those streamlines that pass within $y \leq a + b$ at $x = 0$ (see Figure 2). For potential flow, the interception efficiency is given by [42]

$$\eta_0 = (1 + R) - \frac{1}{1 + R} \tag{5}$$

where $R = b/a$. Figure 4 shows η_0 as a function of R for small R values in the range encountered in this work.

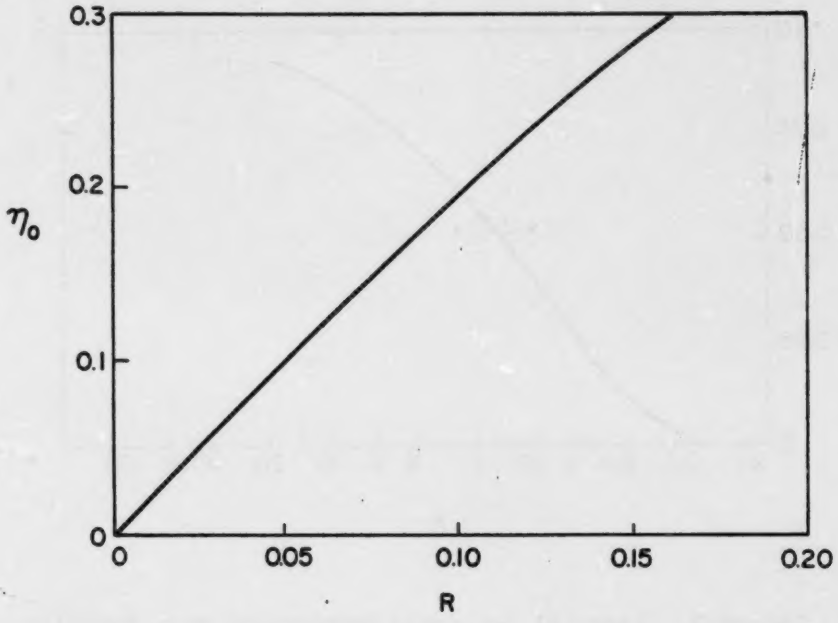

Figure 4. Interception efficiency in potential flow.

Brownian Motion

Very fine particles in a gas stream do not follow a direct path because of collisions with gas molecules. The resulting zig-zag movement of the particles around their statistical mean path (termed Brownian motion or diffusion) can result in collision with the fiber as the gas stream is diverted around it.

The characteristic parameter for this process is the Peclet number which is defined by

$$Pe = \frac{2aV_o}{D} \qquad (6)$$

where D = diffusivity of the particle given by

$$D = \frac{CkT}{6\pi\eta b} \qquad (7)$$

where C = Cunningham correction factor
k = Boltzmann's constant
T = absolute temperature.

For potential flow the diffusion collection efficiency of a single fiber can be estimated by [46]

$$\eta_d = 3(Pe)^{-1/2} \qquad (8)$$

It can be seen from Equation (8) that η_d is largest for small particles and low velocities. Under the most favorable conditions experienced in this work ($b = 0.1$ µm, $V_o = 5$ m/s), η_d is estimated by Equation (8) to be 0.003. It can therefore be considered that the diffusion mechanism is negligible under the conditions of interest.

Gravitational Settling

In general, gravitational settling is important only for large particles in slow moving gas streams. Ranz and Wong [42] showed that compared to inertial impaction, gravitational effects become important when the quantity $2ga/V_o^2$ approaches the value of the Stokes number, where g is the acceleration of gravity. Under the most favorable conditions in this work, the quantity $2ga/V_o^2$ never exceeds 2×10^{-5}, which justifies the neglect of gravitational settling.

Electrostatic Effects

Electrostatic effects can occur in a filter when an external electric field is imposed or when either the particles or fibers or both carry electrostatic charges. Charge effects frequently occur in filters made of nonconducting materials and can create spurious results. Since the filter in this case was conductive and grounded and no charges were intentionally placed on the particles, electrostatic effects were assumed negligible.

High Gradient Magnetic Attraction

Several basically similar theoretical models have been presented to explain the capture of small paramagnetic particles on the matrix wires of a high gradient magnetic separator. Like the theoretical approach to conventional filtration, these models involve the calculation of particle trajectories near a ferromagnetic wire in a magnetic field. Differences among the HGMS models arise in the assumptions made concerning the system geometry, the flow field, and the significance of forces acting on the particles. The analysis presented in some detail here follows most closely the work of Watson [48,51], who published the first such HGMS trajectory model in the open literature. (The original trajectory model development for this case should probably be credited to Zebel [66], who published a similar analysis for particles in an electrical field several years earlier.)

The Watson model considers a single cylindrical wire oriented perpendicular to the magnetic field and velocity vectors as indicated in Figure 5. The background magnetic field, H_o, is homogenous, and the

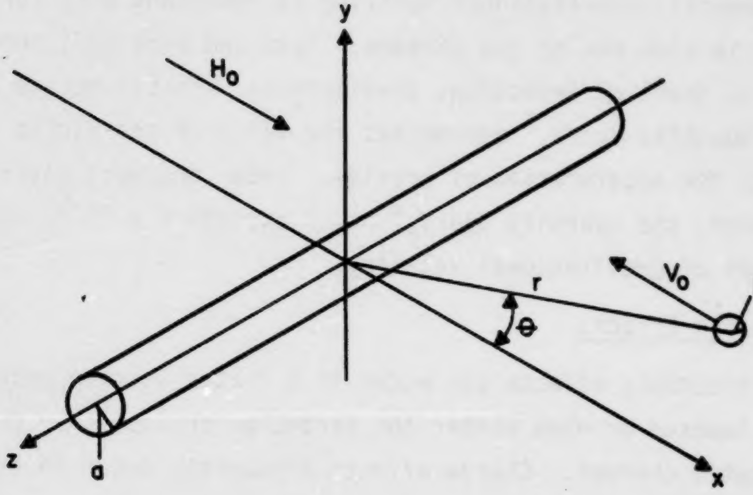

Figure 5. Geometric basis of HGMS trajectory model.

wire is uniformly magnetized to saturation. In the vicinity of the wire the field is distorted, and the resulting field gradients impose a magnetic force on the spherical, paramagnetic particles entrained in the fluid. Watson neglected the inertial and gravitational forces acting on the particles and developed an equation of motion for a single particle in the form of Newton's second law as follows:

$$\vec{F}_d + \vec{F}_m = 0 \tag{9}$$

where $\vec{F}_d$ = drag force,

$\vec{F}_m$ = magnetic force.

Since the relative velocity between the particle and fluid will in general be small, Watson invoked Stokes law for the drag force with the result

$$\vec{F}_d = -6\pi\eta b(\vec{V}_p - \vec{V}_f) \tag{10}$$

where $\vec{V}_p$ = particle velocity

$\vec{V}_f$ = fluid velocity.

Assuming potential flow, the radial and angular components of the drag force, F_{dr} and $F_{d\theta}$, then become

$$F_{dr} = -6\pi\eta b\left[\frac{dr}{dt} + V_o\left(1 - \frac{a^2}{r^2}\right)\cos\theta\right] \tag{11}$$

$$F_{d\theta} = -6\pi\eta b\left[r\frac{d\theta}{dt} - V_o\left(1 + \frac{a^2}{r^2}\right)\sin\theta\right] \tag{12}$$

The magnetic force terms presented by Watson can be developed from the fundamental equation which describes the potential energy of a particle placed in a magnetostatic field in a linear, homogenous, and isotropic medium:

$$\vec{F}_m = -\vec{\nabla}U_m = 1/2\vec{\nabla}\int_{V_i} \vec{M}\cdot\vec{B}_o\, d\nu \tag{13}$$

where U_m = potential energy,

V_i = particle volume,

M = induced magnetization of particle,

B_o = magnetic flux density of applied field.

The simplification of Equation (13) with appropriate assumptions is presented in Appendix A. The resulting expressions for the radial and angular components of the magnetic force, F_{mr} and $F_{m\theta}$, are

$$F_{mr} = -\chi B_o\left(\frac{4}{3}\pi b^3\right)\frac{a^2M_s}{r^3}\left(\frac{a^2\mu_oM_s}{2B_or^2} + \cos 2\theta\right) \quad (14)$$

$$F_{m\theta} = -\chi B_o\left(\frac{4}{3}\pi b^3\right)\frac{a^2M_s}{r^3}\sin 2\theta \quad (15)$$

where χ = magnetic susceptibility of the particle

μ_o = permeability of free space

M_s = saturation magnetization of wire.

Typical magnetic force contours are illustrated in Figure 6. Note that the force is repellent along the y axis; hence no particles would be collected on the surface of the cylinder near these points. In Equation (14) the term $a^2\mu_oM_s/2B_or^2$ occurs because of the magnetization of the wire and is called the near field correction. It becomes significant as the particle approaches the wire ($a^2/r^2 \rightarrow 1$) and can be quite important with relatively low background fields.

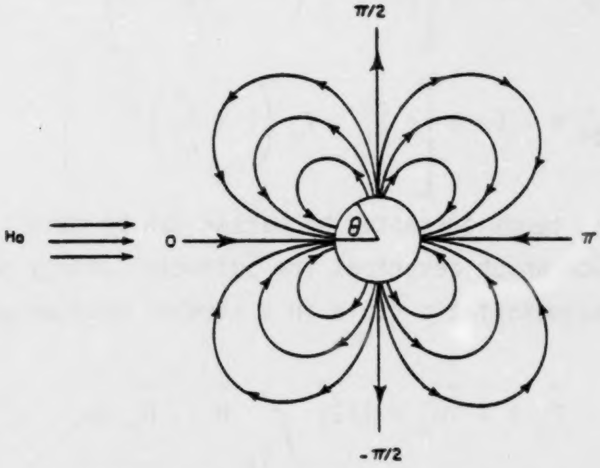

Figure 6. Magnetic force contours around a ferromagnetic cylinder oriented perpendicular to the magnetic field.

Watson substituted Equations (11), (12), (14) and (15) into Equation (9) to solve for the trajectories of particles with initial coordinates (x_∞, y_i) and determined the critical y coordinate analogous to y_0 in Figure 2. Normalizing the coordinates by the wire radius, he defined the dimensionless capture radius of the wire, $R_c = y_0/a$, which is identical to a magnetic collection efficiency, η_m, defined in the form of Equation (1).

Watson solved the substituted form of Equation (9) numerically to obtain values of R_c in terms of two dimensionless groups:

$$\frac{V_m}{V_0} = \frac{2\chi M_s B_0 R^2}{9\eta a V_0} \qquad \text{and} \qquad \frac{\mu_0 M_s}{2B_0}$$

The former group is basically a ratio of the magnetic force acting on a particle to the drag force. V_m is referred to as the magnetic velocity. The latter group is the near field correction factor. Solutions for R_c as a function of V_m/V_0 are shown graphically in Figure 7 for several values of the near field correction factor. The curves corresponding to $\mu_0 M_s/2B_0 = 0$, 0.2, 0.67, and 2.0 are from actual reported trajectory calculations [3,48,51]. The curves for $\mu_0 M_s/2B_0 = 0.88$ and 1.5 were obtained by graphical interpolation of the other four curves for purposes discussed later in this report.

It is important to note that for larger values of V_m/V_0, the value of R_c is greater than unity; that is, under favorable conditions the magnetic attraction not only keeps particles from diverging with the fluid but also will actually draw them in from beyond the projected area of the wire.

Additional understanding of the practical HGMS process can be gained from a review of other modeling efforts. Oder and Price [4,50] developed an intuitive model based on their HGMS experience at Huber. Their model predicts the successive probability of particles striking the wires and being held once they strike. Parametrically the result is identical to Watson's model solution for the case $V_m/V_0 < \sqrt{2}$ and $\mu_0 M_s/2B_0 = 0$ where it can be shown that $R_c = V_m/2V_0$. Oder and Price's model provides a simple expression that can be quite useful in correlating high field, low velocity data, but it is not parametrically correct for most of the conditions experienced in this work.

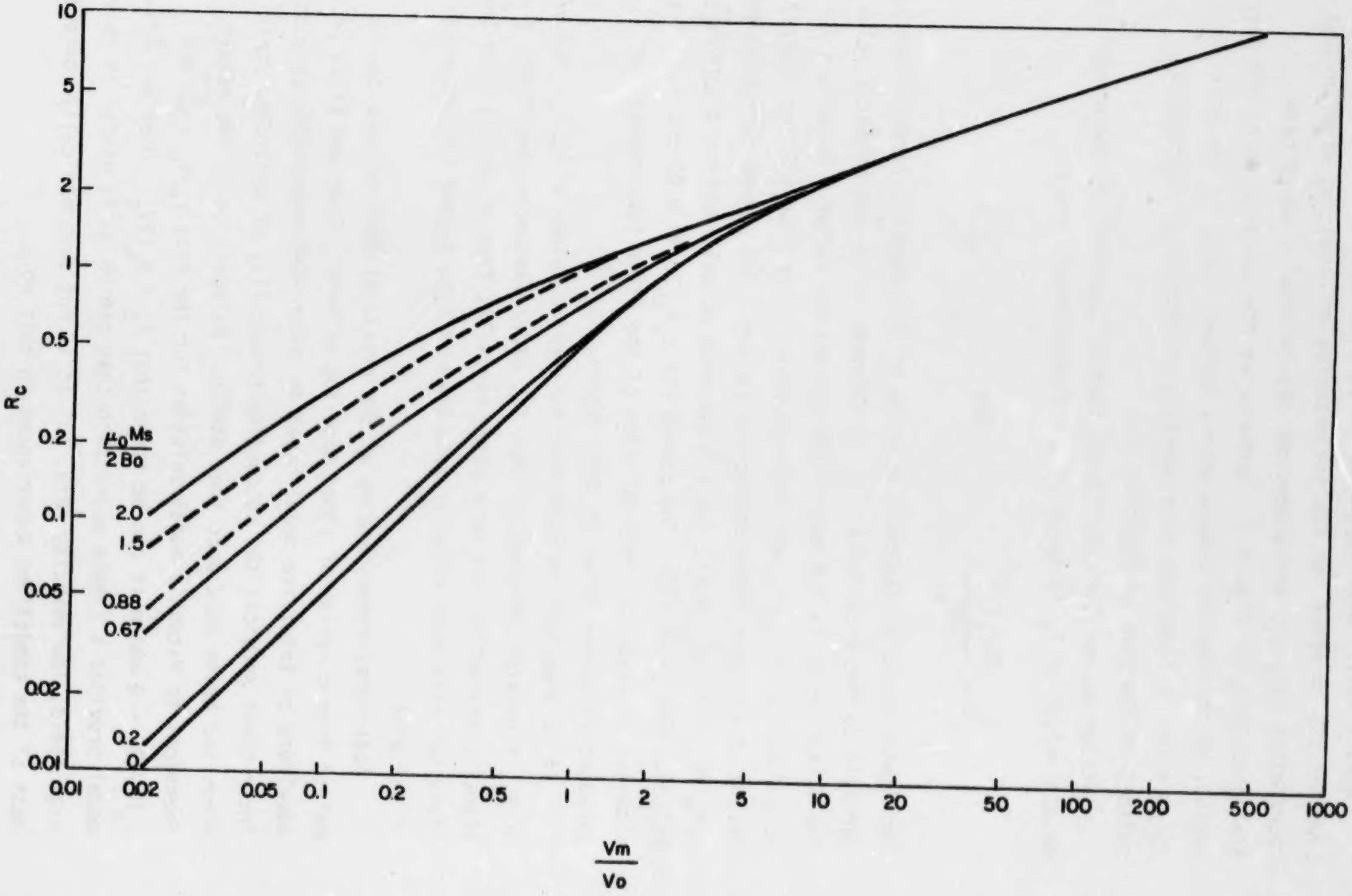

Figure 7. Dimensionless capture radius from Watson's trajectory model.

Oberteuffer [1] developed a force balance for a paramagnetic particle on the surface of the wire at the point $x = a$, $y = 0$ (Figure 5), and deduced the significant result that the maximum magnetic force occurs when the wire radius is approximately 3 times the particle radius. This concept has two important implications: (1) If possible, the fiber size should be matched to the particles being collected; and (2) extrapolation of the single-fiber/single-particle model to a real HGMS system is complicated when both the wires and particles are actually characterized by a distribution of sizes.

In terms of system geometry, Watson [51] also considered the case where the background magnetic field vector is perpendicular to the fiber and to the flow vector (i.e., in the y direction in Figure 5). This configuration corresponds to the use of an H-type magnet rather than a solenoid and could offer some advantages in terms of access to the matrix for cleaning. Although the theory predicts higher values of R_c for a given value of V_m/V_0 with this geometry, observed collection efficiencies are reportedly lower than the parallel vector case [41]. Watson attributes this anomaly to the fact that particles are preferentially collected in this geometry at the point $x = 0$, $y = a$ (Figure 5), where the shear forces of the fluid are greatest.

Birss, et al. [60] as well as Uchiyama, et al. [61] have theoretically investigated the geometry in which the flow is parallel to the fiber and the field is perpendicular to both. This geometry does not appear to offer any practical advantage in most applications, and the collection efficiency is always less than it would be if the flow were perpendicular to the fiber. The remaining geometric permutations in which the fiber and field were parallel are of no significance since no magnetic gradients are produced.

Cummings, Prieve, and Powers [58] demonstrated in an analysis similar to Watson's that the assumption of creeping flow rather than potential flow reduces the capture radius by as much as a factor of three because of earlier diversion of fluid streamlines. This factor demands caution when using Watson's model with real liquid system data in which the fiber Reynolds number is frequently as low as 1. With the conditions encountered in this work, the Reynolds number ranged from about

15 to 30. Potential flow is thus a better approximation than creeping flow, but boundary layer effects may still be significant.

In real systems employing steel wool fibers, the wires are often highly irregular in shape in contrast to the cylindrical shape assumed in Watson's model. Stekly and Minervini [59] theoretically investigated the shape effect on capture radius using elliptical shapes of varying aspect ratio. For clean wires the capture radius varies little with shape (aspect ratio) so long as the projected upstream area is constant. However, as particles begin to build up on the wires, the shape of the clean wire can be an important factor in determining the rate of deterioration in collection efficiency.

Luborsky and Drummond [53,56] have investigated this deterioration in collection efficiency with particle buildup in some detail. As weakly paramagnetic particles are accumulated on the wire, the volume in which field gradients are large is gradually filled. Also the flow streamlines are diverted farther upstream as the wire "grows" in diameter. These two factors combine to give a reduced capture radius in comparison to the prediction of Watson's clean fiber model. Luborsky and Drummond developed a modified version of Watson's model in which particles are assumed to accumulate in successive layers. Viscous and magnetic forces are compared to determine when each layer is filled. Using two adjustable parameters -- the first representing the fraction of fibers that are active in the capture process and the second to account for mechanical entrapment of particles -- they were able to obtain a reasonable fit for Oberteuffer's experimental data [49] on the collection of cupric oxide particles in water.

Cowen, Friedlaender, and Jaluria [52,57,62] have succeeded in obtaining photographs of actual particle accumulation on a single wire using all three flow, field, and fiber geometries mentioned earlier. In general, the photographs qualitatively confirm the validity of Watson's model and Luborsky and Drummond's approach to particle buildup. The most important discrepancy is the absence of significant collection on the back side of the wires in the experimental setup with the geometry illustrated in Figure 5. Theoretically some particle trajectories will result in capture in this region near $x = -a$, $y = 0$.

The effect of the inertial terms, which were ignored in Watson's model, on the equations of motion may be of paramount importance to gas-stream applications of HGMS. Watson argued [51] that these terms are negligible in comparison to viscous and magnetic terms, but his development was directed toward low velocity liquid systems. In gas-stream systems the achievement of high velocity flow may be critical to the economic viability of the process, and the effects of inertia become more significant. Three groups have independently developed models incorporating inertia in recent publications [54,63,65]. The work of Lawson, et al. [65] is presented in the most detailed and usable form.

Lawson [64,65] solved the equations of motion incorporating inertial, viscous, magnetic, and gravitational terms and demonstrated that the particle trajectories are uniquely determined by four dimensionless groups:

$$W = \frac{\mu_o \chi H_o^2}{(1 + 1/3\chi)\rho_p V_o^2} \quad \text{magnetic parameter} \tag{16}$$

$$A = \frac{\lambda}{2\pi a^2 H_o} \quad \text{near field correction} \tag{17}$$

$$K = \frac{2b^2 \rho_p V_o}{9a\eta} \quad \text{Stokes number} \tag{18}$$

$$G = \frac{ag}{V_o^2}\left(1 - \frac{\rho}{\rho_p}\right) \quad \text{gravitational parameter} \tag{19}$$

where λ is the dipole moment per unit length; the other quantities have been previously defined.

In a high velocity gas-stream system the gravitational parameter will be on the order of 10^{-5}, which is negligible. Furthermore, it can be shown that if the wire is homogeneous and magnetized to saturation, the term A reduces to the near field correction factor introduced in Watson's model; and the quantity 2AWK is equal to Watson's V_m/V_o. The appearance of χ in the denominator of Equation (16) arises from a more rigorous derivation of the particle magnetization, which is important when the susceptibility is relatively large.

For the purpose of this work, the most useful result of Lawson's model is illustrated in Figure 8, which shows lines of constant capture radius versus the magnetic parameter and Stokes number with fixed A and negligible gravitational effects. The curvature of the lines demonstrates the intuitive effect of inertia on the capture radius. With log K = -2, inertial forces are negligible, and the R_c values are identical to those which would be obtained from Watson's model. Furthermore Watson's model predicts that with fixed A, R_c is constant so long as the sum (log K + log W) is constant. Hence, ignoring inertia, all of the contours would be straight lines of slope = -1 and would pass through the points as shown in Figure 8 where log K = -2. The downward curvature of the line for R_c = 0.5 thus illustrates that inclusion of inertial terms increases R_c in this case as it should since inertial forces are beneficial in preventing the particles from being diverted around the wire. For $R_c > 1$, however, inclusion of the inertial terms reduces R_c since this case corresponds to the magnetized wire's ability to draw in particles from outside its projected area, and inertial forces will tend to keep the particles outside the projected area moving in steady, rectilinear motion. The line for R_c = 1 is straight with slope = -1. The points at which the lines begin to curve indicate the onset of significant inertial effects. Note that for smaller values of W (lower magnetic fields and higher velocities), inertial forces becomes significant at lower values of K.

Reentrainment

Theoretical models of conventional filtration systems normally assume that every particle that touches the fiber surface adheres. With sufficiently high gas velocities the validity of this assumption becomes questionable. With no magnetic field the particle approaches the fiber under the influence of inertial and viscous forces. When it strikes the surface, the inertial forces are dissipated; and in the absence of electrostatic effects, only Van der Waals forces are left to compete

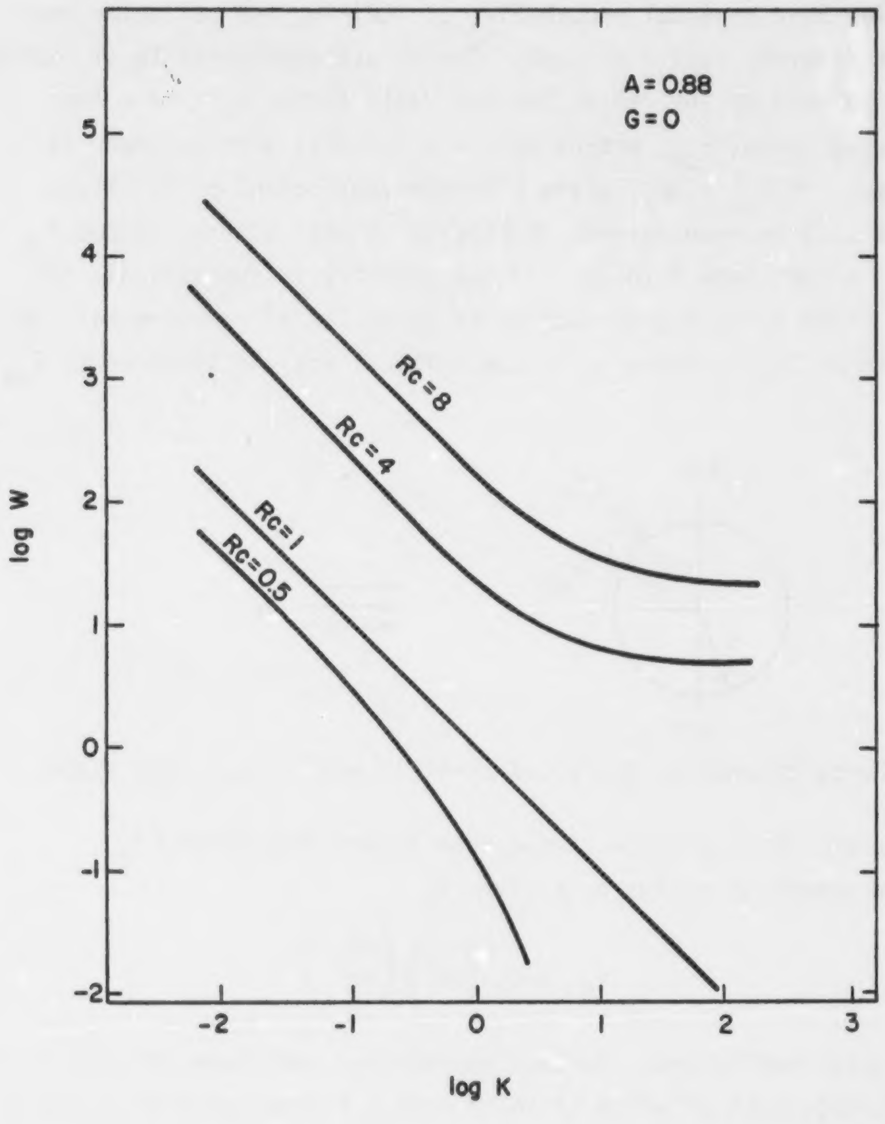

Figure 8. Lines of constant capture radius with inertial forces included [64].

with viscous drag and prevent reentrainment. The importance of reentrainment can be estimated by constructing a force balance for particles located at the surface of the fiber.

Considering the geometry illustrated in Figure 9, it is assumed that particles have an equal probability of striking the collector anywhere in the interval $-\pi/2 < \theta < \pi/2$. The illustrated particle of radius b will then be held by the radial Van Der Waals force, F_a, while the tangential drag force, $F_{d\theta}$, acting at $r = a + b$ will tend to shear it off the fiber. If $F_{d\theta} > kF_a$, where k is the coefficient of friction, the particle will be reentrained. Otherwise it will adhere. Since $F_{d\theta}$ increases as θ goes from 0 to $\pi/2$ and the geometry is symmetrical, the fraction of fiber surface area over which particles of radius b will be held is given by $2\theta_c/\pi$, where θ_c is the critical angle determined by $F_{d\theta} = kF_a$.

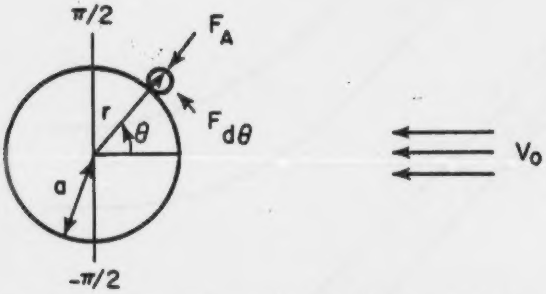

Figure 9. Force balance on collected particle with no magnetic field.

In general, the magnitude of the free stream drag force, F_{do}, acting on an sphere of radius b is given by

$$F_{do} = C_d \left(\pi b^2\right) \left(\frac{\rho V_o{}^2}{2}\right) \tag{20}$$

where C_d = drag coefficient. Various expressions have been offered for the drag coefficient, each of which is valid over a finite range of Reynolds numbers. The best known of these was given by Stokes as $C_d = 24/Re_p$ where Re_p is the particle Reynolds number defined by $2b\rho V_o/\eta$. This expression is equivalent to Stokes law, which was utilized in Equation (10) and is valid with Reynolds numbers up to about 0.5. For particles on the surface of the wire relative velocity is increased, however; and Reynolds numbers of interest will range from about 0.1 to 10. For this range a least-square curve was fit to experimental data obtained by Moller and Davies and reported in Fuchs [44] with the result

$$C_d = \frac{24.08}{Re_p}\left(1 + 0.126\ Re_p - 0.009\ Re_p{}^2\right). \tag{21}$$

In potential flow the tangential component of the drag force at any θ and r = a + b is then given by

$$F_{d\theta} = F_{do}\ \sin\theta\left[1 + \frac{a^2}{(a+b)^2}\right]. \tag{22}$$

According to Hamaker's microscopic theory, the Van der Waals force between a sphere of radius b and a half-space is given by [67]

$$F_a = \frac{\acute{A}b}{6z^2} \tag{23}$$

where $\acute{A}$ = Hamaker constant

z = separation distance between the sphere and half-space.

The parameter z cannot be measured easily and is usually estimated to be 4×10^{-10} m, which corresponds to the lattice constant for crystals with Van der Waals bonds [46,67,68]. Hamaker constants vary by orders of magnitude for different materials. Visser [69] reports two values of interest to this work: for Fe on Fe in vacuum, $\acute{A} = 2.12 \times 10^{-19}$ J; and for Fe_2O_3 on Fe_2O_3 in vacuum, $\acute{A} = 2.32 \times 10^{-19}$ J.

The coefficient of friction required in this analysis likewise cannot be predicted with confidence. To initiate particle sliding a static coefficient of friction on the order of 0.5 would be appropriate [70]. If the particle were considered to roll off rather than slide, the coefficient of friction would be closer to 0.01 [70].

Summarizing the above equations and assumptions, the fraction of colliding particles that are retained on the fiber surface is given by $2\theta_c/\pi$, where

$$\theta_c = \text{Arcsin}\left[\frac{k\acute{A}b}{6z^2 F_{do}\left(1 + \dfrac{a^2}{(a+b)^2}\right)}\right] \tag{24}$$

Using the estimates given above, the lumped parameter $k\acute{A}/6z^2$ should have a value in the range of 0.002 to 0.1 N/m depending on the choice of friction coefficients. Uncertainty in the other parameters could broaden this range. More importantly, Equation (24) indicates the functional relationship of the reentrainment phenomenon on system operating parameters.

In the HGMS process, reentrainment will be greatly reduced or eliminated by the presence of the magnetic force. As a first approximation one might estimate no reentrainment since the capture radius is calculated from a force balance involving both the drag and magnetic forces, and the magnetic forces are strongest at the surface of the wire. Luborsky and Drummond's arguments on particle buildup [53,56] imply the use of an effective reentrainment factor with predicted capture radii, however, if the capture radii are predicted from a clean fiber model.

Combination of Mechanisms

From the previous arguments it is apparent that in an HGMS filter with no applied field, three particle collection phenomena can still function to a significant extent: inertial impaction, interception, and reentrainment. It is incorrect to add the single fiber collection efficiencies of impaction and interception since this method could in principle lead to some particles being collected more than once on the same fiber. If the mechanisms are considered independently and the fraction of particles in the projected area of a fiber collected by impaction is η_i, then interception can collect no more than $\eta_o(1-\eta_i)$. Summing these efficiencies and accounting for reentrainment then gives for the net single fiber efficiency

$$\eta_f = (\eta_i + \eta_o - \eta_i\eta_o)\frac{2\theta_c}{\pi} \, . \tag{25}$$

In a practical HGMS system in which the field is energized and oriented parallel to bulk flow, the interception mechanism loses its significance since it implies collection near the points $\theta = -\pi/2$, $\pi/2$, and these are points of magnetic repulsion (see Figure 6). Lawson's solution of the type illustrated in Figure 8 includes both the high gradient magnetic and inertial effects. Thus, if reentrainment is assumed negligible in this case, the net single fiber collection efficiency is simply given by

$$\eta_f = R_c \, . \tag{26}$$

Collection Efficiency of a Total Filter

Several slightly different approaches have been used to generalize from the collection efficiency of a single fiber to a complete filter or matrix [42,45,46,48]. For the limiting conditions of high porosity and many fiber layers, these methods differ only by constants related to the geometric assumptions.

Consider the matrix of differential length and unit cross-sectional area illustrated in Figure 10. Fibers oriented parallel to the flow and field will be ineffective for particle capture. Hence the fraction of total fiber length that is effective in the randomly packed matrix is given by the fraction that projects on a plane perpendicular to the flow and field, which is

$$\frac{\int_0^{2\pi}\int_0^{\frac{\pi}{2}} \cos\left(\frac{\pi}{2} - \phi\right) d\phi d\alpha}{\int_0^{2\pi}\int_0^{\frac{\pi}{2}} d\phi d\alpha} = \frac{2}{\pi} \, . \tag{27}$$

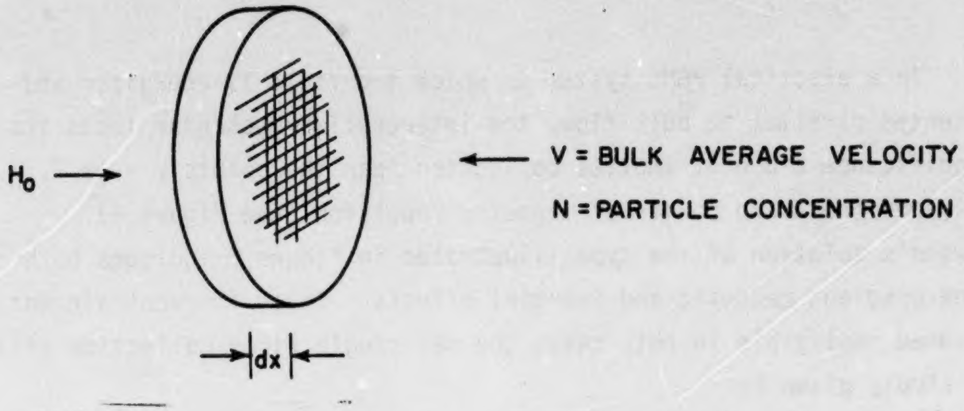

Figure 10. Differential matrix segment.

With collection efficiency defined in the form of Equation (1) a mass or number balance for particles of a single size can be constructed in the following form:

$$\text{Particle Flux In} = \text{Particle Flux Out} + \text{Particles Collected} \qquad (28)$$

$$NV = (N + dN)V + \left(\frac{2aNV\eta_f}{1 - F}\right)\left(\frac{2}{\pi} \cdot \frac{Fdx}{\pi a^2}\right) \qquad (29)$$

where $\frac{2aNV\eta_f}{1 - F}$ = particles collected per unit length of fiber per unit time

$\frac{2}{\pi} \cdot \frac{Fdx}{\pi a^2}$ = total length of fiber projected perpendicular to flow in the unit cross section of matrix

$V = V_o(1 - F)$ = bulk average velocity upstream of matrix

F = fractional packing density (1 - porosity).

Rearranging Equation (29) and integrating over a matrix of length L gives

$$P = \frac{N_o}{N_i} = \exp\left[-\frac{4FL\eta_f}{\pi^2 a(1 - F)}\right] \qquad (30)$$

where P = penetration

N_o = particle concentration at matrix outlet

N_i = particle concentration at matrix inlet.

Equation (30) expresses the theoretical fractional penetration on a number or mass basis for a single particle size. The applicable value of η_f is selected from Equation (25) or (26). Since the extrapolation from a single fiber to the total matrix inherently assumes that there are no particle-to-particle or fiber-to-fiber interactions and contains the idealized $2/\pi$ fiber-orientation factor, the numerical factor $4/\pi^2$ should be considered as a first approximation for an "effectiveness factor" to be verified or determined empirically through experiment.

POTENTIAL APPLICATIONS OF HGMS TO FINE PARTICLE EMISSION CONTROL

Probably the most important parameter to be considered in the evaluation of potential applications of HGMS is the particle susceptibility. Particles with high magnetic susceptibilities will be most easily and economically collected by the HGMS method. Significant emissions of such particulates are found in the iron and steel industry and the ferroalloy industry. Emissions from various processes in these industries contain high percentages of FeO, Fe_2O_3, MnO, Mn_2O_3, Mn_3O_4, Cr_2O_3, and other highly paramagnetic compounds. Table 1 lists several potential applications with typical reported dust compositions. The composition obviously varies widely among the different processes. Within a single process category the composition will vary over a more narrow range with changes in raw feed and operating conditions. However, the susceptibility of heterogeneous dust particles cannot be predicted accurately even when a bulk composition is known. The valence state of ferromagnetic elements is extremely important because very small percentages of ferromagnetic species can produce order-of-magnitude increases in susceptibility. Fortunately, the susceptibility of small samples can be determined experimentally using a Faraday balance or similar device, providing a reasonably simple way to screen potential applications.

TABLE 1. POTENTIAL APPLICATIONS OF HGMS TO FINE PARTICLE EMISSION CONTROL

Industrial Process	References	Typical Dust Composition, mass basis
Sinter Plant	-	Highly variable
Blast Furnace	[71]	35-50% Fe, 12% FeO, 0.5-0.9% Mn
Basic Oxygen Furnace	[71,72]	90% Fe_2O_3, 1.5% FeO, 4% Mn_3O_4
Open Hearth Furnace	[71,72]	85-90% Fe_2O_3, 1-4% FeO, 0.5% MnO
Electric Arc Furnace	[71,72]	20-55% Fe_2O_3, 4-10% FeO, 0.5% MnO
Silico-manganese Furnace	[71,72]	4-7% FeO, 30-35% MnO
Ferro-manganese Furnace	[71,73]	6% FeO, 34% MnO
Ferro-chrome Furnace	[71,73]	7-11% FeO, 3% MnO, 29% total Cr

Particle size also varies widely in different types of dusts, and the susceptibility can vary with size in a single process due to compositional changes with size. HGMS theory predicts in general a decrease in collection efficiency with size, but experimentation with particular dusts will be required to determine the minimum feasible size to collect. Gas temperature may also be an important factor. Trendwise, particle susceptibilities are proportional to the reciprocal of absolute temperature assuming Curie law behavior [74]. Gas viscosity increases with increasing temperature. Both of those trends theoretically reduce HGMS efficiency at higher temperatures, but the effects could be minor. Again experimentation will be required to determine the technical and economic practicalities of the process. Theoretical aspects, however, can play a strong role in designing experiments and equipment and understanding experimental results.

SECTION 5

EXPERIMENTAL WORK

BASIS OF EXPERIMENT DESIGN

The bench-scale experimental test program was planned to evaluate the preliminary technical and economic feasibility of applying high gradient magnetic separation to fine particle control. Existing methods of fine particle collection for air pollution control are generally characterized by a limited range of capital costs and energy requirements. Although the actual values vary greatly with the specific technology applied, the type of source controlled, and the efficiency of particulate collection, many common applications require a capital investment of roughly \$2000 to \$8000/m^3/s of gas flow (\$1 to \$4/CFM) for uninstalled primary equipment. Power consumption frequently ranges from 1.6 kW to 3.2 kW/m^3/s of gas flow (1 hp to 2 hp/1000 CFM). Total mass collection efficiencies of greater than 99 percent are typical, and the current trend is to design for at least 90 percent collection of submicron particulate. If HGMS is to become a viable alternative to present control methods, satisfactory performance must be demonstrated with competitive estimates of capital cost and power requirements or some other significant advantage over present technology must be exhibited.

To focus the HGMS evaluation on practical operating conditions, the upper bounds of the above rule-of-thumb capital costs and power requirements were adopted as tentative performance goals. With appropriate design information and assumptions these goals were then transformed into tentative limitations on major operating variables. The transformation is explained in the following paragraphs.

Capital Cost

In late 1975 when this analysis was first conducted, the largest commercially operating HGMS systems were iron-bound solenoids with a 2.13-m (7-ft) diameter bore and a 50-cm (20-inch) matrix length.

According to one vendor of commercial-scale equipment, the cost of a unit of this type with a field rating of 0.2 T would have been approximately $240,000 including the magnet, power supply, and cooling equipment [75]. This estimate indicated that the superficial gas velocity would have to be at least 8.4 m/s (1650 ft/min) to keep the capital cost below $8000/m^3/s ($4/CFM) with a duty cycle approaching 100 percent.

Power Requirements

The major power requirements of HGMS in a particle/gas system would be generation of the magnetic field and operation of the gas moving equipment. To produce a background field of 0.2 T, the large iron-bound solenoid referenced above would require approximately 20 kW electrical input [75]. A unit of the same size has been reported to consume 200 kW of power to produce a field of 1.0 T [76]. These two figures provided baseline data that were used to calculate magnet power requirements for the field/velocity combinations shown in Table 2.

TABLE 2. ESTIMATED MAGNET POWER REQUIREMENTS FOR SEVERAL FIELD/VELOCITY COMBINATIONS

Background Field	Gas Velocity		Magnet Power		
T	m/s	ft/min	kW	kW/m^3/s	hp/1000 CFM
0.2	5	984	20	1.12	0.71
0.2	10	1968	20	0.56	0.35
1.0	5	984	200	11.23	7.12
1.0	10	1968	200	5.61	3.57

Fan power requirements are directly proportional to the product of gas flow rate and pressure drop. With a 60-percent efficient fan a pressure drop of 2.5 kPa (10 inches of water) is equivalent to a power requirement of 4.17 kW/m^3/s (2.63 hp/1000 CFM).

The bench-scale experiment design and execution were strongly influenced by the results of this analysis. However, since the design of large electromagnets has been primarily for research usage in the past (with the exception of the several units now in use in the clay industry), cost reductions and more energy-efficient designs might be anticipated should HGMS emerge as a widely used technology. Accordingly the limiting conditions for the major operating variables were initially specified at the following levels:

Operating Parameter	Limiting Condition
Superficial gas velocity	>5 m/s (984 ft/min)
Pressure drop	<2.5 kPa (10 inches of water)
Background magnetic field	<1.0 T
Collection efficiency	>90% for submicron particles >99% for particles greater than 1 μm

Basic oxygen furnace dust was selected as the test dust from the list of likely candidates because it satisfied three important criteria: (1) it is associated with a major industrial process, (2) it is difficult to collect by conventional methods because of the high mass percentage of submicron particles, and (3) it is one of the strongest candidates for successful HGMS application because of the typically large ferric oxide content.

SUMMARY OF PHASE I EXPERIMENTS AND RESULTS

Apparatus and Procedures

The experimental apparatus utilized in Phase I is shown schematically in Figure 11. Basically, the apparatus consisted of a fluidized bed system to redisperse the dust followed by a section in which the dust was diluted with clean air. The dirty air stream was then passed through the magnetic separator and vented. Samples were extracted upstream and downstream of the magnetic separator and analyzed to determine the particle size distribution and concentration.

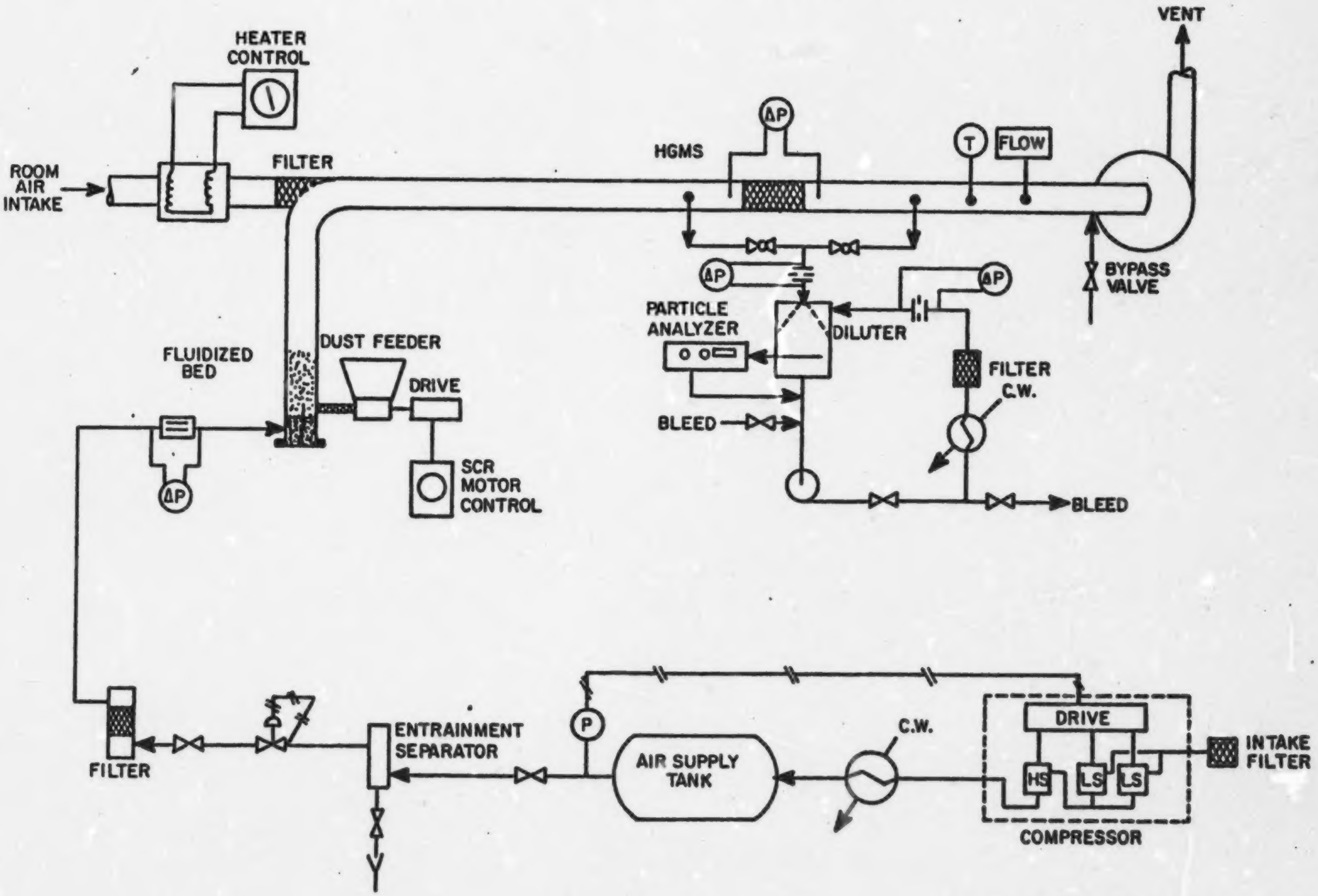
HEATER CONTROL
ROOM AIR INTAKE
FILTER
HGMS
ΔP
T
FLOW
VENT
BYPASS VALVE
ΔP
PARTICLE ANALYZER
DILUTER
ΔP
FILTER
C.W.
BLEED
BLEED
FLUIDIZED BED
DUST FEEDER
DRIVE
ΔP
SCR MOTOR CONTROL
FILTER
ENTRAINMENT SEPARATOR
P
AIR SUPPLY TANK
C.W.
DRIVE
HS
LS
LS
COMPRESSOR
INTAKE FILTER

Figure 11. Experimental apparatus used in preliminary HGMS experiments.

A dust redispersing system was chosen for source simulation over artificial particle generators because it allowed the use of an actual industrial dust at a comparatively high feed rate. The fluidized bed system was similar in principle, although somewhat different in application, to equipment described by Guichard [77], Blann and Moreno [78], and Willeke and co-workers [79]. The fluidized medium was nickel metal powder sieved to a size range of approximately 75 to 100 μm. Fluidizing air was compressed and cooled, passed through an entrainment separator and submicron filter, and metered into the bed to provide a superficial velocity of approximately 15 cm/s.

The test dust was obtained from the hoppers of an electrostatic precipitator which controls emissions from a basic oxygen furnace at a Pennsylvania steel mill. The dust was fed into the fluidized bed by a small screw feeder. The fluidized nickel spheres partially deagglomerated the bulk dust, allowing it to be entrained in the superficial air flow. The fluidized BOF dust was diluted by mixing with a stream of clean room air. The incoming air was preheated to 38° C (100° F) to reduce the relative humidity and filtered to remove some of the background particulate. To minimize the complexity of the experimental apparatus, all of the Phase I tests were limited to 38° C.

The dusty air stream was passed through the high gradient magnetic separator, which consisted of a 35.6-cm long steel canister with an inside diameter of 8.9 cm. The canister was positioned in the bore of an iron-bound solenoid where the background magnetic field could be adjusted in six increments from 0.094 to 0.965 T. The electromagnet and its associated power supply constituted a commercially available laboratory HGMS unit which was leased from Magnetic Engineering Associates of Cambridge, Massachusetts. The filter material was 430 stainless steel wool similar to that used in previously reported experiments [49].

Sampling and analysis were accomplished using a custom dilution system and a commercial optical particle analyzer. Sequential sampling was conducted upstream and downstream of the HGMS apparatus to determine the collection efficiency as a function of particle size. Since rather long sample lines were required, information on the larger particles (3 μm and above) was unavoidably lost.

Dilution of the samples was required to avoid coincidence loss in the optical analyzer. Specifications for the dilution system were obtained through the courtesy of Southern Research Institute (SoRI) in Birmingham, Alabama. In the SoRI-designed diluter the sample stream is fed into a conical vessel where it is mixed in highly turbulent flow with a filtered stream of dilution air. A dilution ratio of 50:1 was used throughout these tests. Calibrations by SoRI [80] have shown that this type of diluter yields representative samples very close to the predicted dilution ratio for submicron particles. Some transmission losses experienced by SoRI with 2.3 μm particles during calibration caused greater uncertainty in the predicted dilution ratio.

Single point, isokinetic sampling was initially attempted in this preliminary work, but a problem developed because larger particles were drawn through the sample lines and deposited in the diluter. These particles would then occasionally become broken up and entrained, causing spurious counts. To eliminate the problem, it was necessary to turn the sample nozzles downstream to prevent large particles from entering the sampling apparatus. This extreme deviation from isokinetic sampling probably led to some bias in the sampling of even the fine particles. However, since the upstream and downstream particle concentrations were ratioed to calculate a collection efficiency, it was assumed that the sample bias was eliminated by the ratio (i.e., that the bias for any given particle size was a constant factor independent of particle concentration and equal at the upstream and downstream sample points).

The particle analyzer was a Climet Model 208A which uses near-forward scattering of visible light to count and size particles in discrete increments. The optical particle analyzer was chosen primarily because it allowed the measurements to be made in near-real time. The particular unit used in this study was a special-order model including an extra increment in the submicron range. Data were extracted for four optically determined ranges of particle diameter: 0.3 to 0.5 μm, 0.5 to 0.7 μm, 0.7 to 1.0 μm and 1.0 to 3.0 μm.

During each HGMS run three or more particle counts were taken upstream and downstream in sequence. A collection efficiency was calculated from each paired data set, and the results were averaged to obtain the efficiency for the particular run. Although the individual data sets sometimes yielded penetration results differing by as much as a factor of two, they showed no trend with time; that is, all of the data were collected before significant loading of the matrix occurred. Between runs the filter matrix was forward-flushed (aided by manual rapping) with the magnet off. Occasional duplication of runs showed that this method of cleaning returned the matrix to its original condition within the limits of experimental error. One long-term run was made to observe the effects of uninterrupted filter loading.

Salient Experimental Results

The ranges of important operating parameters are summarized in Table 3. Figures 12, 13, and 14 show results of several runs that encompass the ranges of these variables. The dramatic improvement in collection efficiency upon application of a low magnetic field is most easily seen in those groups in which zero-field runs were made. Increases in the background field further reduced the particle penetration as expected. Fields higher than 0.308 T were never needed because in all tests the collection efficiency approached or exceeded detectable limits with the 0.308 T field.

The effect of gas velocity was less obvious. Efficiencies exceeding 90 percent were achieved with both low and high velocities. Increases in velocity seemed beneficial in some test series and detrimental in others. At this point in the program the effect of gas velocity on collection efficiency was not well understood.

TABLE 3. RANGES OF OPERATING PARAMETERS - PHASE I EXPERIMENTS

Magnetic Field, T	0-0.308	0-0.214	0-0.214
Matrix Length, cm	20.3	20.3	20.3
Packing Density	0.0088	0.0132	0.0174
Gas Velocity, m/s	5.9-9.3	6.1-10.6	5.9-10.2
Pressure Drop, kPa	0.7-1.3	1.2-2.9	1.4-3.2
(in. H_2O)	(2.8-5.3)	(4.7-11.5)	(5.4-12.8)

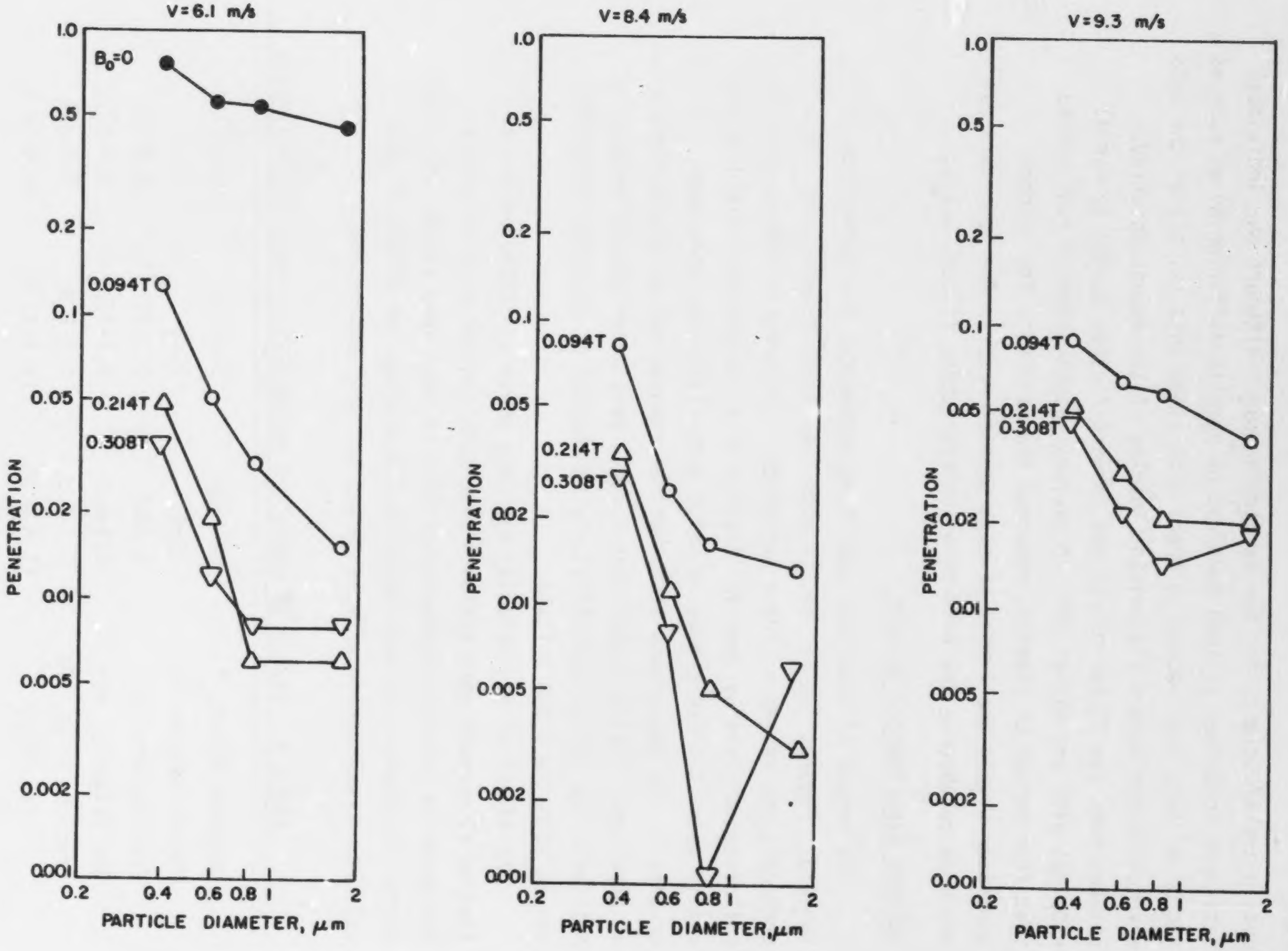

Figure 12. Results of bench-scale HGMS tests with packing density of 0.0088.

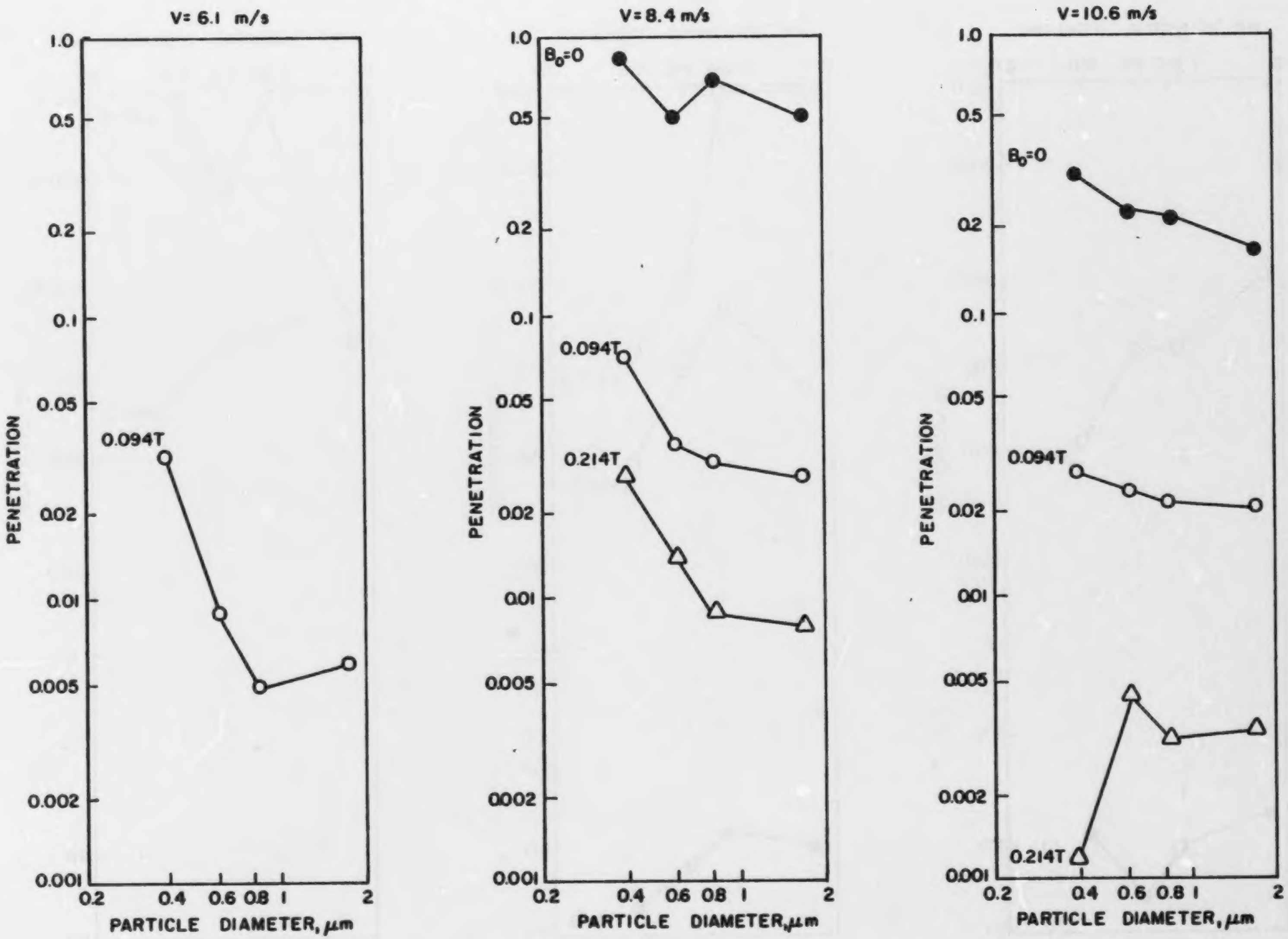

Figure 13. Results of bench-scale HGMS tests with packing density of 0.0132.

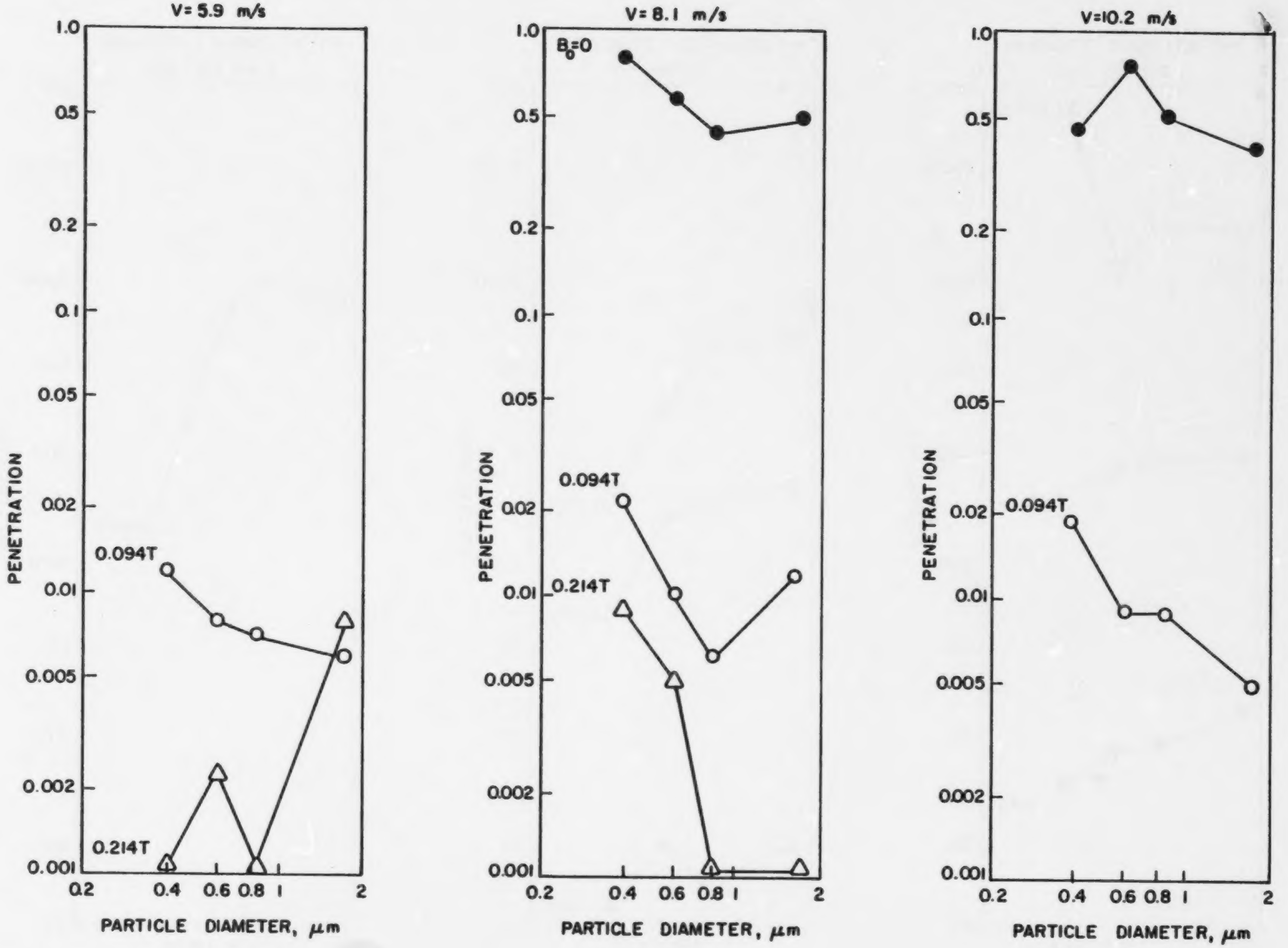

Figure 14. Results of bench-scale HGMS tests with packing density of 0.0174.

The important effect of matrix packing density can also be seen by comparing runs with comparable velocities in Figures 12, 13, and 14. Increasing the packing density yielded a definite improvement in collection efficiency but also increased the matrix pressure drop.

One long-term run was made to study the variation in sampling results with time and the transient effects of matrix loading. The results are shown in Figure 15. The penetration varied without any pattern for the first eight hours of the test and then began to rise. After 10 1/2 hours the superficial gas velocity could no longer be maintained at its original value because of the increased pressure drop, and the run was stopped after 11 1/2 hours. At the end of the run the matrix was carefully removed and weighed. The clean weight was 120 g, and a total of 81.8 g of dust had been collected. Assuming the total mass collection efficiency was constant over the 11 1/2 hour run (neglecting the small decrease in the last four hours), these results indicate that the matrix collected approximately 50 percent of its own weight in dust before the collection efficiency was appreciably affected. However, during this time the pressure drop across the matrix also increased by about 50 percent.

Preliminary Economic Estimates

A preliminary economic analysis was prepared based on the results obtained with the median packing density matrix (F = 0.0132). Satisfactory collection efficiencies were obtained with the median density matrix using superficial gas velocities of 6.1 to 10.6 m/s (1200 to 2090 ft/min). The choice of operating velocity involves a trade-off between operating and capital costs. A high velocity reduces the total flow area and thus the number of parallel collector modules, but results in a higher pressure drop and thus greater energy requirements for fan operation. Lower velocities have the converse effect. Cost estimates were made for a hypothetical system using either low or high velocity operation and taking into account the increased fan power requirements with higher pressure drop. The incremental costs of HGMS modules were evaluated on the basis of 2.13-m (7-ft) diameter modules each of which

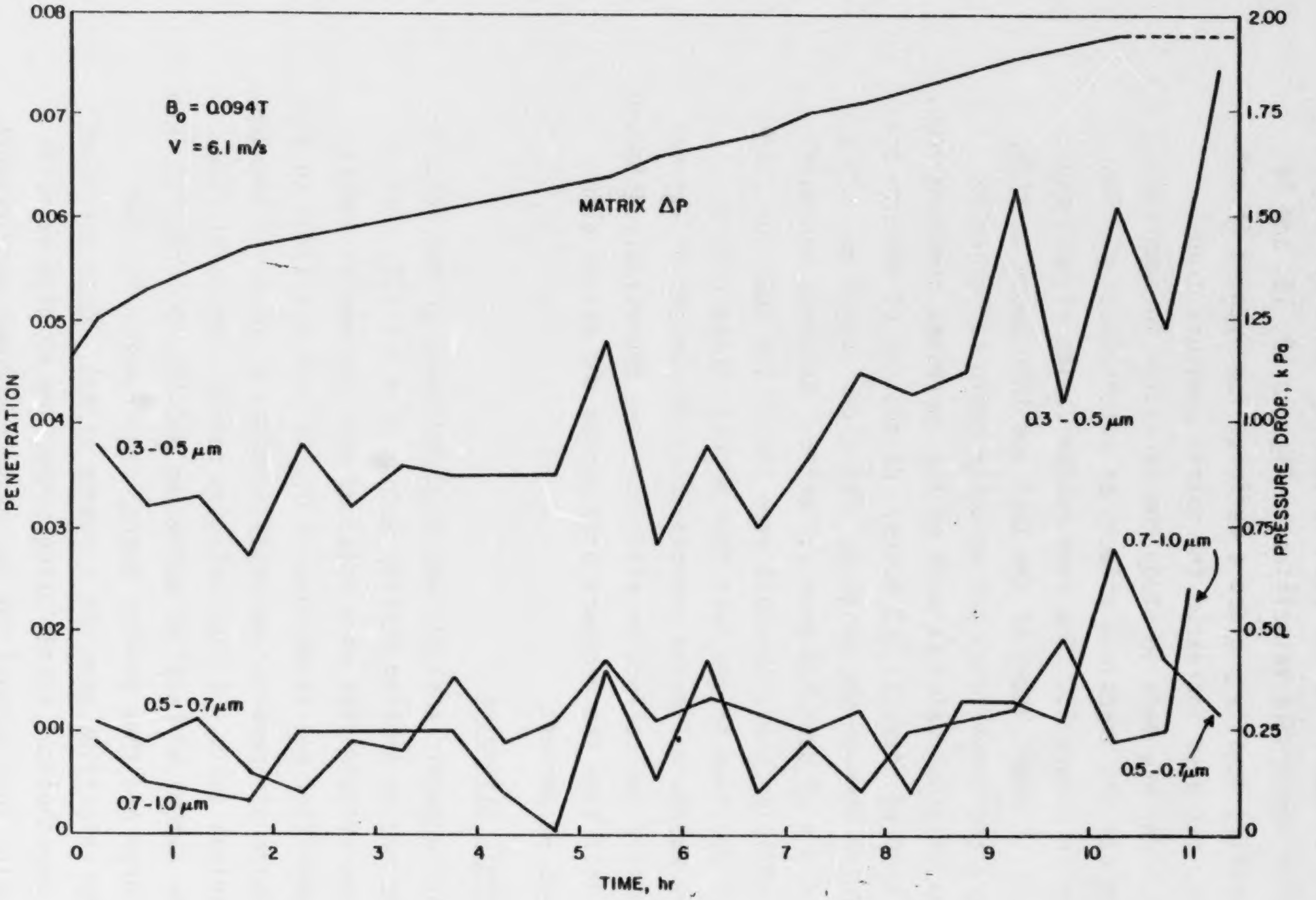

Figure 15. Bench-scale variation in collection efficiency and pressure drop with matrix loading.

would cost $240,000 (including the magnet, power supply, and heat exchangers) and would require 20 kW to produce a 0.2 T background field [75]. Since information on matrix cleaning was not yet sufficient to allow a detailed analysis of operating cycles, a 75-percent duty cycle was assumed (25 percent downtime on each module for matrix cleaning), which is comparable to commercial clay unit operation [10]. The results of the preliminary analysis are summarized in Table 4.

Both the cost and power requirement projections shown in Table 4 are slightly higher than the tentative goals stated previously, but are well within the range of potential feasibility. As mentioned previously, the cost of large-scale HGMS systems is not yet firmly established, and the process has not been optimized for gas-stream application so the cost projections could easily be ±50 percent. Also calculations indicate that the total energy requirement of the system could be reduced by using higher magnetic fields with lower matrix packing density (hence, lower pressure drop). In the low velocity case presented in Table 4, magnet energization accounts for approximately 32 percent of the total power requirement, and in the high velocity case, approximately 12 percent.

TABLE 4. PRELIMINARY ECONOMIC ANALYSIS FOR HGMS APPLIED TO BOF DUST CONTROL

	Low Velocity	High Velocity
Superficial gas Velocity, m/s	6.1	10.2
(ft/min)	(1200)	(2010)
Estimated Pressure Drop, kPa	1.2	2.5
(in H_2O)	(4.7)	(9.9)
Cost of HGMS Modules, $\$/m^3/s$	14,700	8,800
($/CFM)	(6.94)	(4.15)
Total Power Requirements, $kW/m^3/s$	2.9	4.7
(hp/1000 CFM)	(1.8)	(3.0)

At this stage in the program it became apparent that more detailed experimental results were needed on a larger scale system to expand the understanding of the process and to provide more extensive and reliable results on which to base economic projections.

DESCRIPTION OF PHASE II APPARATUS AND EXPERIMENTS

General Guidelines For Scale-Up

The bench-scale experiments provided a baseline of information and experience from which to design the larger system. The following guidelines for the design of both the pilot-scale apparatus and the experiment resulted.

(1) Contractual agreement stipulated a minimum system capacity of 0.235 m^3/s (500 CFM). To insure that this obligation could be met even if operating velocities had to be reduced in the larger system, a 30-cm diameter matrix canister was specified.

(2) A more systematic experiment was designed to allow analysis of variance and direct comparison of runs that differed by only one operating parameter.

(3) Operation at four velocities in the nominal range of 5 to 10 m/s was planned in an attempt to more accurately determine the velocity effect since it has an important impact on system optimization.

(4) The matrix packing density was reduced to yield lower pressure drops and a more equitable distribution of projected power requirements between the magnet and fans. Two matrix densities ($F = 0.005, 0.010$) were chosen for evaluation.

(5) A magnetic field capability of 0.5 T was specified. Zero-field operation was also planned to aid in the comparison of experimental data and theory.

(6) Two different types of dust were specified to broaden the information on potential applications. BOF dust from the same source as the bench-scale test was selected as one dust. A second dust was obtained from the hopper of a roof-system baghouse that controls emissions from electric arc furnaces at a Pennsylvania steel mill.

(7) Allowance was made for a matrix length of up to 30 cm. Two matrix lengths (L = 15, 30 cm) were selected for testing.

(8) Plans were made for limited testing at an elevated temperature to allow preliminary evaluation of temperature effects.

(9) Selection of operating parameter levels was purposely directed toward lower efficiency operation than that observed in the bench-scale tests to allow better observation of parameter effects. When collection efficiencies exceed 90 percent (penetration = 0.1) good repeatability of experiments is more difficult and parametric effects are more likely to be masked by random error.

(10) Cascade inertial impactors were specified as the primary means of particle size determination since their range of particle size information is broader than the available optical system and since impactors are more widely used in field sizing studies. Also the theoretical filtration and HGMS models are based on aerodynamic behavior of spherical particles, which is the same basis on which impactors are calibrated and operated. The optical system was also retained to provide preliminary results in near-real time and to allow observation of transients during extended runs.

Apparatus and Procedures

To avoid the duplication of costly equipment that was already available, the pilot plant was designed to operate as a slipstream off the existing Particulate Aerodynamic Test Facility located at the EPA Technical Center in Research Triangle Park, North Carolina. This facility basically consists of a low-speed, closed-loop wind tunnel. Incorporated with the wind tunnel is a dust feed and redispersion system that operates on the same fluidized-bed principle as the system used in the bench-scale experiments. (In fact, the bench-scale system was designed as a scaled-down model of the EPA facility.) The wind tunnel is also equipped with a baghouse that results in once-through operation with respect to dust. The entire system is described in detail elsewhere [81,82], and the description will be repeated here only to the extent that it pertains to the Phase II experiments.

The experimental apparatus is shown schematically in Figure 16. The fluidized bed in this system had two separate stages. The lower-bed was 20 cm in diameter and contained 2.5 cm of 6-mm glass beads. It was operated at incipient fluidization to break up the dust initially as it was fed in by the screw feeder. The dust then sifted up through a screen to the 40-cm upper bed, which contained approximately 2.5 cm of no. 9 lead shot and 2.5 to 5 cm of 700-μm glass beads. The larger diameter of the upper bed lowered the gas velocity so that the glass beads were fluidized but not elutriated, and the lead shot was near incipient fluidization. The upper bed further broke up the dust agglomerates. Some early effort was devoted to optimizing the gas flow rate and bed depths with an objective of maximizing the percentage of fine particles in the output, but little success was achieved. The bed depths were finally set at the above values, and the fluidizing gas flow was set at roughly 0.14 m^3/s (300 CFM). These conditions provided the most trouble-free operation and yielded a steady particle output with roughly 1 percent smaller than 1 μm ($\rho_p = 4.5\ g/cm^3$).

From the fluidized bed the dust was blown into the 61-cm diameter wind tunnel where it was mixed with dilution air coming from the baghouse and wind tunnel fan. A slipstream of the dusty air was then drawn off the wind tunnel into the pilot-scale HGMS apparatus. The stream passed through a cyclone separator, which was designed to provide a 50-percent cut point (D_{50}) of approximately 5 μm ($\rho_p = 4.5\ g/cm^3$). The combination of superisokinetic flow at the slipstream intake and scalping by the cyclone reduced the percentage of large agglomerates in the gas stream. The characteristics of the stream exiting the cyclone varied

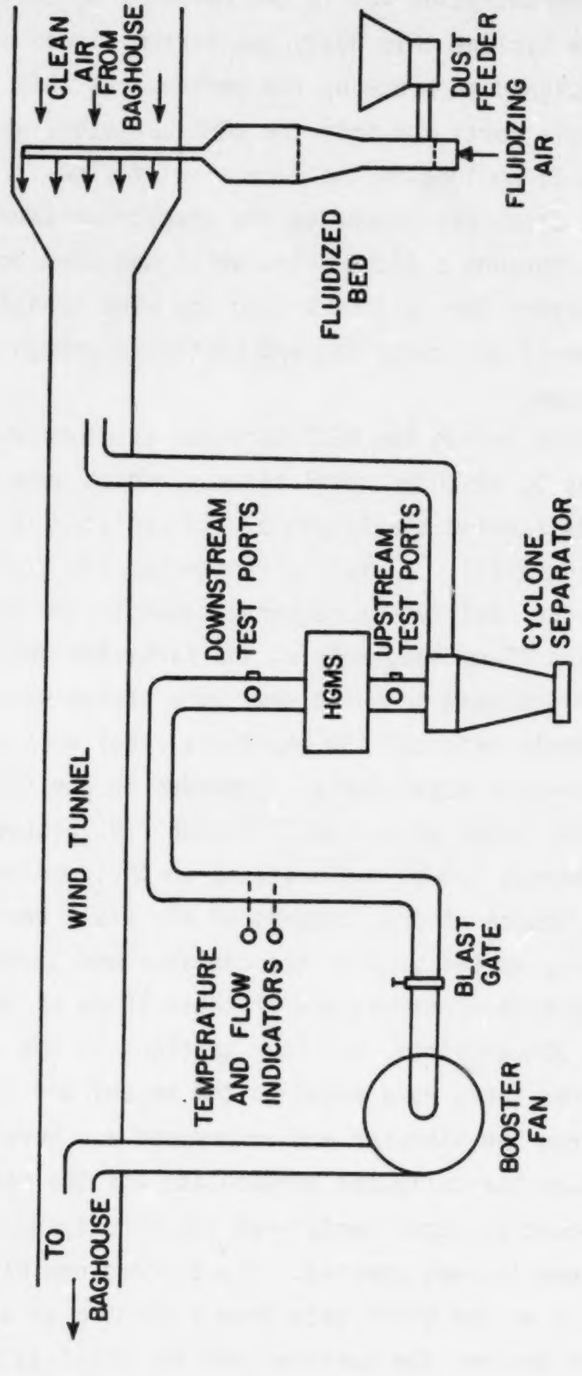
CLEAN AIR FROM BAGHOUSE
DUST FEEDER
FLUIDIZING AIR
FLUIDIZED BED
DOWNSTREAM TEST PORTS
UPSTREAM TEST PORTS
CYCLONE SEPARATOR
HGMS
WIND TUNNEL
TEMPERATURE AND FLOW INDICATORS
BLAST GATE
BOOSTER FAN
TO BAGHOUSE

Figure 16. Schematic representation of pilot-scale HGMS facility.

from run to run with the slipstream flow rate, but typically the mass median diameter was on the order of 2 to 4 μm (ρ_p = 4.5 g/cm^3) and the total mass concentration was in the range of 50 to 100 mg/m^3.

From the cyclone this dusty gas stream flowed up through a baffle which was designed to break up the vortex. It then flowed past the upstream sample ports and into the HGMS canister, which was 30 cm in diameter and 35 cm long in the direction of flow. From the HGMS canister the clean gas passed by the downstream sample ports; through a return bend; through a blast gate, which was used for flow control; through a booster fan; and back into the wind tunnel where it rejoined the remainder of the dusty gas and continued around the wind tunnel loop to the baghouse.

The matrix inside the HGMS canister was subdivided into four 7.5-cm long sections by expanded metal screens, which were connected by three threaded rods running the length of the canister in the direction of flow (see Figure 17). A small air-operated vibrator was attached through the duct wall via a rubber grommet to one of the threaded rods. To construct a 15-cm long matrix, the first and third sections (counting from the upstream or inlet end) were packed with the appropriate mass of randomly oriented 430 stainless steel wool of the same type used in the bench-scale experiments. Imbedded in the first section were two 20-cm diameter loops of 0.6-cm (1/4-inch O.D.) copper tubing. The loops each had numerous 1.5-mm perforations on their underside and were connected to a source of dry, compressed air via a vertical section of tubing running up the side of the canister and through the duct wall. The third section contained one of these loops of perforated tubing. To construct a 30-cm matrix, all four sections in the canister were employed, and perforated tubes were added to the second and fourth sections. After each run the vibrator and compressed air were used in tandem to shake and blow the collected particulate off the matrix.

To conduct an experimental run the wind tunnel was started up and the slipstream fan was started. The desired nominal velocity was set by adjustment of the blast gate from a reading on a stationary pitot tube located between the canister and the blast gate. A 16-point pitot

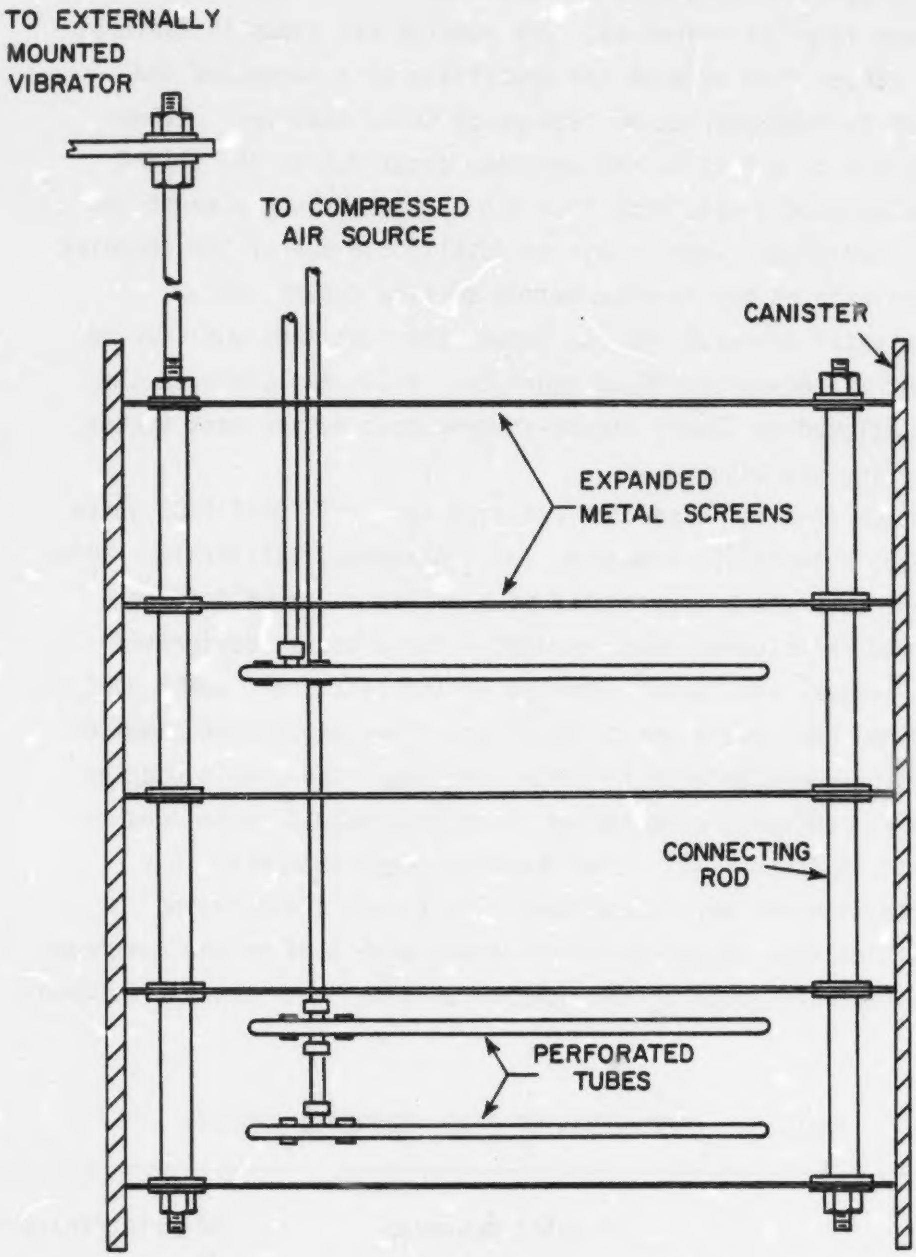
TO EXTERNALLY MOUNTED VIBRATOR
TO COMPRESSED AIR SOURCE
CANISTER
EXPANDED METAL SCREENS
CONNECTING ROD
PERFORATED TUBES

Figure 17. HGMS matrix construction and cleaning apparatus.

traverse (eight points on each of two perpendicular diameters) was then run at the downstream test ports. A special test was conducted early in the program to compare the upstream and downstream average velocities as well as 16- and 32-point traverses. The results are shown in Table 5. The apparent larger flow rate on the downstream side suggested the possibility of in-leakage, but no leakage could be detected. It was more probably due to a bias on the upstream pitot due to the slight swirling flow component remaining from the cyclone. In any event the results were considered close enough to justify the use of the 16-point downstream traverse as the routine method of flow determination.

When the pitot traverse was completed, the dust feed was started, and the magnet was energized if appropriate. A 10- to 15-minute time interval was allowed to insure steady-state output by the dust system, and then sampling was begun.

The cascade inertial impactors utilized were MRI Model 1502 units manufactured by Meteorology Research, Inc., Altadena, California. Prior to use the MRI substrates were coated with a thin layer of Apiezon L gease dissolved in toluene, baked at 120° C for 2 hours, desiccated overnight or longer, and tared. Because of the relatively small duct diameter (30 cm) and upward direction of gas flow, extractive sampling was judged to be preferable to in-stack sampling. The sample nozzles and probes were specially constructed using recommended techniques to minimize particle losses [83]. The impactors were supported in a horizontal position and were moved carefully to avoid dislodging collected particulate. Eight-point traverses were used on the upstream side and 12-point traverses on the downstream side, both divided between

TABLE 5. COMPARISON OF PITOT TRAVERSE RESULTS

	16-point traverse	32-point traverse
Upstream	7.57 m/s	7.39 m/s
Downstream	7.84 m/s	7.82 m/s

two perpendicular diameters. Downstream sampling was started first and lasted 96 minutes. Upstream sampling was then begun and lasted 32 or 48 minutes. Each of the impactors was operated with a nozzle and sample rate combination calculated to yield isokinetic sampling at the downstream average velocity.

After the runs the impactors were carefully dismantled, and the substrates were desiccated overnight before weighing. The probes were washed with acetone, and the probe washings were dried and also desiccated overnight. All of the weights were determined to 0.01 mg. A Mettler Model H51AR balance was used for the runs conducted prior to May 17, 1977, and then a new Perkin-Elmer microbalance, Model AD-2Z was placed in service for the remainder of the tests. The probe washings averaged 7.7 percent of the total collected mass on the upstream side and 13.0 percent on the downstream side. This particulate matter was most probably made up of larger particles lost in the probe bend. Data from the first two impactor stages (particle diameters of about 5 μm and above) were not included in the data analysis.

The cut points (D_{50}) of the impactor stages were calculated using the latest recommended EPA procedures [84], including published calibration factors for the MRI impactor stages [85]. Particle densities of 4.47 g/cm^3 for the BOF dust and 4.61 g/cm^3 for the EAF dust were determined from helium pyknometer measurements (courtesy of Mr. Ray Grote of EPA) and were used in the D_{50} calculations. A value of $\rho_p = 1.0$ g/cm^3 is frequently used in D_{50} calculations and yields what is known as the aerodynamic particle diameter. However, in this case since the volume susceptibility was used in magnetic calculations, it was decided that the Stokes diameter based on the measured particle density would be a more representative measure of particle size. Hence, measured particle densities and Stokes diameters were used throughout the calculations.

Differential particle size distributions were calculated to reduce the upstream and downstream data to the same concentration basis. During the sampling, identical nozzles were used on both sample trains, and sample rates were adjusted so that D_{50}'s of corresponding upstream and downstream stages were equal (±7 percent). This technique avoided the use of curve fitting procedures and allowed the calculation of particle penetrations from a direct ratio of upstream and downstream differential distributions at corresponding impactor stages.

Optical particle counts in the ranges 0.3 to 0.5 μm, 0.5 to 0.7 μm, and 0.7 to 1.0 μm were also made using the same dilution system and Climet instrument employed in the bench-scale tests. In these experiments, however, the sample nozzles were turned upstream, and samples were drawn at a constant nozzle velocity of approximately 5.0 m/s for all runs. This resulted in sample rates from approximately isokinetic in the low-velocity runs to 50 percent isokinetic in the high-velocity runs. Four-point, single diameter traverses were made on both the upstream and downstream sides. To prevent large agglomerates from entering the diluter and causing spurious counts, a small cyclone with a D_{50} of approximately 1 μm ($\rho_p = 4.5$ g/cm^3) was located at the inlet of the diluter. The subisokinetic sampling rates, the single diameter traverse, and the presence of the cyclone could have created systematic errors in the optical data; hence, the impactor data were utilized for primary data analysis. The optical system was utilized to ensure that no upsets occurred during impactor sampling, to provide approximate efficiency results in near-real time, and to study transient effects during two special long-term matrix-loading tests.

When each run was completed, the dust feed and gas flow were shut off. The magnet was deenergized, and the vibration and blowing system was used to dislodge the collected particulate from the matrix and to cause it to fall down into the cyclone hopper. The gas flow was then restarted and the matrix pressure drop was compared to the value observed before the run to ensure that the matrix was clean. If necessary the cleaning procedure was completed. Difficulties were sometimes encountered in returning the matrix pressure drop to its original value. Frequently a net gain in pressure drop of 25 to 125 Pa (0.1 to 0.5 in H_2O) was observed. The small vibrator and blowing system were evidently not completely adequate to overcome the combination of residual magnetism and mechanical entrapment of dust. The matrix loading tests conducted later indicated that this problem probably was not severe enough to seriously bias the efficiency results, but the cleaning system should still be upgraded before any future work is undertaken.

Experiment Design

The overall layout of the pilot-scale experimental program is shown in Table 6. Practical constraints prevented a complete randomization of the experiments. Changes in matrix length or packing density necessitated a time-consuming dismantling of the system so the different matrix configurations were separated into blocks, which are separated by the dashed lines in Table 6. With each matrix, the magnetic field was always incrementally increased, since returning to a lower field could have introduced errors because of hysteresis. In each set of three or four runs with the same matrix and same field, the velocities were randomly ordered. A few preliminary runs were made to debug the equipment and establish operating procedures. The actual test plan was conducted between April 19, 1977, and July 18, 1977. In Table 6 a run number of 4201, for example, indicates the first run on April 20, while 4202 indicates the second run on the same day.

TABLE 6. EXPERIMENT DESIGN FOR PILOT-SCALE HGMS

Run No.	Particulate	Packing Density	Matrix Length cm	Magnetic Field T	Gas Velocity m/s	Temperature °C
4191	BOF	0.005	15	0	5.59	31.1
4201	BOF	0.005	15	0	8.21	30.6
4202	BOF	0.005	15	0	6.71	34.4
4211	BOF	0.005	15	0	9.79	30.8
4271	BOF	0.005	15	0.05	5.49	25.3
4272	BOF	0.005	15	0.05	8.06	32.5
4281	BOF	0.005	15	0.05	6.74	29.1
4282	BOF	0.005	15	0.05	9.93	33.9
5031	BOF	0.005	15	0.10	8.47	30.9
5032	BOF	0.005	15	0.10	5.63	35.3
5041	BOF	0.005	15	0.10	6.89	31.9
5042	BOF	0.005	15	0.10	10.20	36.7
5091	BOF	0.005	15	0.10	10.78	108.9
5101	BOF	0.005	15	0.10	8.52	109.4
5102	BOF	0.005	15	0.10	7.02	109.4
5111	BOF	0.005	15	0.10	5.46	109.7
5121	BOF	0.005	15	0.20	8.00	32.8
5131	BOF	0.005	15	0.20	6.71	33.0
5161	BOF	0.005	15	0.20	5.70	32.8
5171	BOF	0.005	15	0.20	10.16	33.9
5181	BOF	0.010	15	0	9.74	30.0
5182	BOF	0.010	15	0	5.94	39.4
5191	BOF	0.010	15	0	7.38	32.8
5192	BOF	0.010	15	0.05	5.71	37.8
5201	BOF	0.010	15	0.05	7.84	32.8
5202	BOF	0.010	15	0.05	7.17	38.3
5242	BOF	0.005	30	0	5.16	33.3
5251	BOF	0.005	30	0	7.65	29.3
5252	BOF	0.005	30	0	9.24	36.9
5261	BOF	0.005	30	0.05	7.53	30.9
5262	BOF	0.005	30	0.05	10.06	37.0
5271	BOF	0.005	30	0.05	10.70	31.1
5272	BOF	0.005	30	0.05	6.56	35.9
6011	BOF	0.005	15	0.10	5.68	30.9
6012	BOF	0.005	15	0.10	8.52	37.2
6021	BOF	0.005	15	0.10	10.30	32.5
6022	BOF	0.005	15	0.10	6.84	37.2
6031	BOF	0.005	15	0.10	6.76	30.3
6032	BOF	0.005	15	0.10	7.06	37.0
*6281	BOF	0.005	15	0.40	8.24	35.4
7111	EAF	0.005	15	0	8.45	34.7
7112	EAF	0.005	15	0	7.85	41.4
7121	EAF	0.005	15	0	10.96	36.4
7122	EAF	0.005	15	0.10	7.88	40.6
7131	EAF	0.005	15	0.10	11.12	35.8
7132	EAF	0.005	15	0.10	9.16	41.1
7141	EAF	0.005	15	0.20	7.63	35.6
7142	EAF	0.005	15	0.20	9.31	40.8
7151	EAF	0.005	15	0.20	10.76	33.1
*7181	EAF	0.005	15	0.40	8.21	36.7

* Matrix removed from canister, manually cleaned, and replaced before this run.

SECTION 6

PILOT-SCALE EXPERIMENTAL RESULTS

Since they predict the effects of individual parameters on collection efficiency, the theoretical models discussed in Section 4 provide a logical framework within which experimental results can be analyzed. In this section supportive data on matrix and particle characteristics are first presented, and then the comparison of individual runs with theory is presented graphically. This procedure not only provides a convenient means of presenting all of the experimental data but also gives an overview of the extent to which observed experimental results can be explained. The effects of individual operating parameters are then discussed in more detail.

SUPPORTIVE MATRIX AND PARTICLE DATA

The 430 stainless steel wool used as matrix material in these experiments is commonly used in HGMS systems. It is a very non uniform material, as evidenced by the photomicrographs shown in Figures 18, 19, and 20. Some fibers are reasonably well approximated by the idealized cylindrical geometry while others are more ribbon-shaped and still others are shaped nearly like a coil. The theoretical investigation of Stekly and Minervini [59] implies that to a first approximation the assumed cylindrical geometry should give reasonable predictions provided the diameter of the cylinder approximates the mean projected width of the actual fibers. However, Oberteuffer's [1] conclusions on the importance of matching fiber size to particle size to achieve maximum magnetic force implies the possibility of different effective mean fiber diameters for different particle sizes. An impractically large number of photomicrographs would be required to define a meaningful distribution of fiber sizes and shapes for incorporation into the theoretical expressions. Therefore, a single radius of 25 μm was selected for use

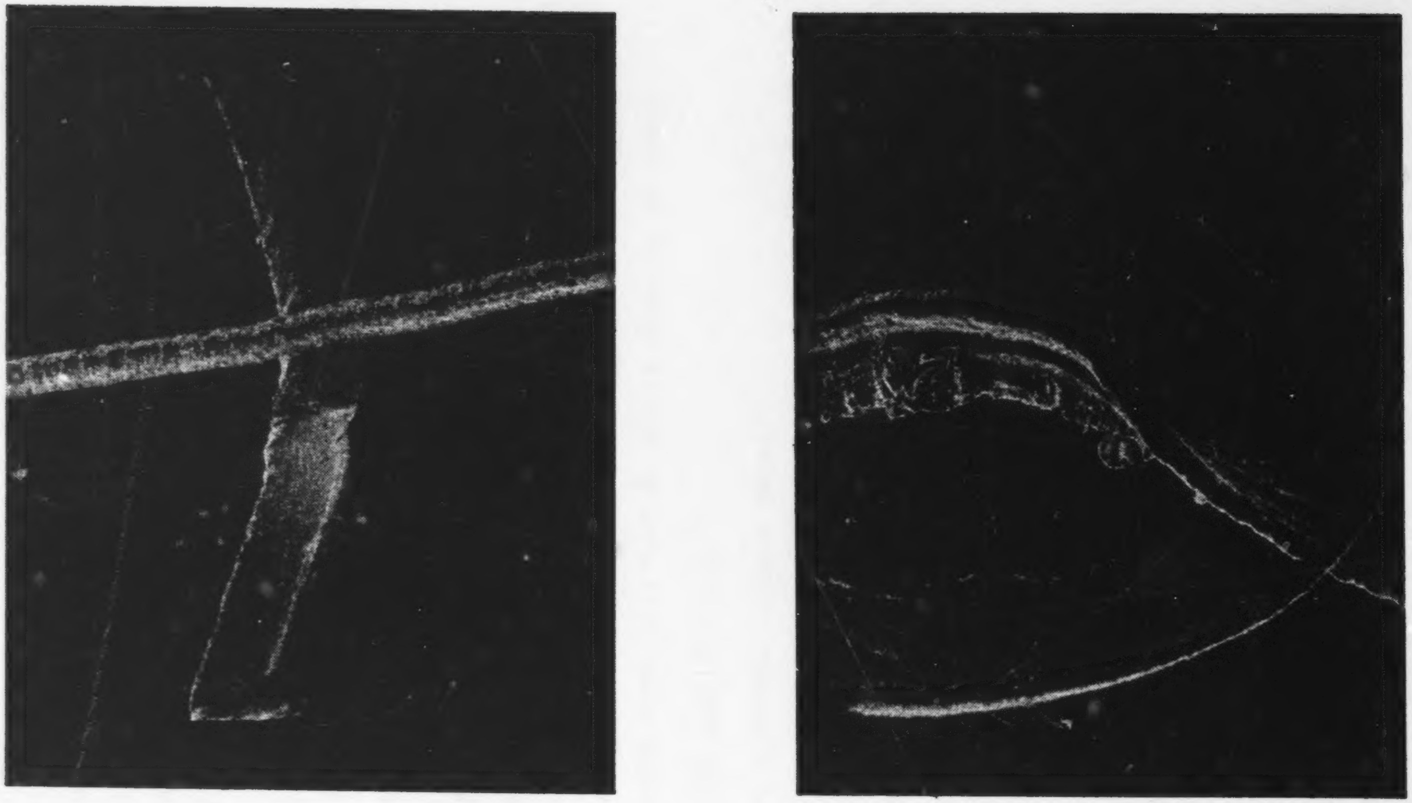

68X 100 μm

68X 100μm

Figure 18. Photomicrographs of stainless steel wool matrix fibers.

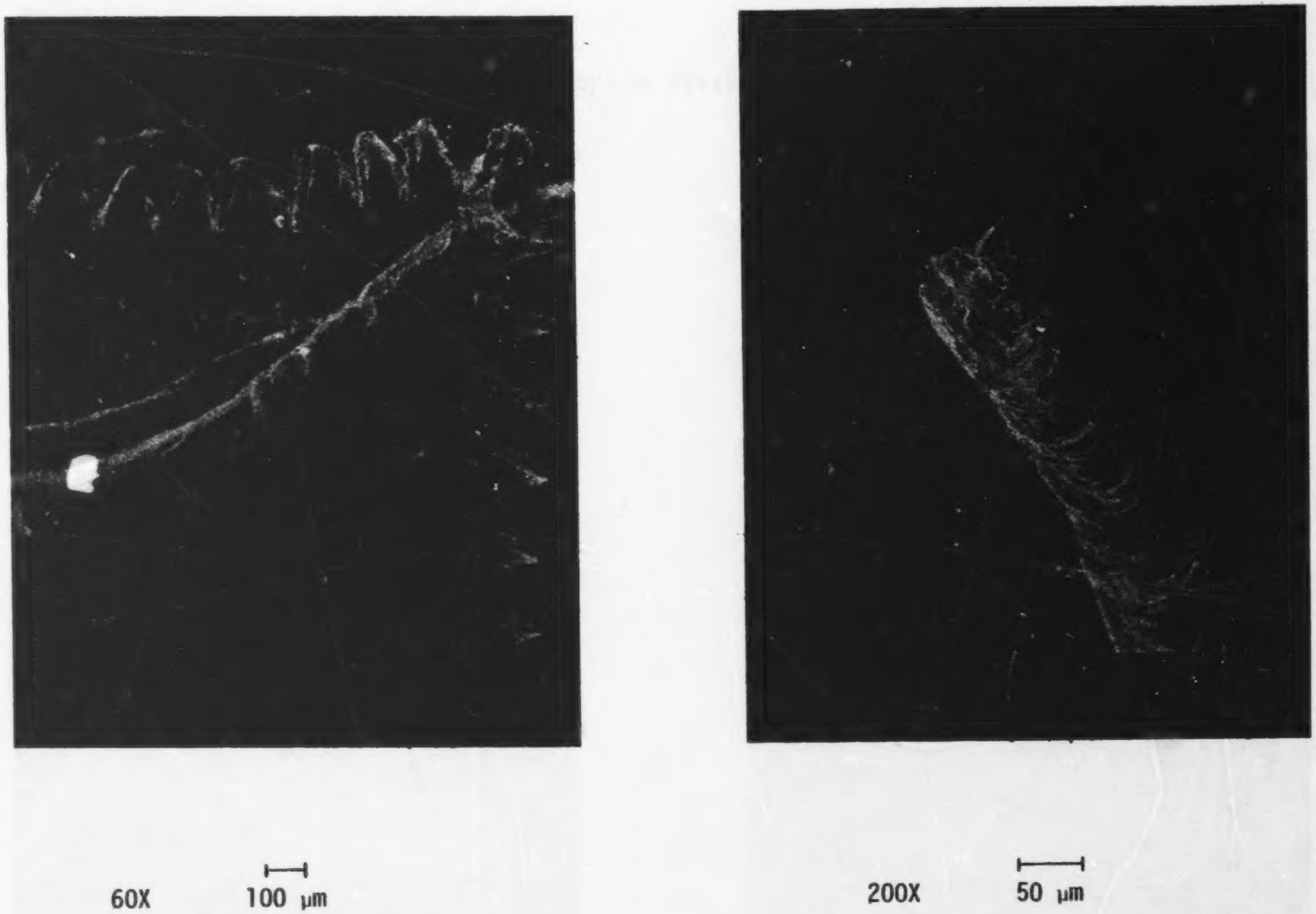

60X 100 µm

200X 50 µm

Figure 19. Photomicrographs of stainless steel wool matrix fibers.

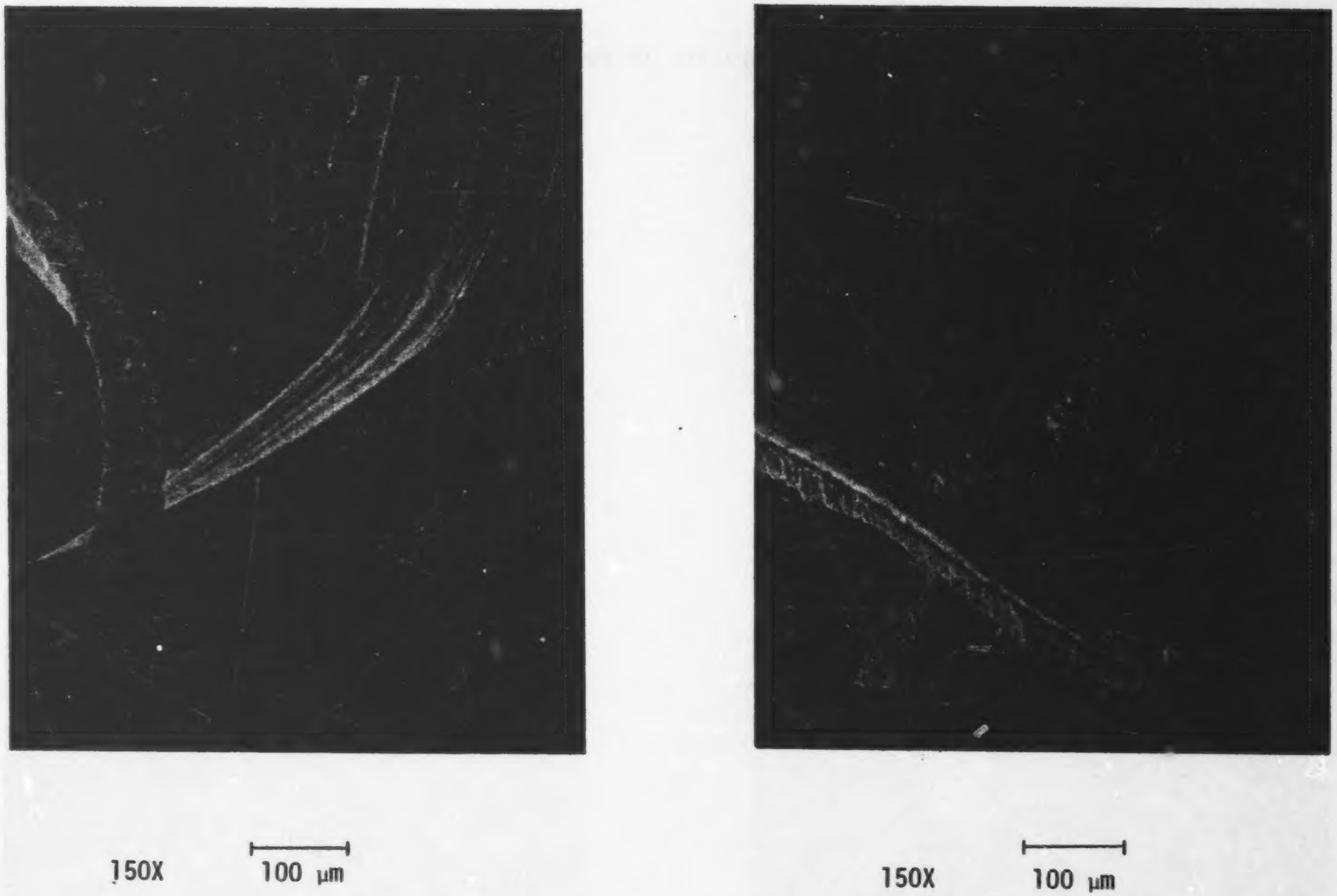
150X
100 µm
150X
100 µm

Figure 20. Photomicrographs of stainless steel wool matrix fibers.

in the models. This figure is reasonably consistent with the photomicrographs and results in good agreement between theoretical and experimental results.

Experimental magnetization measurements were also made on seven small samples of the steel wool material. The range and average of these measurements are shown in Figure 21. The variability of the magnetization results from inhomogeneities in the material, cold-worked effects, and the fact that the different samples had different shapes. In a total matrix a much higher applied field is required to saturate the steel wool. Also shown on Figure 21 are three points on the calculated in-matrix magnetization curve for a matrix packing density on the order of 0.01 [86]. The matrix eventually reaches saturation with an applied field on the order of 5.6 to 6.4 x 10^5 A/m (7 to 8 kOe) [41, 63].

With the low fields used in this work, the matrix was never saturated. To utilize the theoretical model, the near field correction parameter was thus calculated as

$$A = \frac{\mu_o M}{2B_o} \tag{31}$$

where M = estimated in-matrix magnetization from Figure 21.
The values of the parameter are given in Table 7 for the four fields used in the experiments.

TABLE 7. VALUES OF THE NEAR FIELD CORRECTION PARAMETER

Background Magnetic Field, tesla	$A = \frac{\mu_o M}{2B_o}$
0.05	2.39
0.10	2.26
0.20	1.98
0.40	1.54

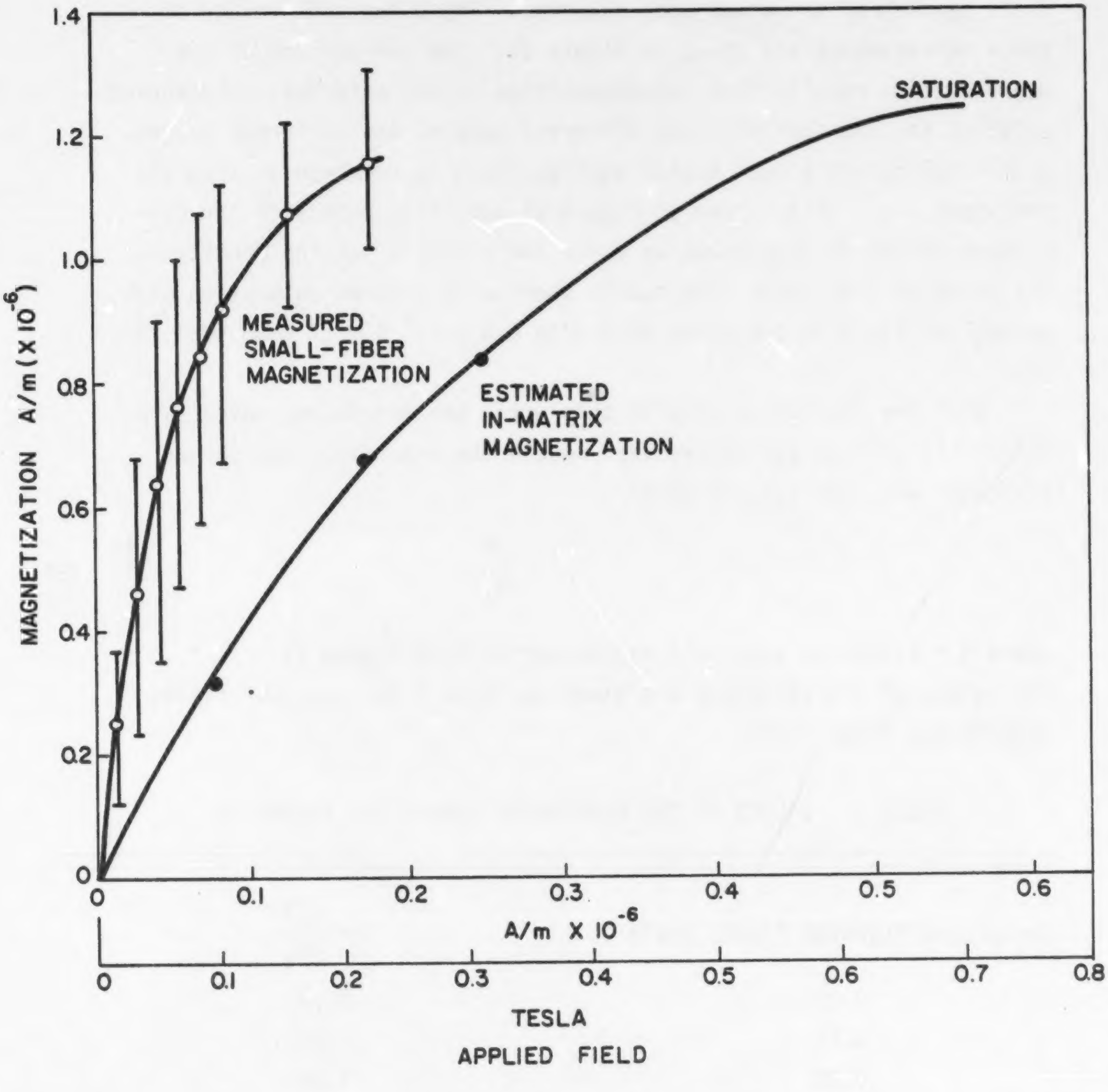

Figure 21. Magnetization curves of steel wool material and in-situ matrix.

Experimental determinations of particle magnetization were also obtained for each of the two dusts. The results are shown in Figures 22 and 23 for the BOF dust and EAF dust, respectively. For convenience the results are shown in the mass cgs units in which they were determined. The particle susceptibility is determined from these data by the equation

$$\chi = 4\pi\rho_p\sigma/H_o \tag{32}$$

where χ = volumetric particle susceptibility, dimensionless SI units
ρ_p = particle density = 4.47 g/cm^3 (BOF) or 4.61 g/cm^3 (EAF)
σ = specific magnetization, emu/g
H_o = applied field, Oe.

Figures 22 and 23 show that the susceptibility of both dusts is relatively large and is not constant with applied field. Rather than being weakly paramagnetic, both dusts exhibit relatively high permeability. Note that the magnetization of the BOF dust is about twice that of the EAF dust at any given field.

COMPARISON OF RESULTS WITH THEORETICAL MODELS

The no-field experimental data were fit to an equation of the form

$$P = \exp\left[-\frac{EFL}{a(1-F)}\left(\eta_i + \eta_o - \eta_i\eta_o\right)\frac{2\theta_c}{\pi}\right]. \tag{33}$$

With the fiber radius a = 25 μm and all of the operating parameters substituted into Equation (33), two adjustable parameters remain: E, the matrix effectiveness factor, and Á, the lumped adhesive force factor that is required for the calculation of θ_c. The matrix effectiveness factor would be affected by variations in the tortuous path that the gas stream must follow through the matrix. Under the idealized assumption of randomly oriented fibers which do not interfere with each other aerodynamically, a theoretical value of $4/\pi^2$ is predicted. In reality, the value of E that is required to obtain a good fit to the data is also influenced by the assumed mean fiber radius. The adhesive force

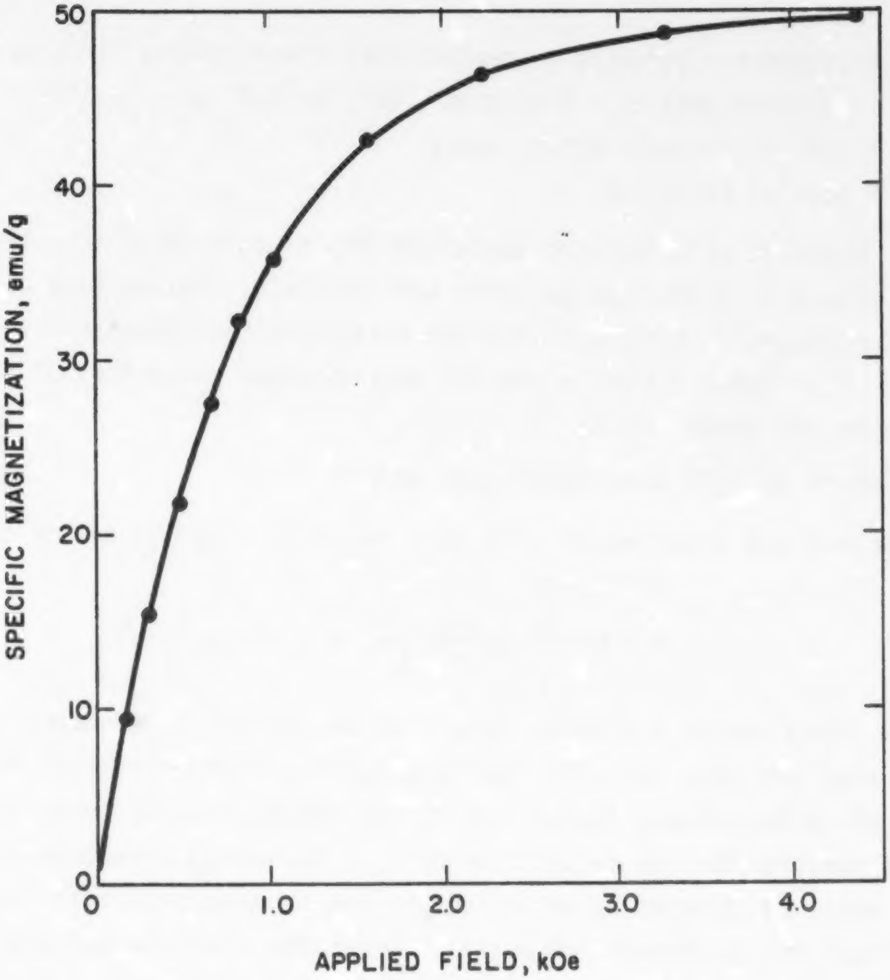

Figure 22. Magnetization curve of basic oxygen furnace dust.

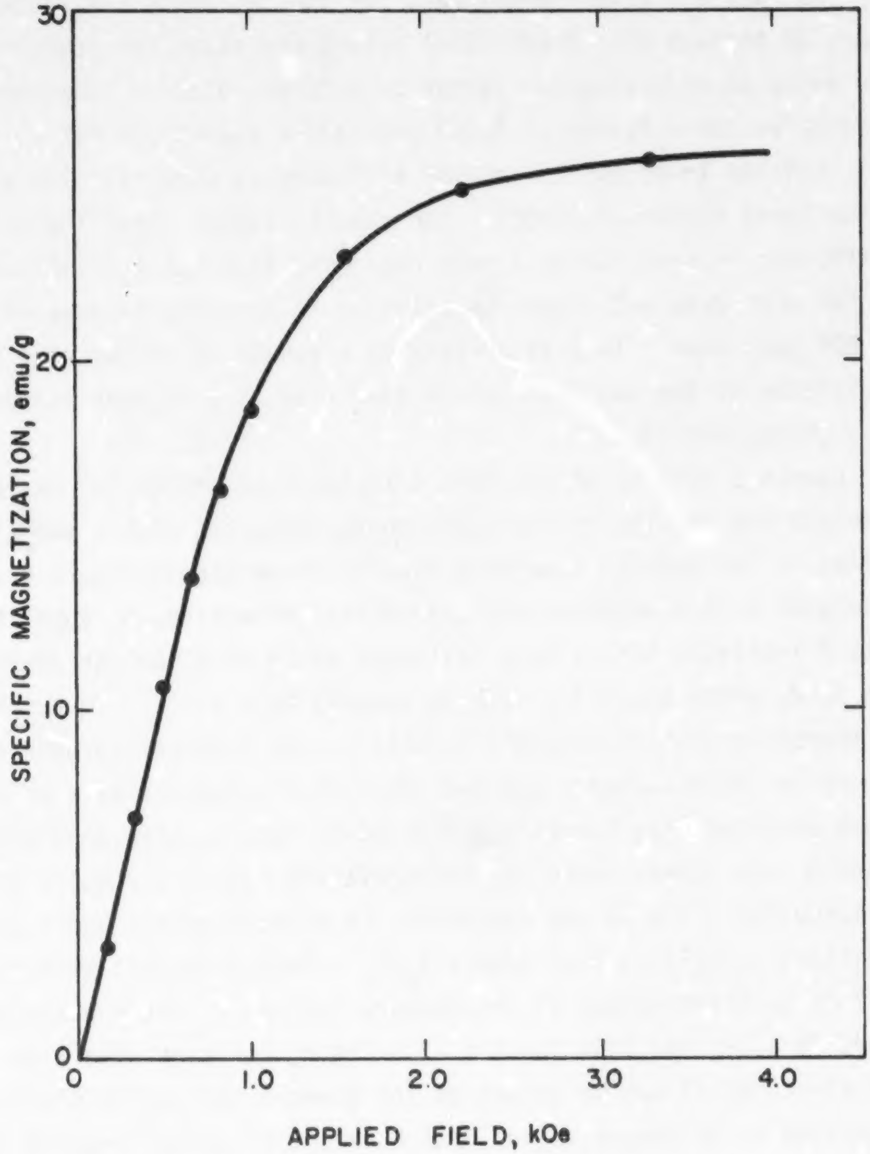

Figure 23. Magnetization curve of electric arc furnace dust.

factor was shown in Section 4 to have a predicted value in the range of 0.002 to 0.1 N/m.

The no-field experimental data for the two dusts are plotted in Figure 24 through 27. Theoretical curves are shown for comparison. For both dusts an effectiveness factor of 0.22 was used in Equation (33). An adhesive force factor of 0.003 provided a reasonable fit to the BOF data, and the lower EAF collection efficiencies were fit with an adhesive force factor of 0.0005. The results suggest that the rolling coefficient of friction is a more realistic approach and indicate that the EAF dust does not adhere as strongly to the wire fiber surface as the BOF dust does. This is presumably a result of differences in the composition of the two dusts which give rise to different Van der Waals force characteristics.

Lawson's version of the HGMS trajectory model [64,65] was used to correlate the results of the experiments conducted with a magnetic field applied to the matrix. Lawson's results presented in Figure 8 were calculated with a value of the near field correction, A, equal to 0.88. Table 7 indicates that a more realistic value of A for the lower field data is 2, while the 0.4 T data correspond to A = 1.5. To accomplish the transformation of Lawson's results to the appropriate near field correction, both Lawson's and Watson's [48,51] results were used. First it was verified that Lawson's and Watson's results are identical at low values to the Stokes number by interpolating Watson's results to obtain the curve for A = 0.88 and comparing the capture radius under identical conditions, recalling that $2AWK = V_m/V_o$. Then using Watson's results at A = 2.0, selected values of the capture radius, R_c, were positioned on Figure 28 along the line log K = -2. The R_c contours were then extended with slopes of -1 out to values of log K where the negligible inertia assumption is no longer valid. For $R_c = 1$ the contour remains straight for all K. The contours for $R_c = 4$ and 8 were completed accurately using additional Lawson results in the form log (AW) vs. log K [65] and his arguments that the separate parameter A has no effect on large R_c.

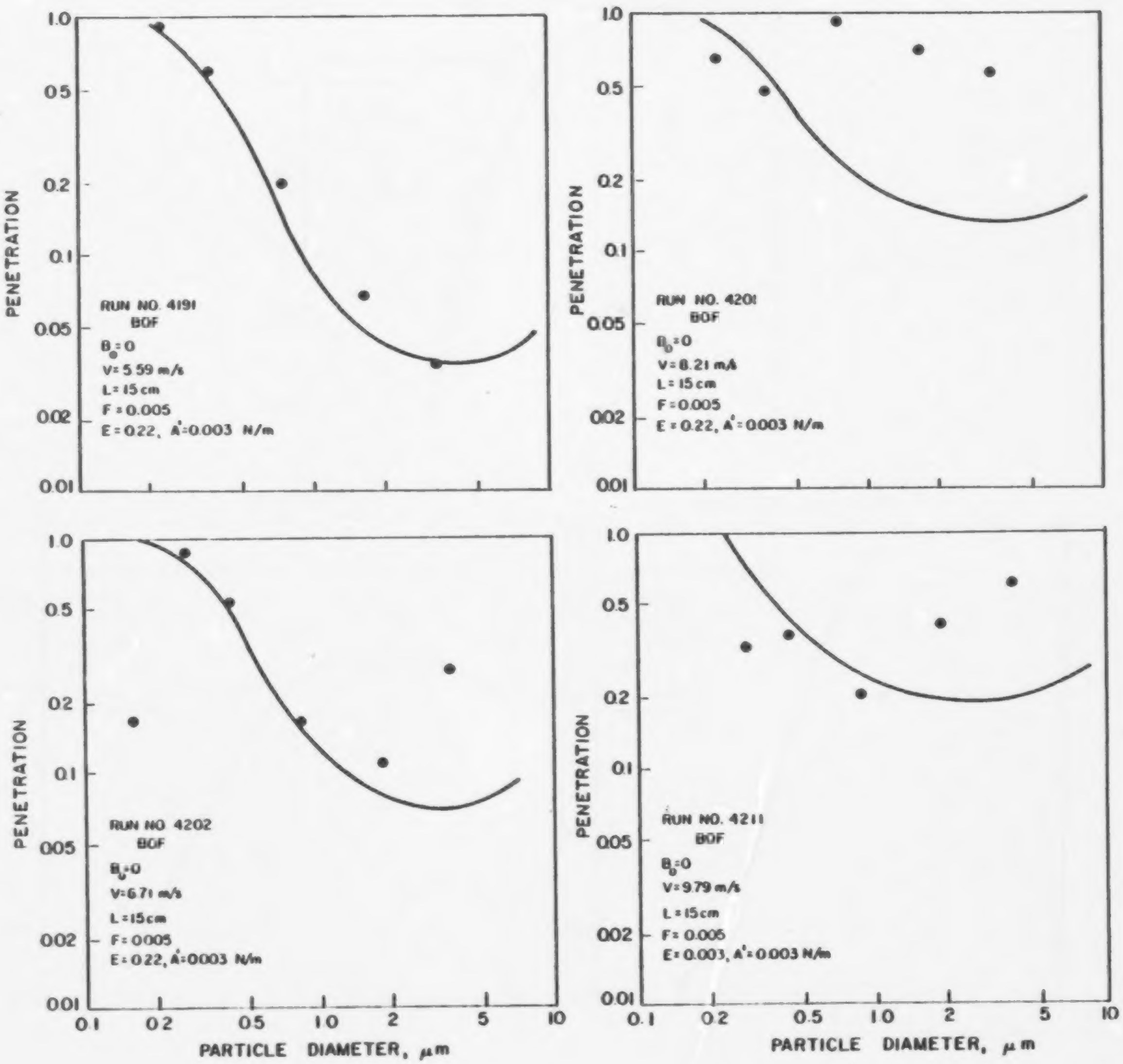

Figure 24. Zero-field pilot-scale results with BOF dust (F=0.005, L=15 cm).

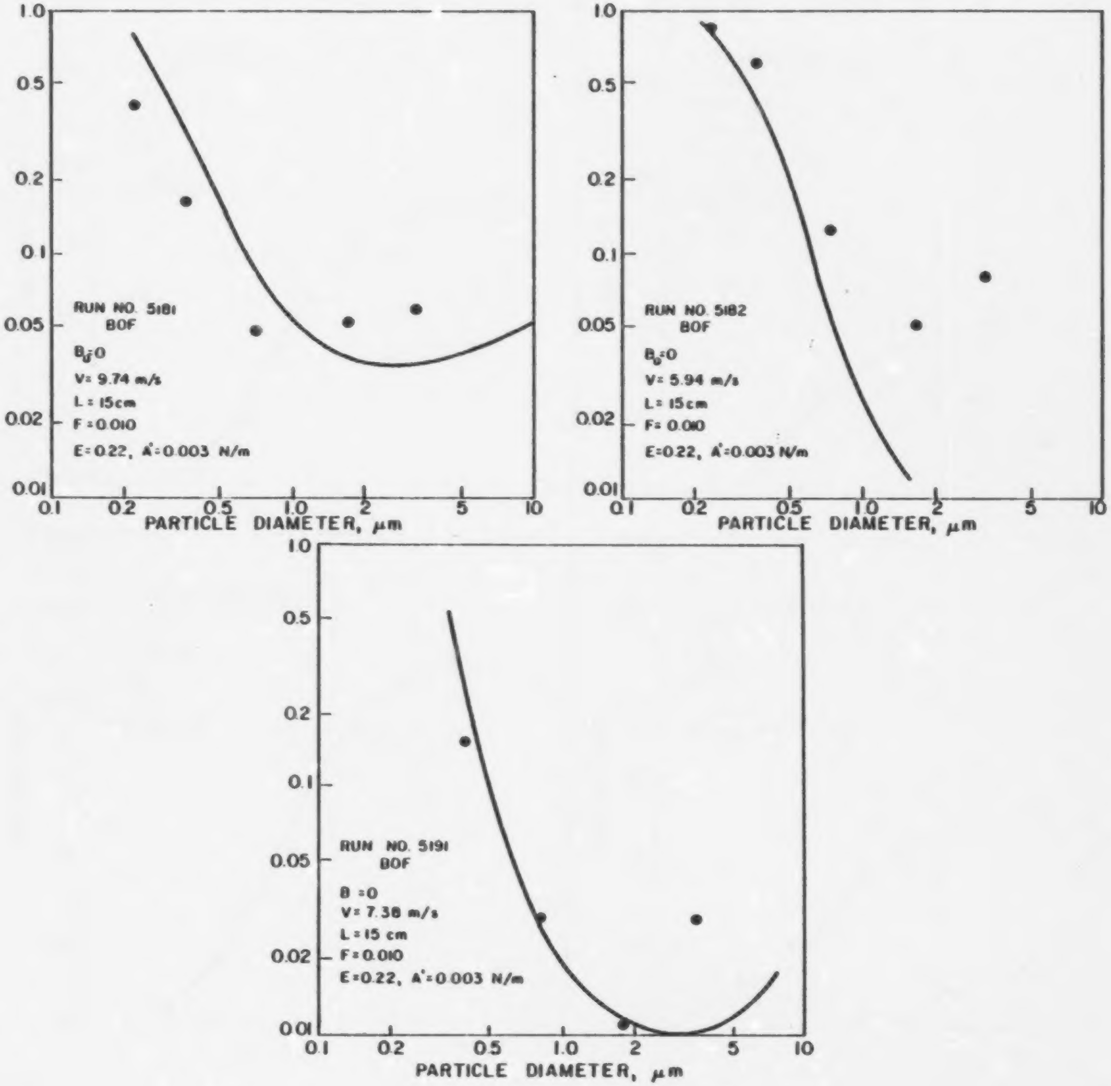

Figure 25. Zero-field pilot-scale results with BOF dust (F=0.010, L=15 cm).

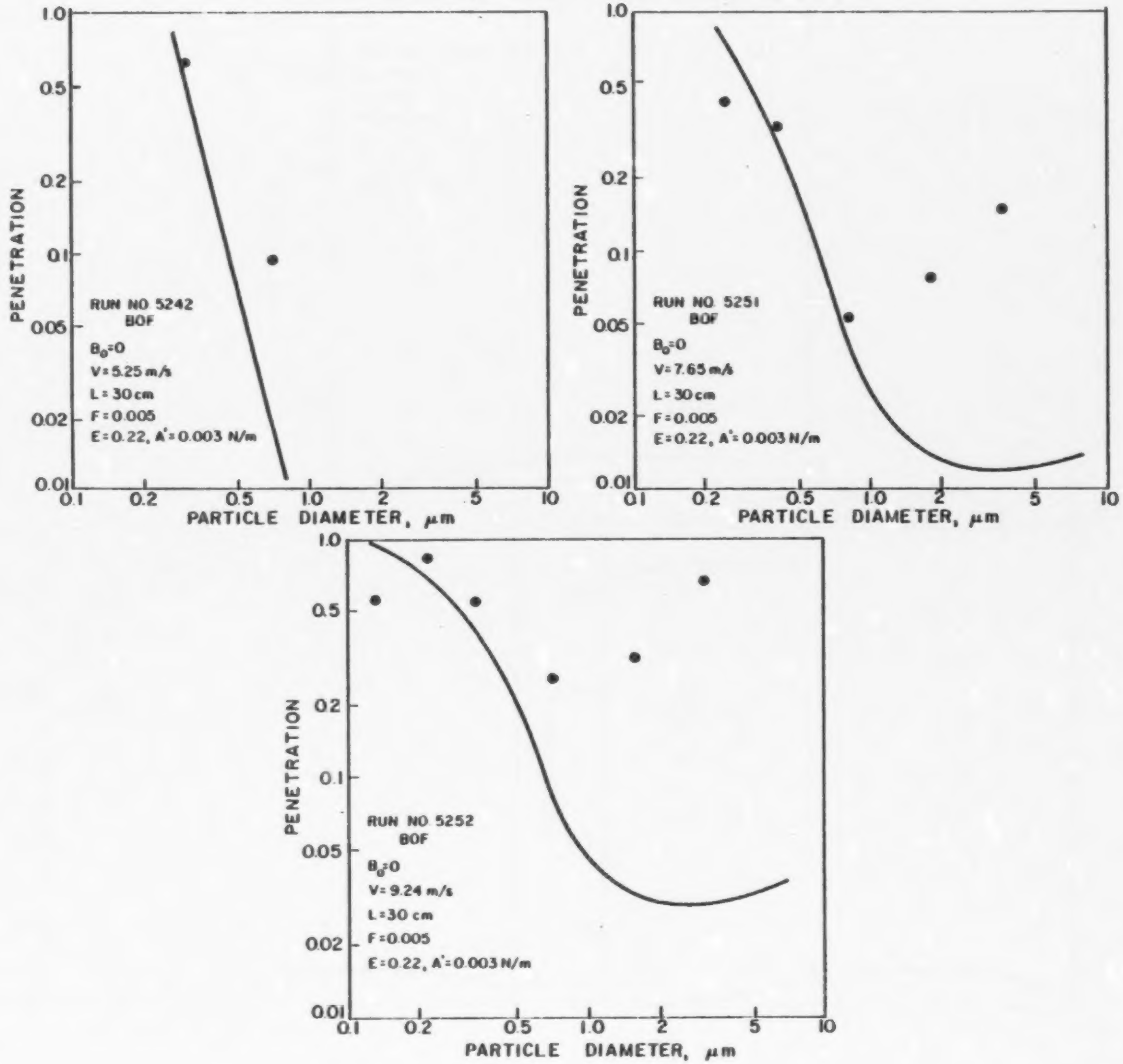

Figure 26. Zero-field pilot-scale results with BOF dust (F=0.005, L=30 cm).

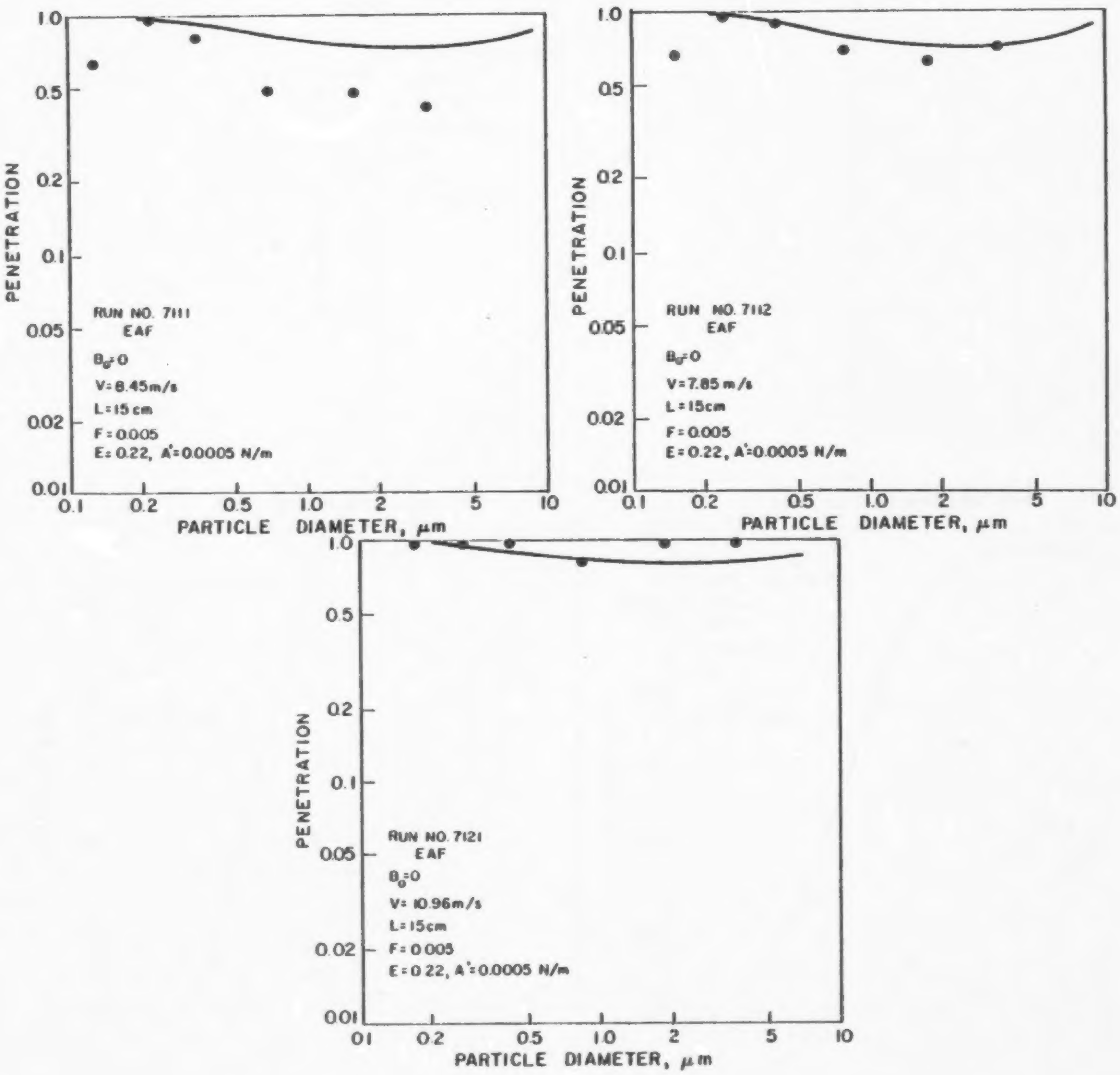

Figure 27. Zero-field pilot-scale results with EAF dust (F=0.005, L=15 cm).

The remaining contours were completed by extrapolating with approximately the same curvature as Lawson's curves at corresponding values of R_c. The extrapolated sections of the contours are shown as dashed lines in Figure 28. They have not yet been verified by trajectory calculations and should be regarded as approximate. A similar transformation was accomplished to model the two runs which were conducted at 0.4 T using a value of $A = 1.5$.

Theoretical curves for all of the HGMS runs were calculated using the expression

$$P = \exp\left[-\frac{EFL}{a(1-F)} \cdot R_c\right]. \tag{34}$$

The theoretical curves and experimental data are presented in Figures 29 through 39. The runs are presented basically in the order in which they were conducted except that the two 0.4 T runs are shown together in Figure 39. A fiber radius of 25 μm was used both in the determination of R_c from Figure 28 and where it appears explicitly in Equation (34). Equation (34) has one adjustable parameter, E, the matrix effectiveness factor. A value of $E = 0.09$ provided a good fit to the BOF data, while the EAF data indicated a lower value of $E = 0.07$.

It is reasonable to expect that the effectiveness factor might not be the same for the two dusts or for the same dust under with-field and no-field conditions. As argued above, the value of E is influenced by the assumed value of mean fiber size, by the validity of the assumed geometric orientation of the fibers, and by the assumption of no interference among neighboring fibers. In general all of these factors could be different with respect to aerodynamic and magnetic phenomena, resulting in different values of E for the with-field and no-field cases.

The differences in effectiveness factors for the two dusts with the field energized could be related to the matrix loading effects discussed by Luborsky and Drummond [53,56] and by Cowen, et al. [52,57,62]. The results of the matrix loading tests presented in Figures 40 and 41 provide additional information. Both of the matrix loading tests were

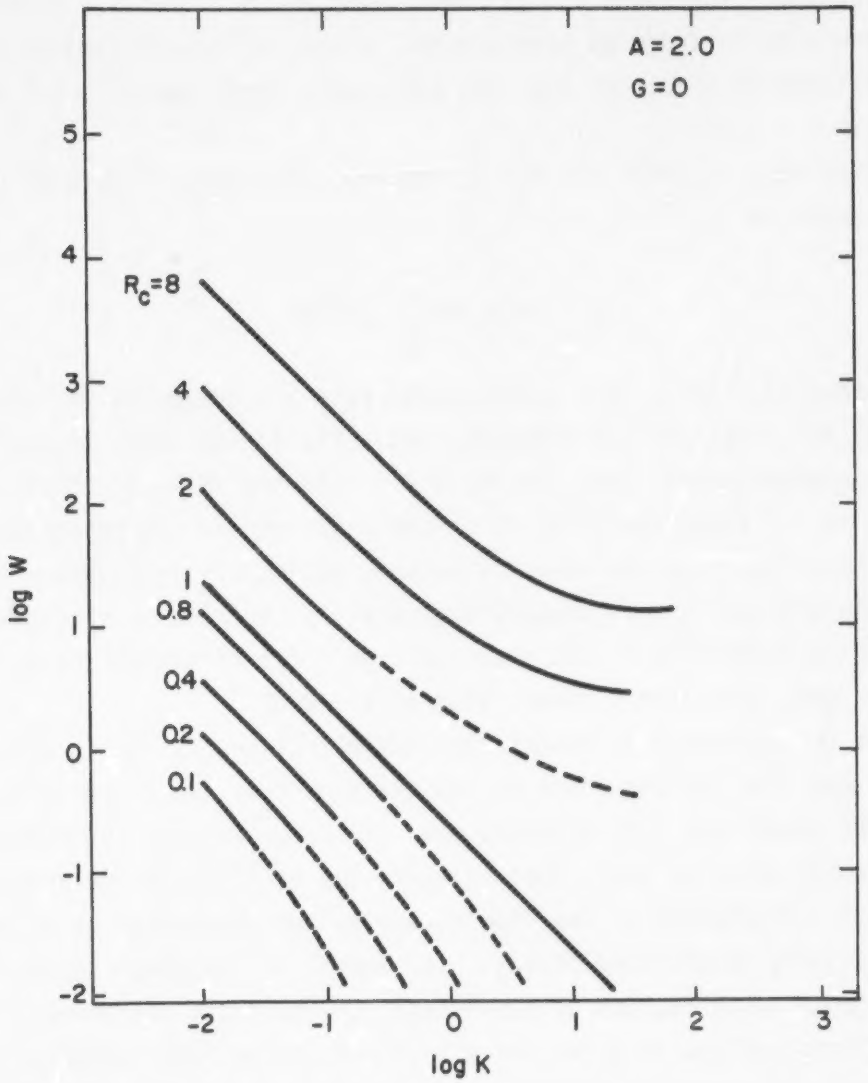

Figure 28. Lines of constant capture radius with inertial forces included and A=2.0.

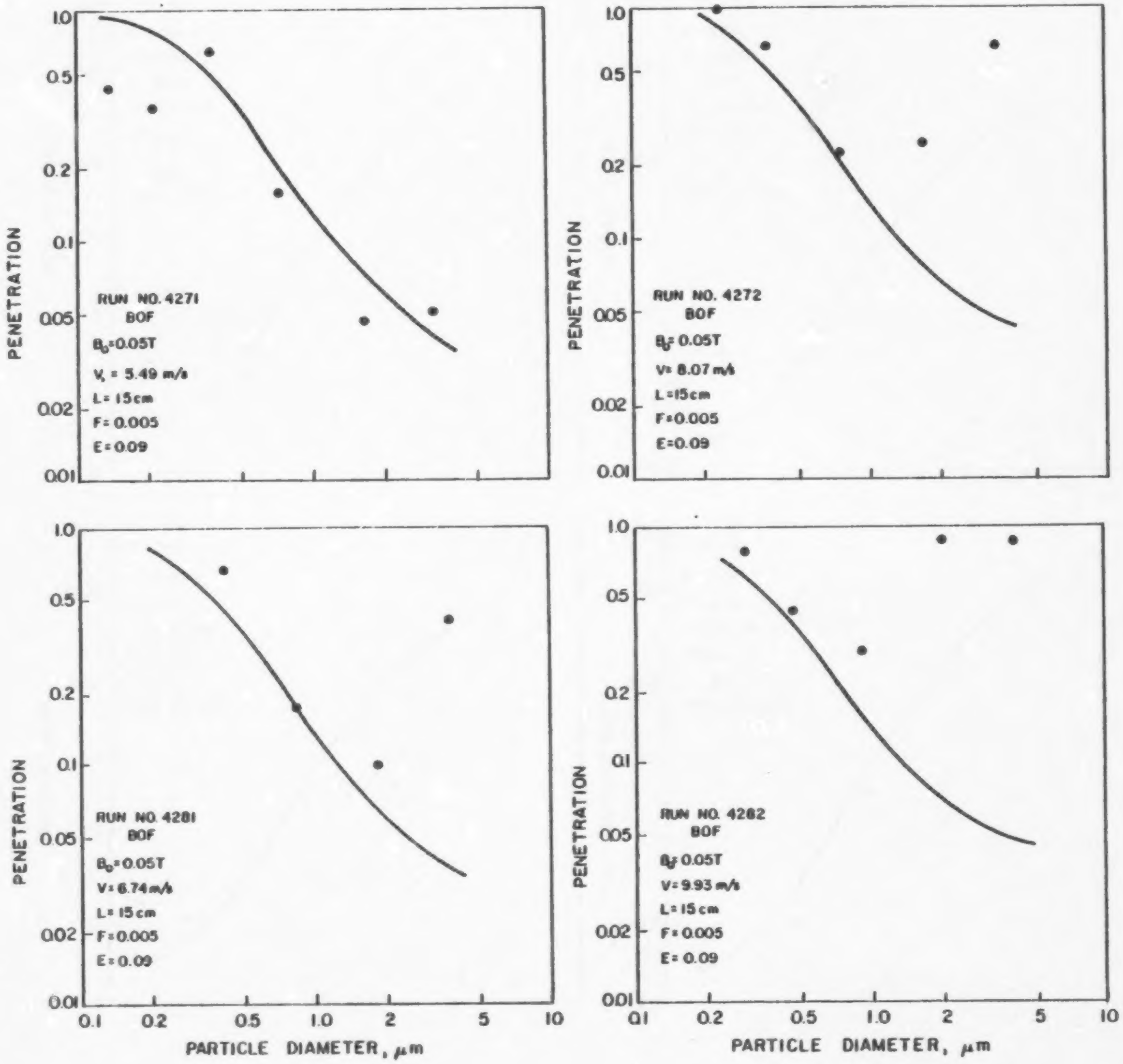

Figure 29. Pilot-scale HGMS results with BOF dust (B_0=0.05T).

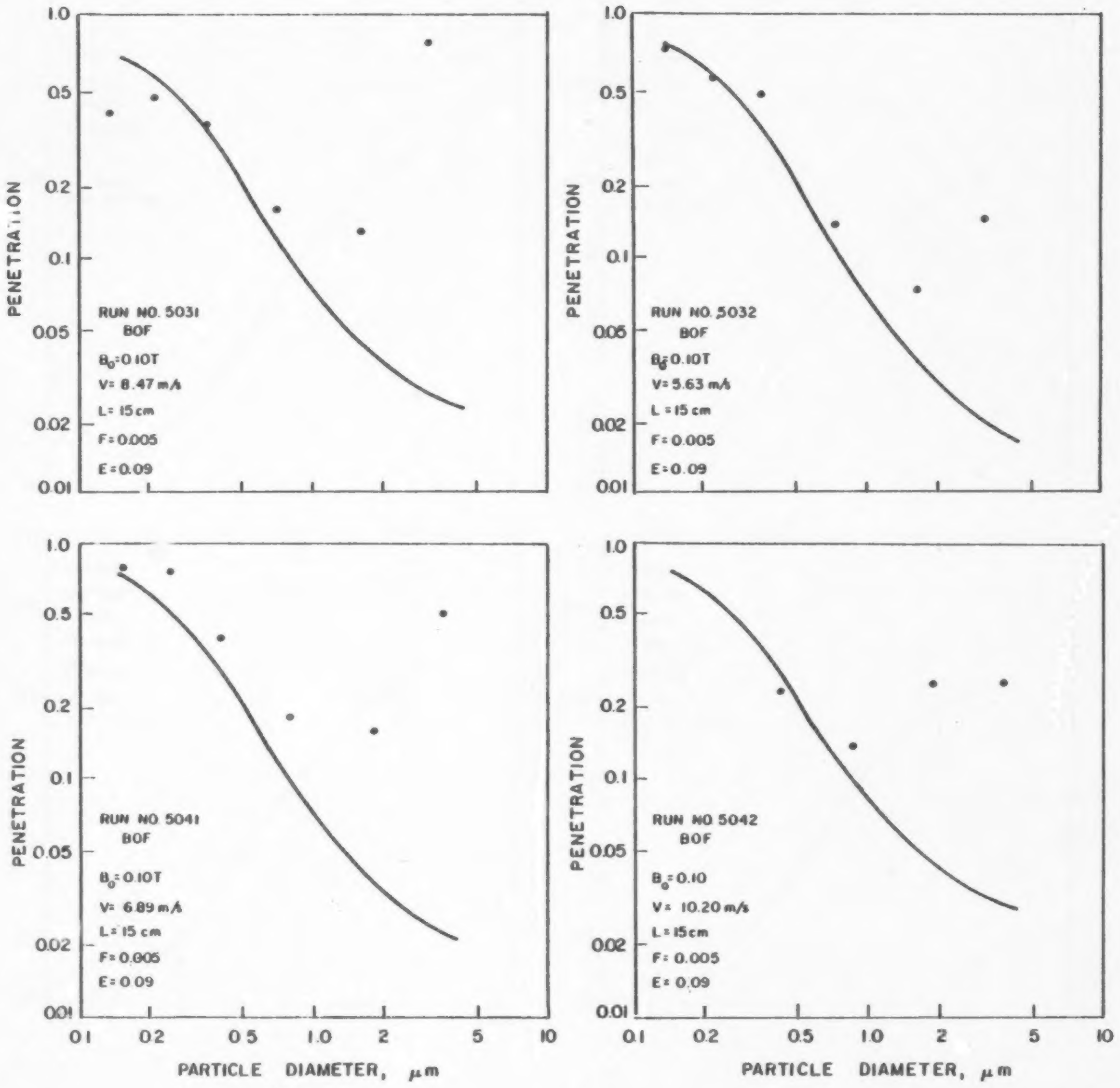

Figure 30. Pilot-scale HGMS results with BOF dust (B_0=0.10T).

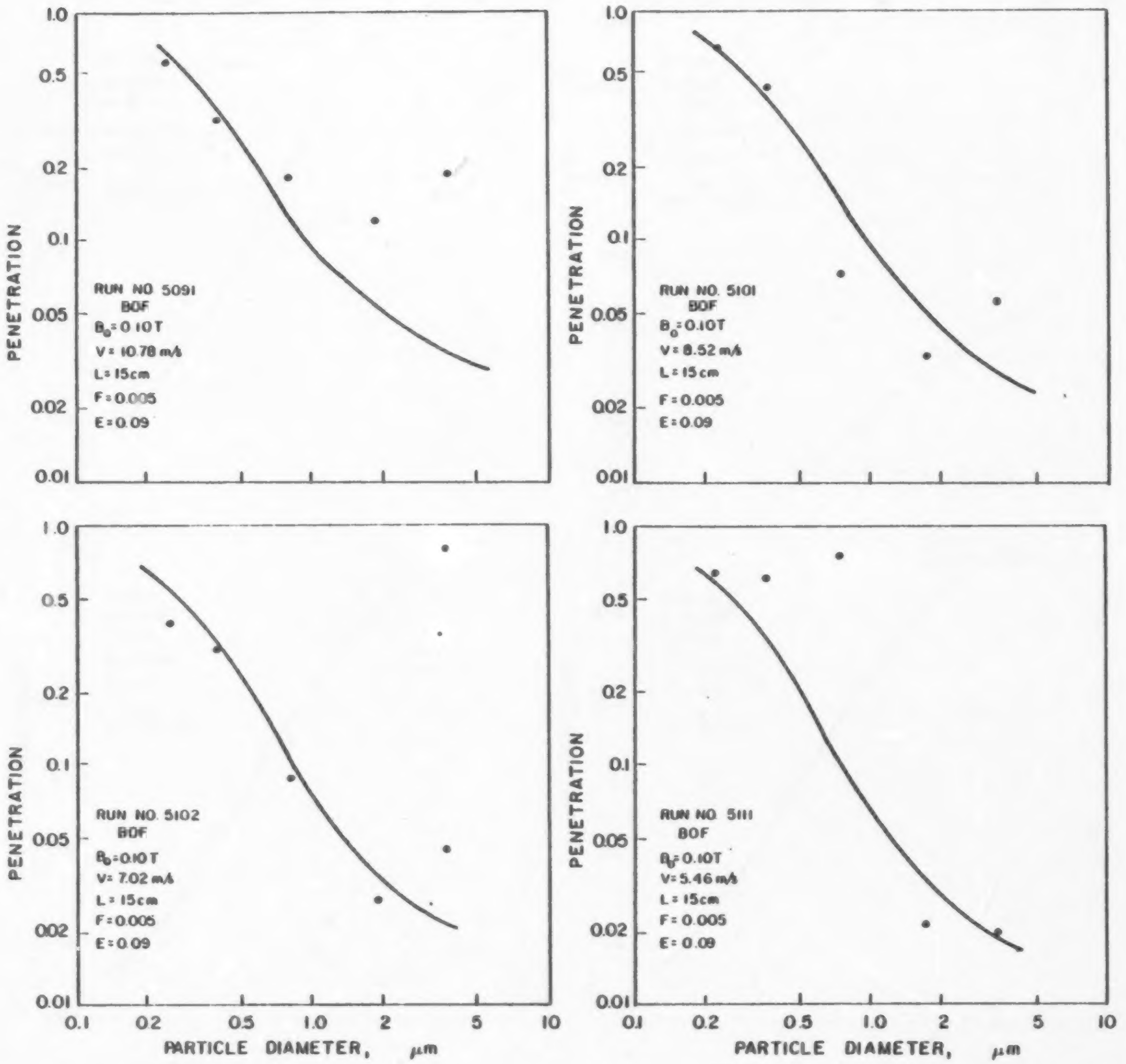

Figure 31. Pilot-scale HGMS results with BOF dust at elevated temperature.

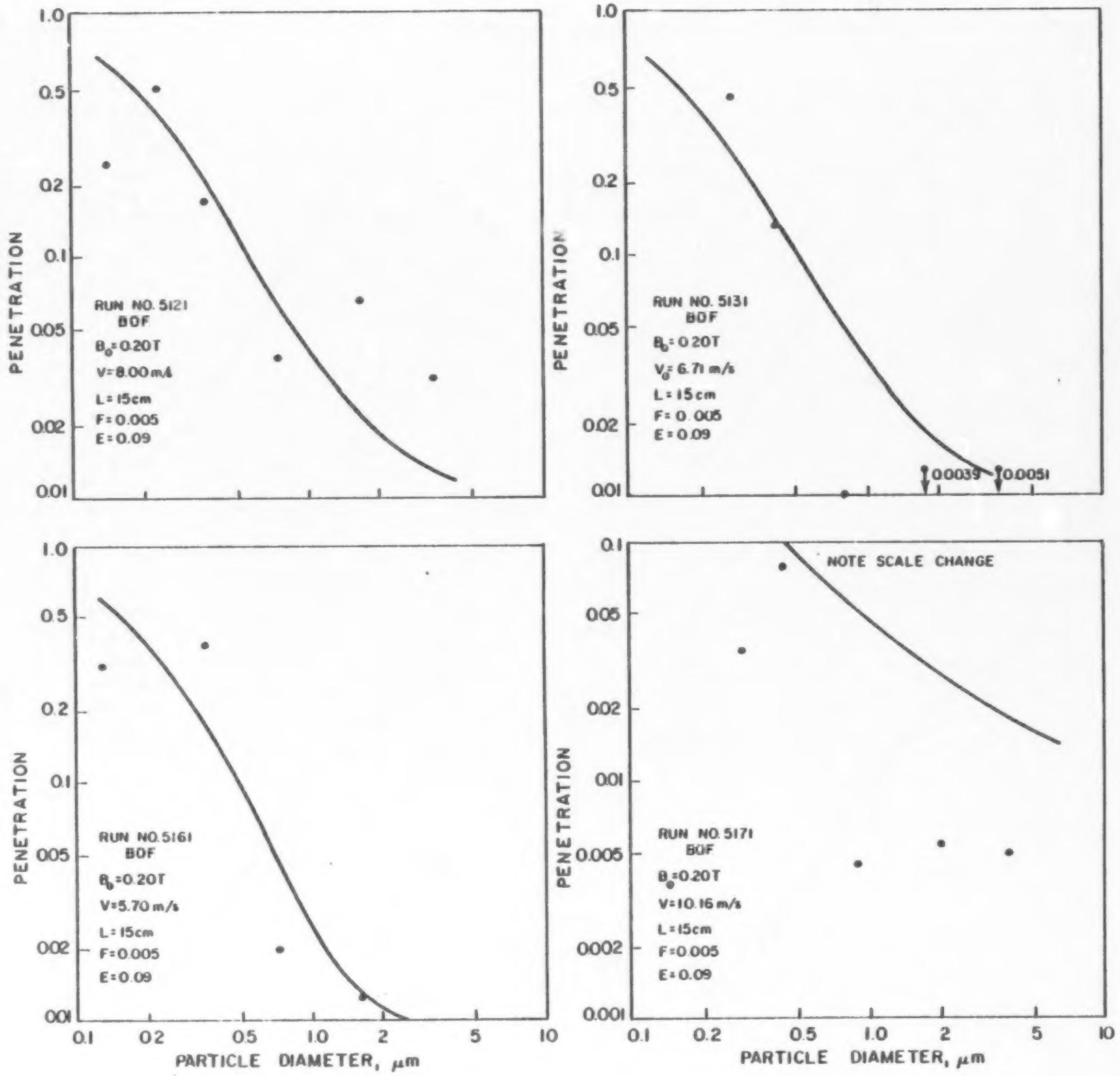

Figure 32. Pilot-scale HGMS results with BOF dust (B_0=0.20T).

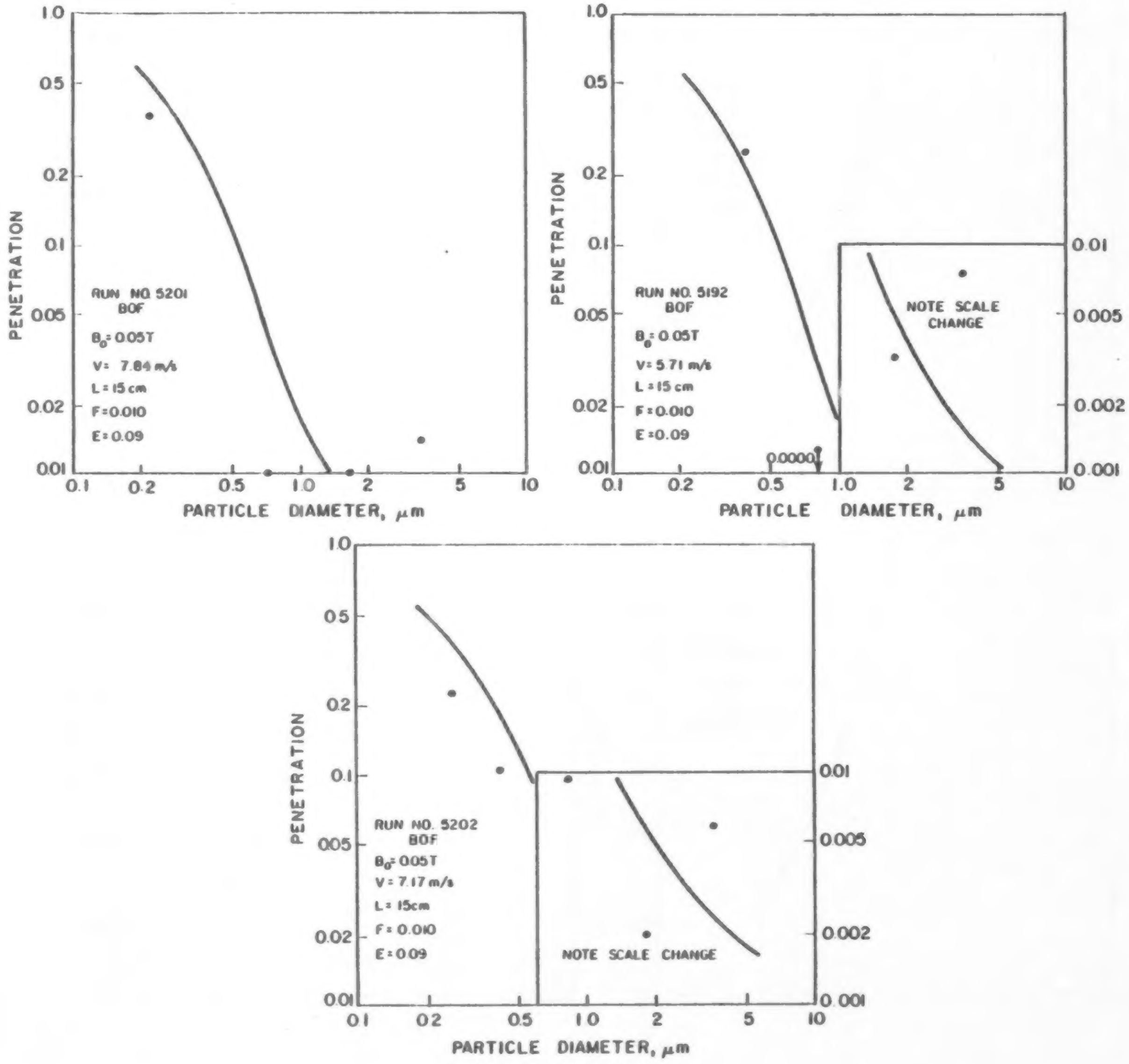

Figure 33. Pilot-scale HGMS results with BOF dust (F=0.010).

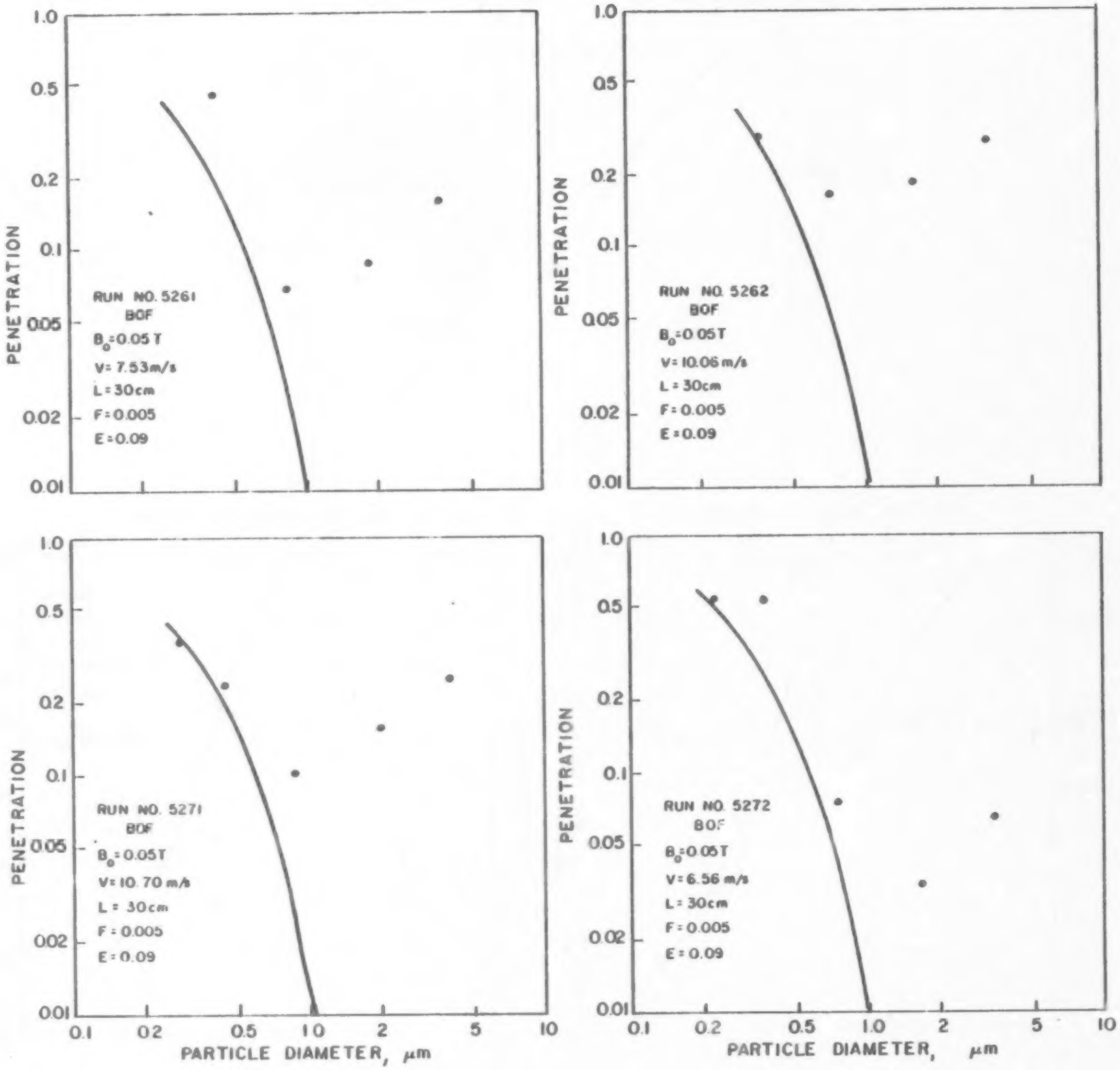

Figure 34. Pilot-scale HGMS results with BOF dust (L=30 cm).

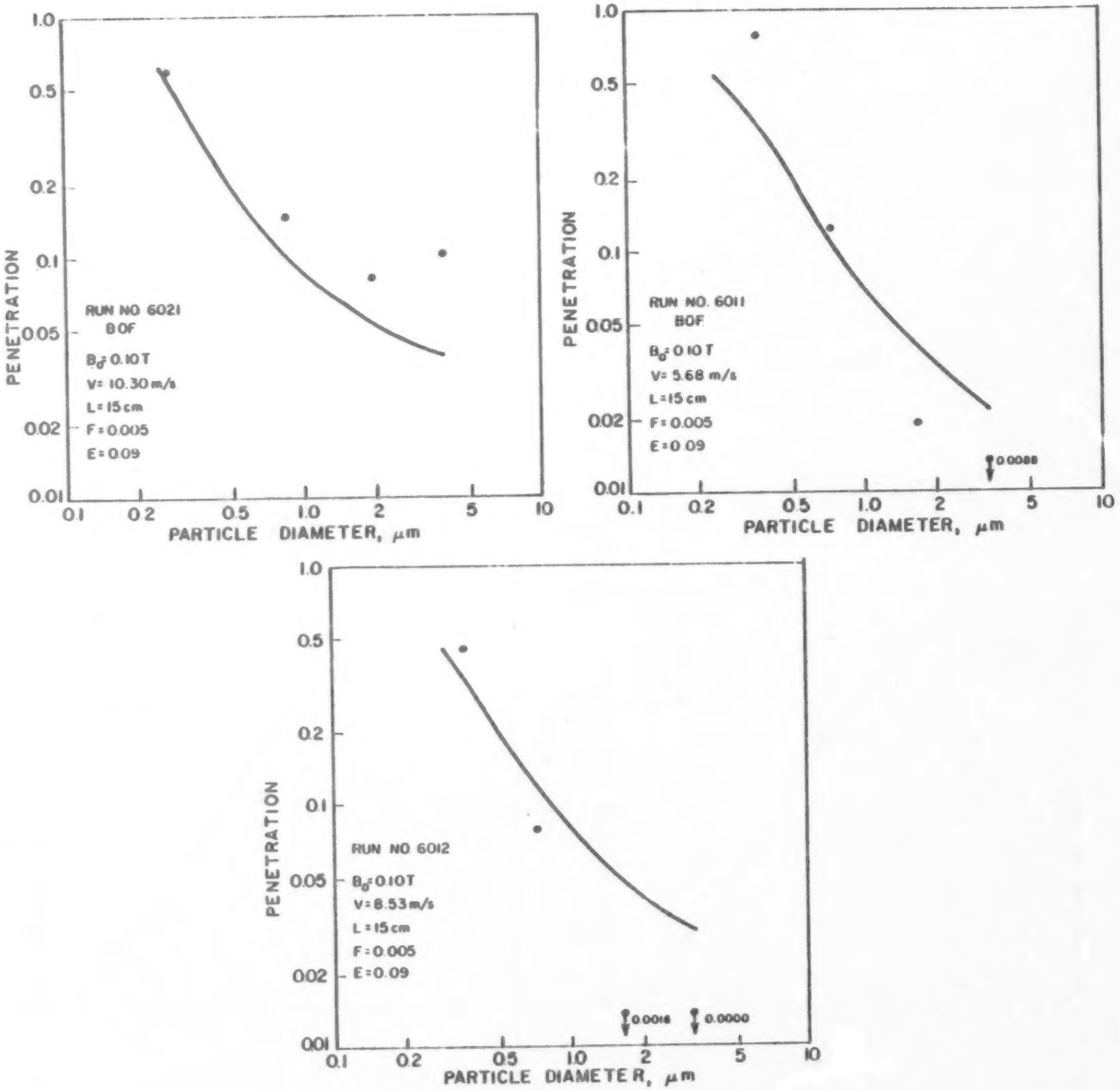

Figure 35. Pilot-scale HGMS results with BOF dust (duplicates of earlier runs).

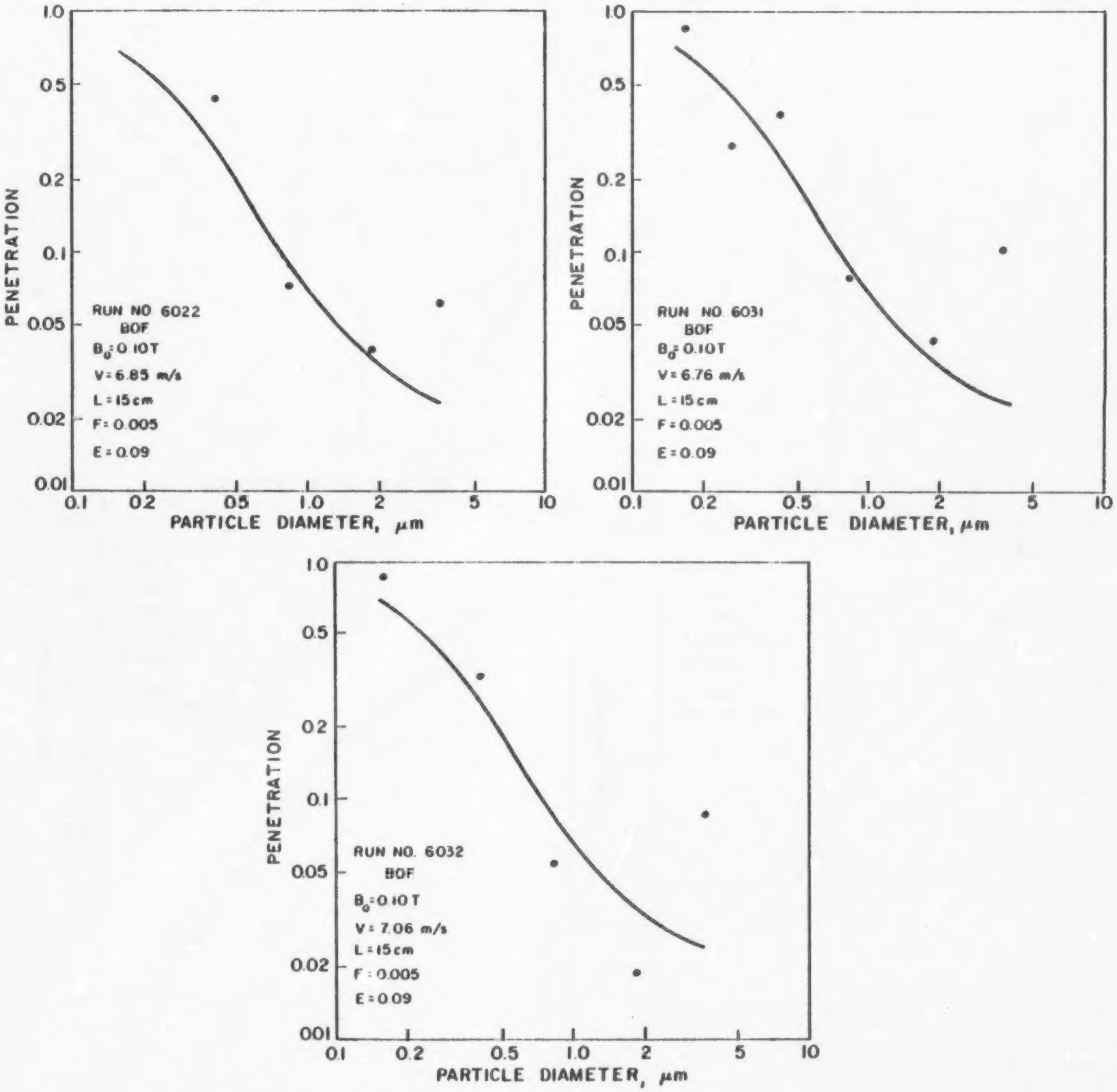

Figure 36. Pilot-scale HGMS results with BOF dust (replicate runs).

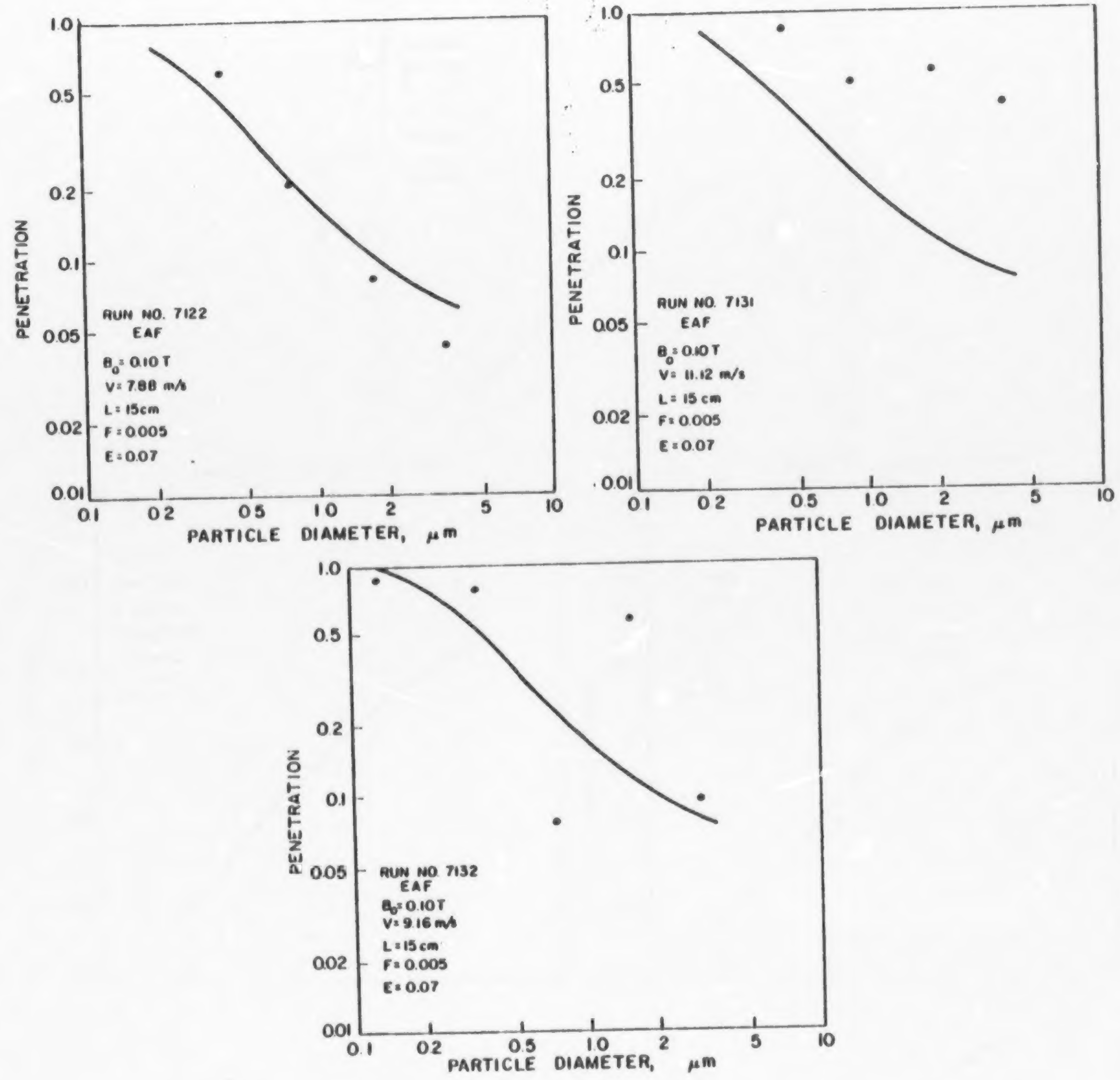

Figure 37. Pilot-scale HGMS results with EAF dust (B_0=0.10T).

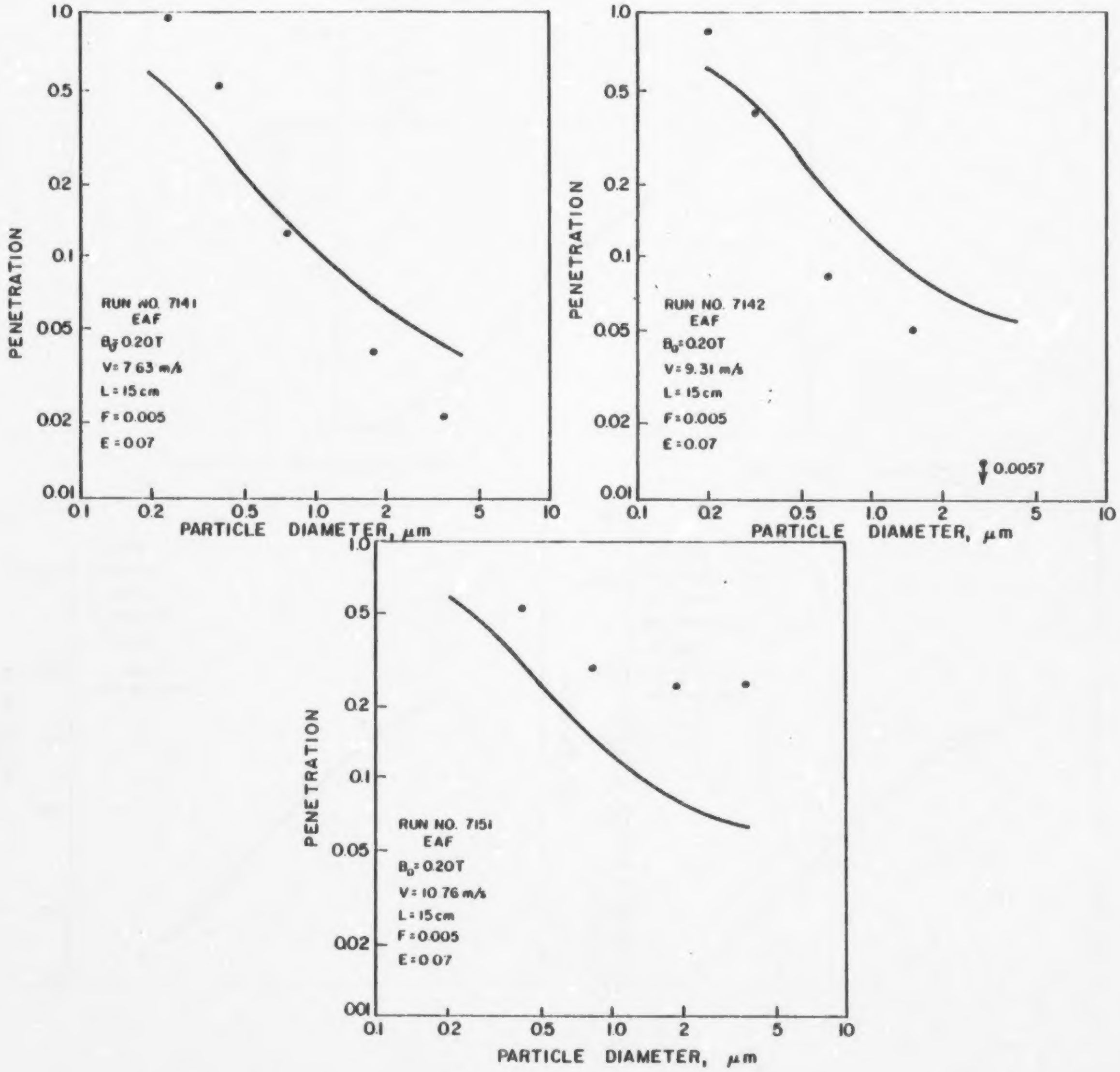

Figure 38. Pilot-scale HGMS results with EAF dust (B_0=0.20T).

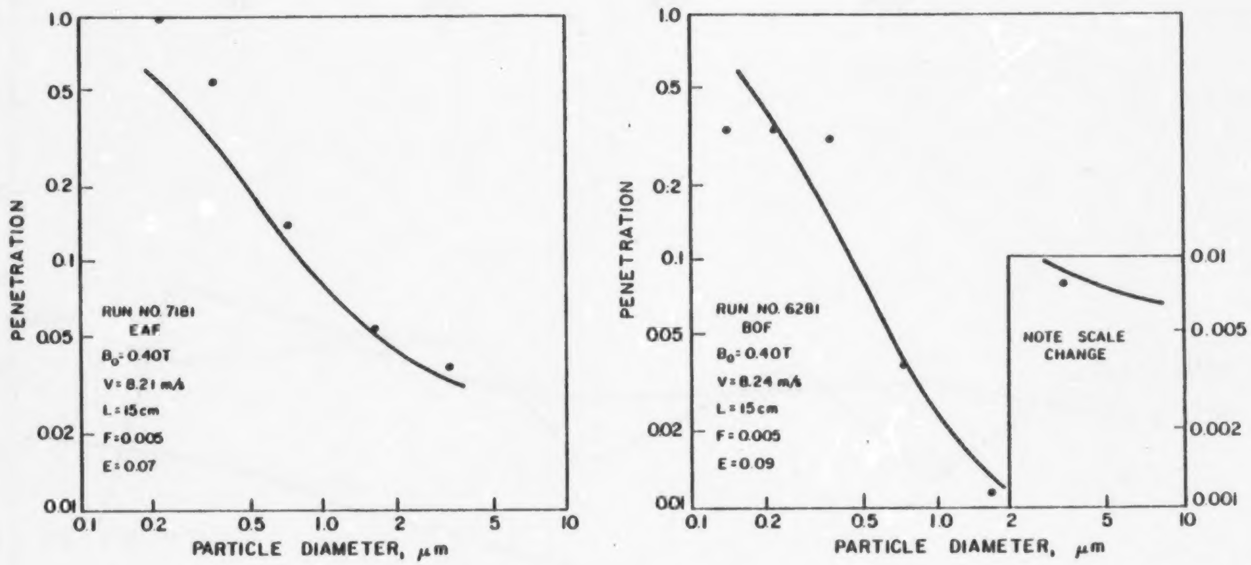

Figure 39. Pilot-scale HGMS results with both dusts at B_0=0.40T.

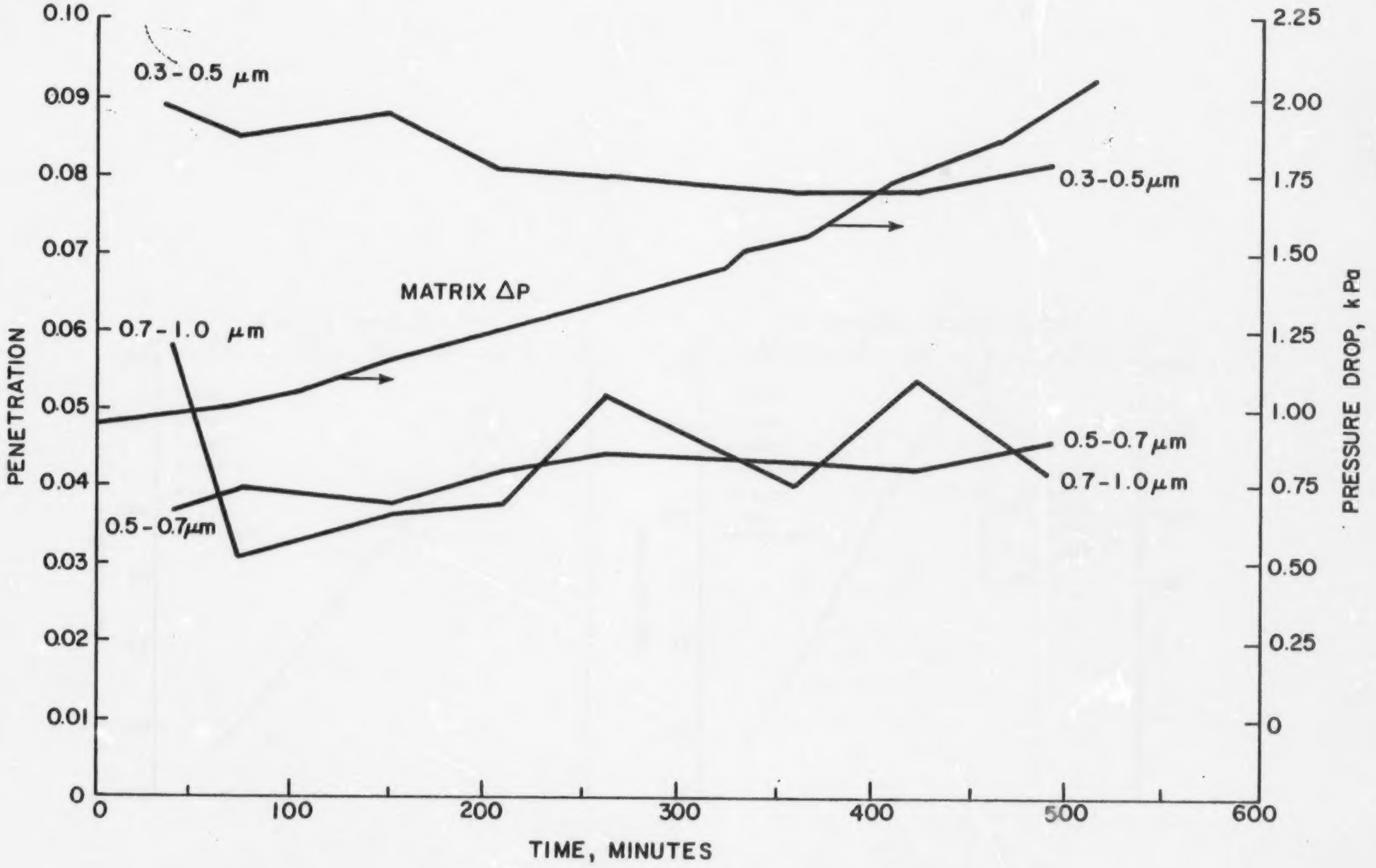

Figure 40. Pilot-scale variation in BOF collection efficiency and matrix pressure drop with matrix loading.

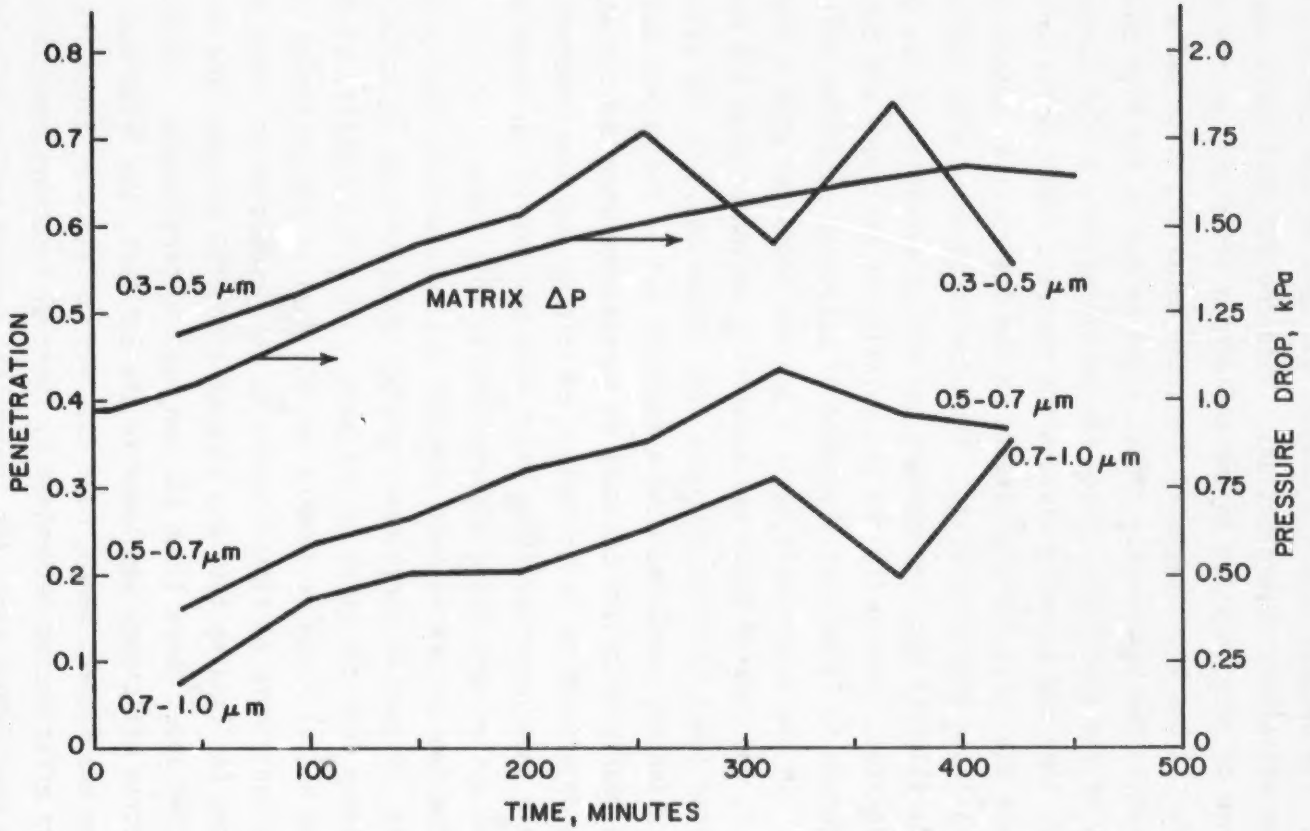

Figure 41. Pilot-scale variation in EAF collection efficiency and matrix pressure drop with matrix loading.

begun with a clean matrix, and operation was continued for several hours. The optical particle counter was used to make periodic collection efficiency determinations. With the BOF dust there was no evidence of deterioration in the collection efficiency as the matrix was loaded. It has been suggested that this behavior, which was also observed in the bench-scale tests, might be due to the high susceptibility of the dust [87]. Since the particles have a high susceptibility, they may actually distort the magnetic field sufficiently to maintain the large field gradients in the interstitial spaces rather than fill the gradient region. Thus the aerodynamic wire radius increases slightly but the magnetic collection mechanism is not grossly deteriorated. Eventually the accumulation of particles and the pressure drop become so large that sloughing of collected particles will probably occur. In the bench-scale test, which was conducted with a field of 0.094 T, the deterioration was apparently beginning when the matrix had collected about half its own mass (see Figure 15). In the pilot-scale test, which was conducted with a field of 0.4 T, the matrix had collected nearly twice its own mass of particulate when the run was stopped, and no deterioration in collection efficiency had been observed. It is possible that large particles which were not within the range of the optical system were being sloughed off at this stage.

The matrix loading test with EAF dust yielded distinctly different results. Figure 41 indicates a gradual deterioration of collection efficiency from the start of the test. The susceptibility of the EAF dust is not as large as that of the BOF dust so the particles apparently do not contribute as significantly to the production of field gradients. When the EAF loading test was stopped after 450 minutes, the matrix had collected about three times its own mass in particulate. (Although the collection efficiency was lower in the EAF test, the inlet mass concentration was higher; hence, more dust was collected.) Since the collection efficiencies determined by inertial impactors represent integrated values over 2-hour runs, the theoretical capture radius calculated for clean fiber conditions is larger than the actual EAF dust capture radius. In the theoretical equation the lower matrix effectiveness factor provides a correction.

It should be noted that nearly all of the data correspond to capture radii that are in the extrapolated portion of Figure 28. Considering that the extrapolations are a possible source of error, the overall fit of the experimental data to the theoretical expression is quite good. There is a fairly consistent trend to overpredict the collection efficiency of the larger particles, particularly in the low-field runs. Assuming that the extrapolated capture radii are not significantly in error, there are at least two possible explanations for this problem. If the collected particles do contribute new regions of high gradient, the gradients are most effective over a dimension approaching the particle size. Considering Oberteuffer's arguments on the relative size of collector and particle [1], this effect is not as strong for larger particles, and they are thus more vulnerable to reentrainment (or failure to be collected) as the matrix becomes loaded. Secondly, the possibility of particles bouncing off the wires or knocking others off has not been included in the model. This phenomenon could possibly be significant with the larger, high momentum particles.

DISCUSSION OF INDIVIDUAL PARAMETER EFFECTS

Analysis of individual parameter effects requires comparison of two or more experimental runs. Many combinations are possible because of the experiment design. In this section representative comparisons are made, and the results are discussed. Before drawing conclusions from these comparisons, it is important to consider the repeatability of experiments conducted under identical conditions. Because of time and cost limitations it was not possible to duplicate all runs. Instead a set of replicates was run at one set of conditions in the central range of the operating parameters. Figure 42 shows the results of these replicate runs. The solid symbols represent the results of three consecutive runs with the same matrix. In each case the field strength was set at 0.1 T. The temperature ranged from 30.3 to 37.2 ° C and

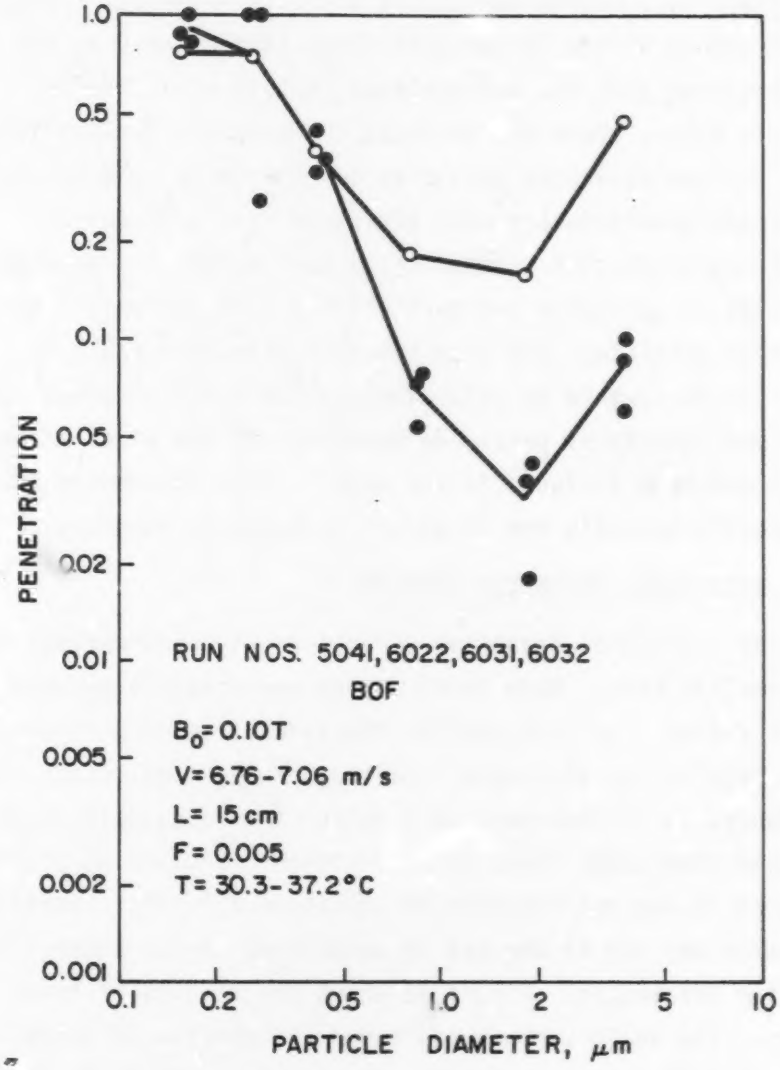

Figure 42. Comparison of collection efficiency results of replicate runs.

the velocity from 6.76 to 7.06 m/s. These ranges indicate the limits of controllability of the two variables. The open symbols are the results of a test run 4 weeks earlier with a different matrix which was supposedly identical. The field strength was also 0.1 T, the temperature was 31.9° C, and the velocity was 6.89 m/s.

Differences in the three runs with the same matrix reflect random error due to variations in dust characteristics, fluctuations in the dust feed rate and size distribution during individual runs, errors associated with the sampling and weighing process, and probably other unknown factors. The additional run with another matrix reflects all of the above sources of error plus the possibility of matrix-to-matrix variation. It is apparent that the matrix variation was significant.

Three other sets of duplicates were run across the same two matrices at three different velocities. Pooled standard deviations for the replicates in Figure 42 plus the three sets of duplicates are reported in Table 8. Dividing the standard deviation by the mean penetration in each case gives the coefficient of variation, a measure of the variability as a fraction of the mean penetration at each diameter. Statistics were not calculated for particle sizes less than 0.4 μm since data in this range could not be obtained during all runs.

TABLE 8. POOLED STATISTICS ON PARTICLE PENETRATION

Nominal Particle Diameter, μm	0.4	0.8	1.8	3.6
Standard Deviation of Penetration	0.100352	0.047474	0.077665	0.169624
Coefficient of Variation	0.229	0.421	0.994	1.055
Degrees of Freedom	5	6	6	5

Figure 43 shows the important practical relationship among matrix pressure drop, matrix length, packing density, and superficial gas velocity. The data were collected at the beginning of the first several runs with each matrix and thus represent clean matrix conditions. The

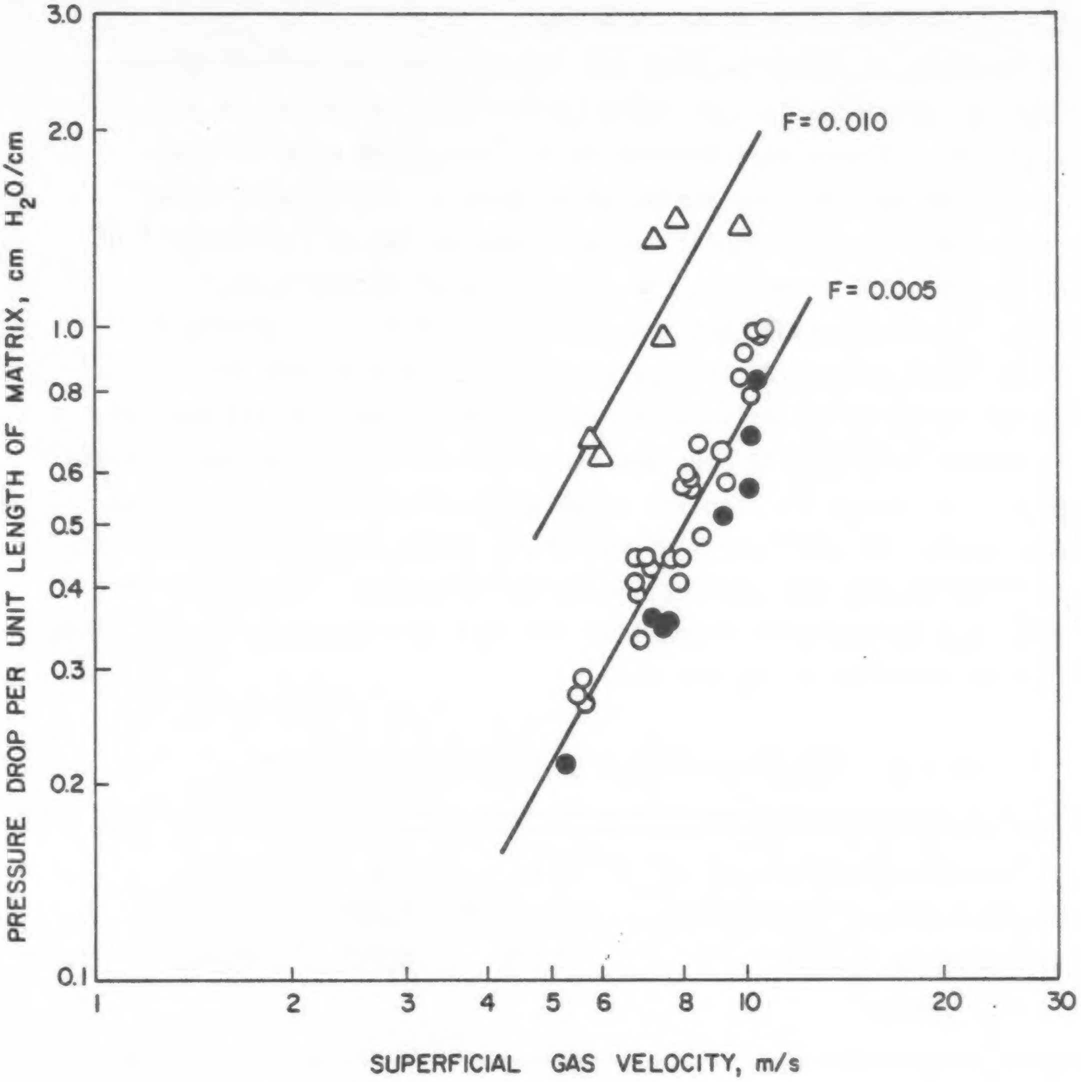

Figure 43. Correlation of matrix pressure drop with gas velocity, matrix packing density and matrix length.

straight lines running through the data were obtained from linear regression of all of the data shown expressed in logarithmic form. The equation is

$$\frac{\Delta P}{L} = 13.07\ F^{1.32}\ V^{1.79} \tag{35}$$

with the pressure drop expressed in cm H_2O, the matrix length in cm, and the velocity in m/s. The pressure drop data also provide an additional indication of matrix variation among runs. Of particular note are the filled circles on the lower line, which are the data for the 30-cm matrix. Assuming that the linear relationship between pressure drop and matrix length is correct, these data suggest that the 30-cm matrix was more porous than the others, possibly due to leakage around the extra cleaning rings or other construction anomalies.

The experimental collection efficiency results support the contention that the construction of the 30-cm matrix might have been faulty. Figure 44 compares the penetration results of the 15-cm and 30-cm matrices at the same velocity for both the no-field and with-field cases. Theoretical arguments suggest that in either case doubling the matrix length should result in the penetration being squared. For example, a penetration of 0.2 would be improved to 0.04. The improvement with the longer matrix is not that dramatic in either case shown in Figure 44. Since there is a question about the effective porosity of the 30-cm matrix, the quantitative effect of matrix length remains uncertain. Increasing the matrix length definitely improves collection efficiency but perhaps not as much as the theory suggests.

Matrix density effects at one velocity are shown in Figure 45, with and without a magnetic field. Again theoretical considerations imply that doubling the matrix density should square the penetration. Analysis of Figure 45 reveals approximately that quantitative result in the no-field case. With the magnetic field applied, the improvement in efficiency achieved by doubling packing density is even greater than predicted. In other comparable runs the improvement in efficiency was at least equal to that predicted.

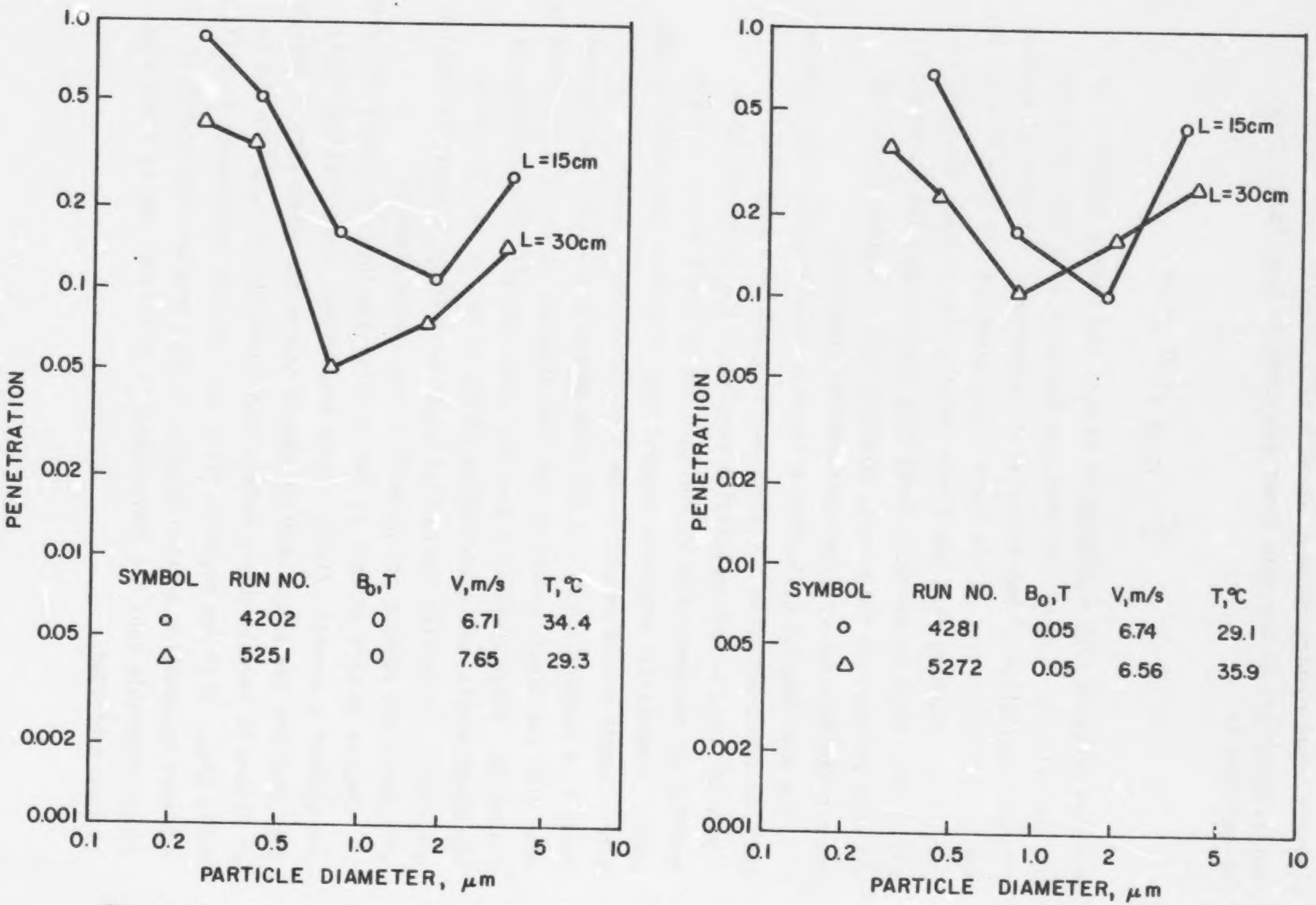

Figure 44. Experimental effect of matrix length on collection efficiency with and without an applied magnetic field.

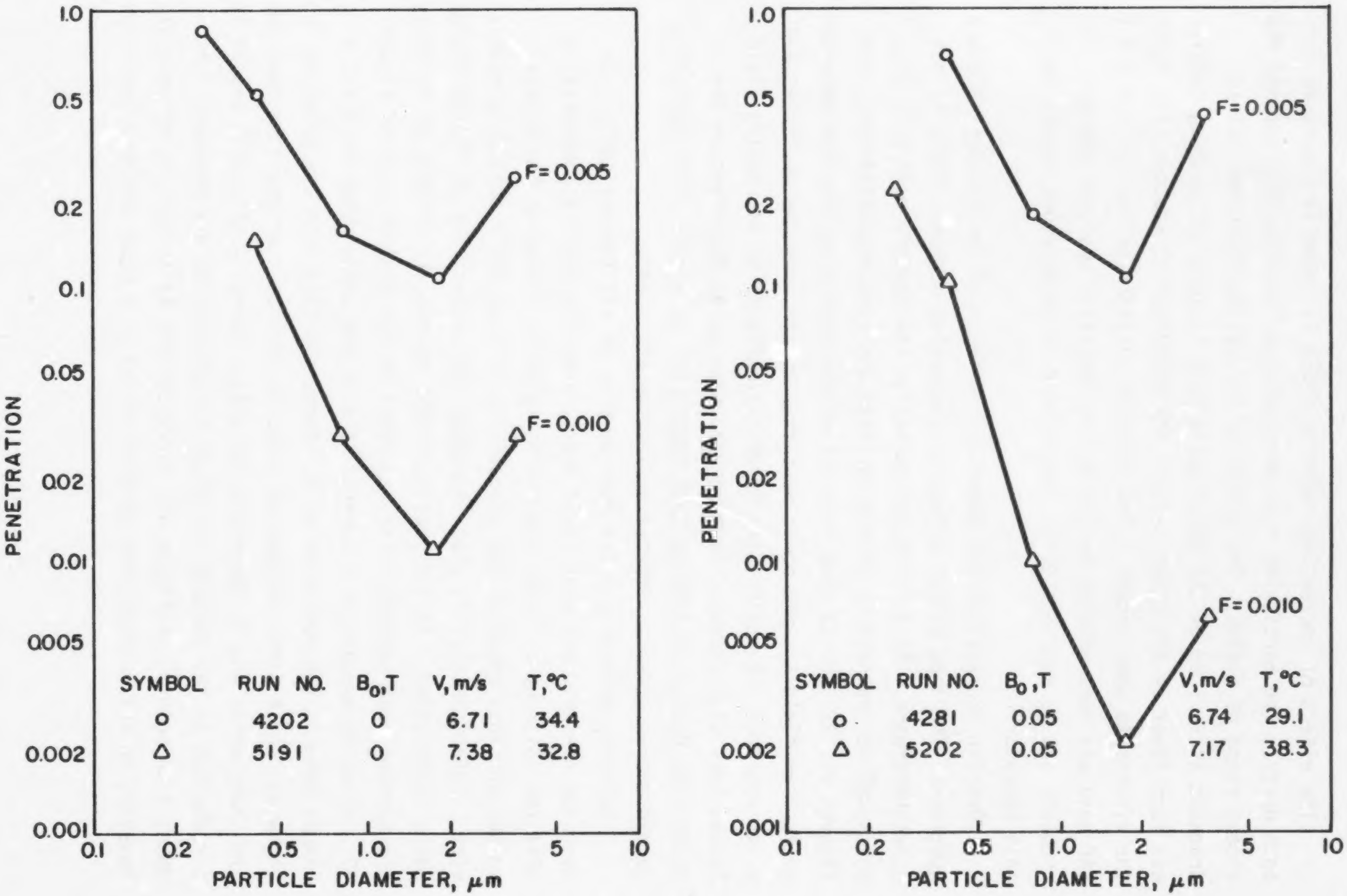

Figure 45. Experimental effect of matrix packing density on collection efficiency with and without an applied magnetic field.

The effect of increasing magnetic field is shown in Figure 46 for both dusts. The particular runs were selected because they spanned the widest range of fields. The effect of increasing field was not as dramatic as in some of the bench-scale runs because the packing density was much lower in the pilot tests. The experimental scatter also masks the effects to some extent. The reversed position of the 0.2 and 0.4 T EAF data was contradicted by the optical particle analyzer and was probably due to sampling error since there is no apparent reason for this behavior.

Despite the scatter the beneficial effects of increasing field are apparent. The theoretical effect of increasing magnetic field is not straightforward. To a first approximation the capture radius is proportional to the product of the particle and wire magnetizations, and Figures 21, 22, and 23 show that all of the magnetizations are dependent on applied field to some power less than 1. As both the particles and wires approach saturation, the beneficial effects of increasing field become less significant. Hence beyond some point dependent on the particular dust, it would be more beneficial to adjust other operating parameters in order to improve collection efficiency.

Velocity effects are the most complex of all theoretically. In both the no-field and with-field cases, velocity has two compensating effects. Without a field, increasing velocity increases the Stokes number and thus enhances the probability of a particle colliding with a wire. Unfortunately, it also increases the probability of the particle being reentrained. In the practical HGMS system the effects of velocity are perhaps best analyzed with reference to the contour plot of Figure 47. Velocity appears as a squared term in the denominator of W and a linear term in the numerator of K. Hence starting from any point on the log W vs. log K plot, increasing velocity implies that one move down two arbitrary units and to the right one unit. Normally this will result in a reduction in the capture radius as illustrated by the movement from point 1 to point 2 on Figure 47, corresponding to a doubling of velocity. However, in the extrapolated portion of the plot when the negative slope

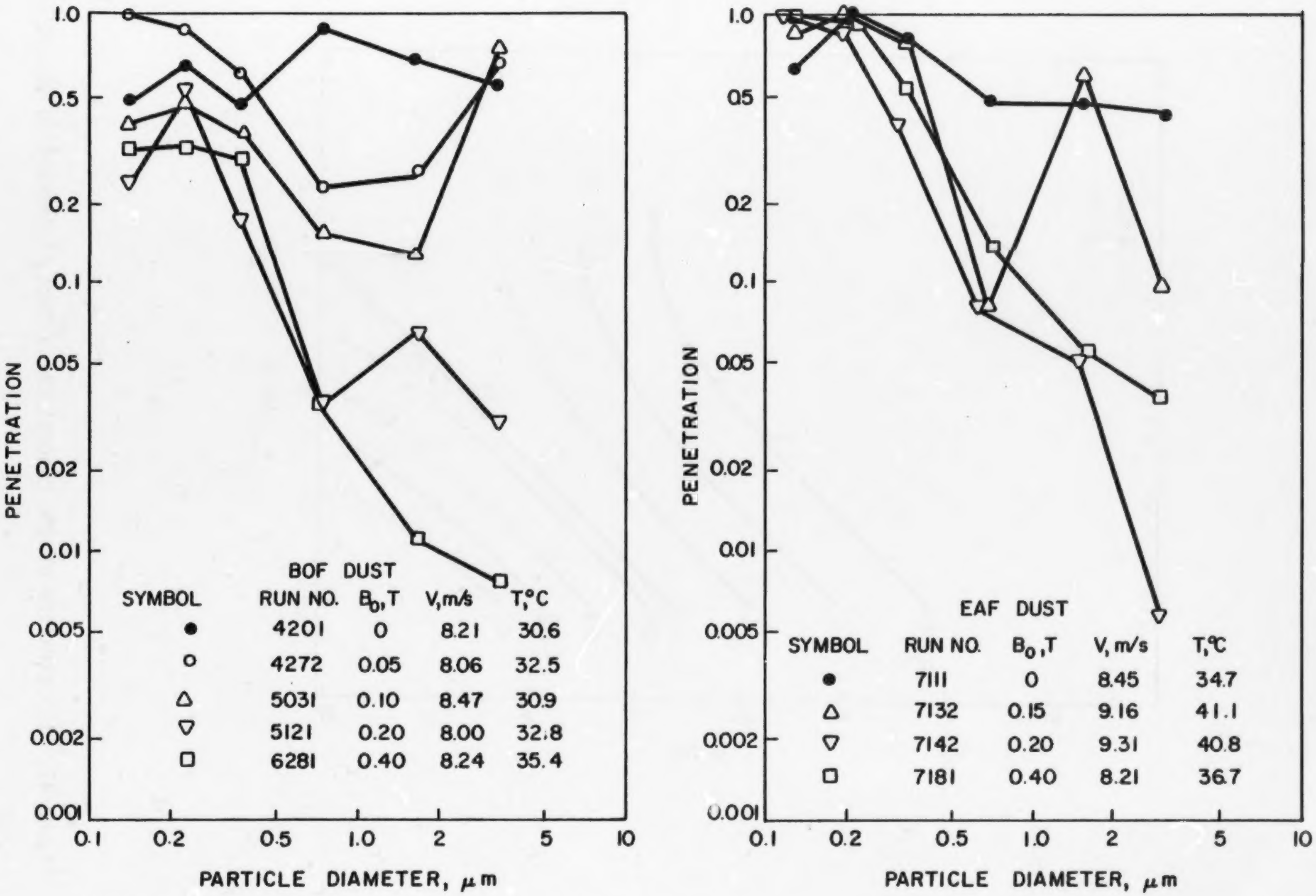

Figure 46. Experimental effect of applied magnetic field on the collection efficiency of both dusts.

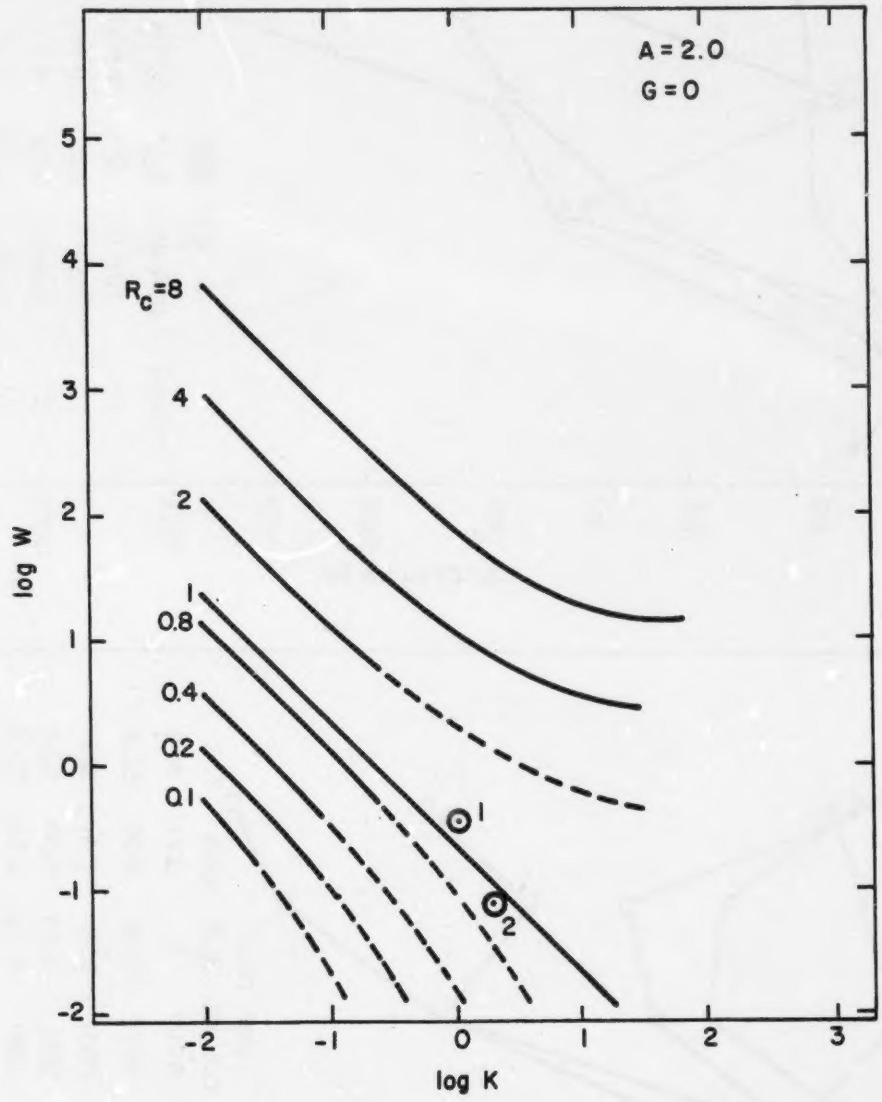

Figure 47. Illustration of the theoretical effect of increasing gas velocity.

of the low capture radius contours becomes larger in magnitude than 2, increasing velocity actually results in an increase in capture radius. Physically this is due to beneficial inertial effects of particles approaching in the projected area of the fiber.

Figure 48 illustrates the experimental effects of velocity. These plots are not typical in the strict sense of the word because a few results showed contradictory effects. In general, however, increasing velocity has no strong effect on the smaller particles, which correspond to the extrapolated portion of Figure 47. Higher velocities tend to be detrimental to larger particle collection when the capture radius is greater than 1. The same behavior is true with no field apparently due to the greater tendency of larger particles to be reentrained.

Three of the four elevated temperature runs indicated the possibility of a beneficial temperature effect especially with the larger particles. The fourth comparison at the highest velocity showed no significant effect. The theoretical arguments predict a very small decrease in collection efficiency when the temperature is raised from 30° C to 110° C. The collection matrix was particularly difficult to clean after the four higher temperature runs, suggesting that for some reason the particles adhered more strongly to the matrix. Industrial gas cleaning applications of HGMS would be more economically attractive if the process could be operated at temperatures well above the 110° C used in these experiments. If the observed improvement in efficiency can be shown to be real in more extensive testing, it will be an important result. However, the observed difficulty in matrix cleaning would have negative implications.

OPERATING DIFFICULTIES

Operating problems were encountered in three separate areas of the total pilot-plant system. The first two were associated with the dust generation and wind tunnel system. While these problems have no direct implication toward application of the HGMS process, they do represent limitations on future pilot-plant work that could be significant. The third difficulty was associated with the HGMS matrix cleaning system and suggests the need for considerably more developmental work in this area.

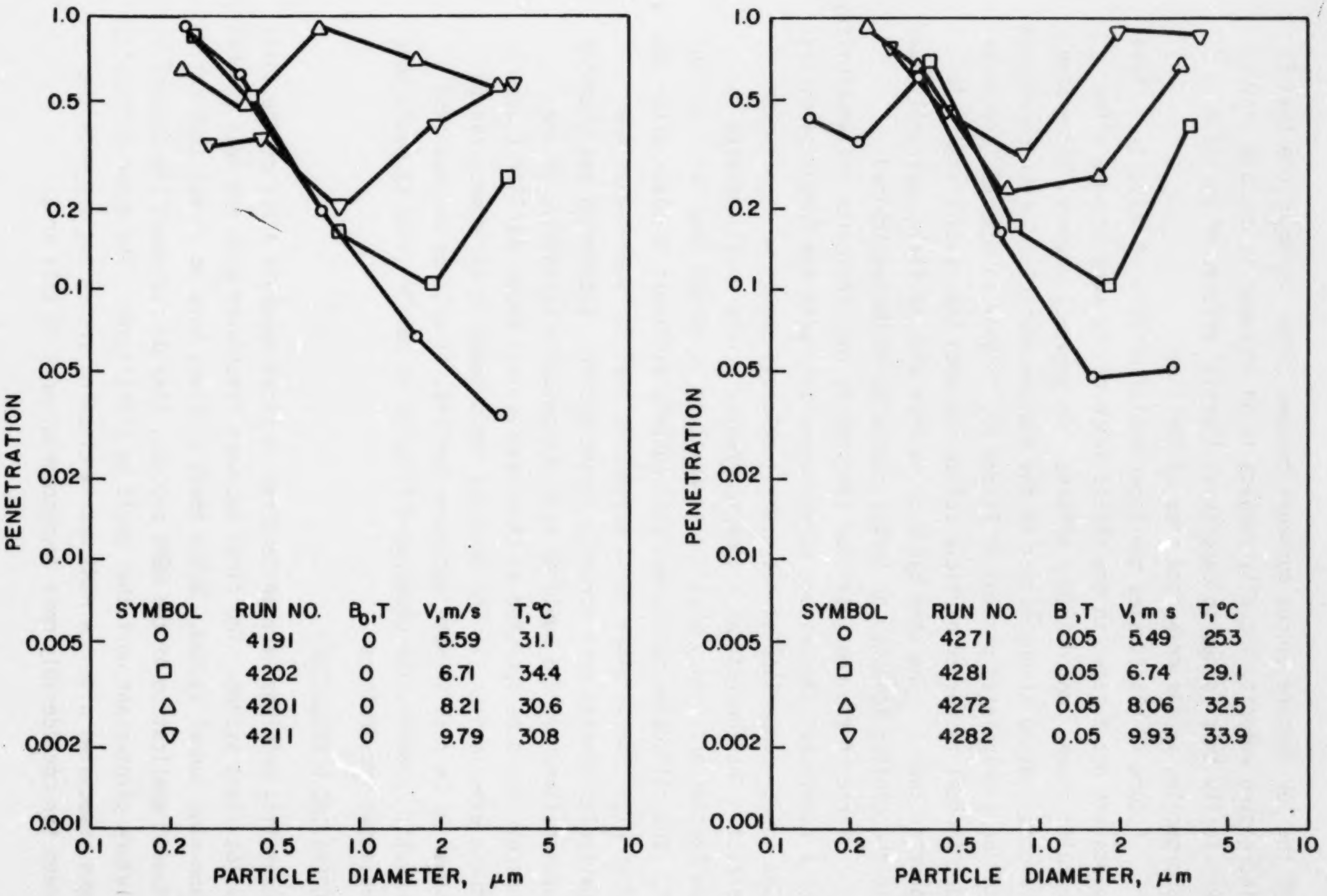

Figure 48. Experimental effects of gas velocity on collection efficiency with and without an applied magnetic field.

The capabilities of the fluidized bed dust generation system have been studied in some detail using fly ash as the test dust [82]. With the iron oxide dusts used in these tests, however, several new difficulties were encountered. First, dust feed rates were limited to about 2 kg/hr. Higher feed rates were attempted so that higher dust concentrations could be studied, but the dust would accumulate on the lower bed and eventually force shutdown. The percentage of submicron particles in the system output was also much lower than desired. Several different combinations of fluidizing media and fluidizing gas flow rate were tried with little improvement. Workable conditions were finally achieved by keeping the feed rate as high as possible without causing plugging, reducing the wind tunnel dilution air flow to as low a level as possible, and using the slipstream cyclone to remove large agglomerates ahead of the HGMS canister. With the present facilities the system cannot be used to study the collection of higher concentrations of submicron particles that would be more typical of industrial conditions.

The second problem area involved the higher temperature work. As the wind tunnel is presently constructed, steam can be added to the air to raise the humidity, but there is no means of determining how much steam is being added or what the absolute humidity is when the gas temperature is greater than 50° C. The humidity can be determined with a sample train, but it cannot be set at a desired point before the run is made. In this experimental work the humidity was allowed to fluctuate with the ambient conditions during the lower temperature work, and small amounts of steam were added in the higher temperature runs so that the humidity would not be extremely low. Better control of the steam addition and real-time monitoring of the air humidity will be needed before the system can be used to simulate industrial gas streams at an elevated temperature and a realistic percentage of water vapor.

Since the bench-scale HGMS matrices were cleaned by manual rapping, the quantitative requirements of matrix cleaning were not well defined when the pilot unit was designed and constructed. As a result, the vibrator and air blowing system installed proved inadequate. Transmission of vibrational energy from the externally mounted vibrator to the matrix was poor, and the air blowing system was not sufficient to completely overcome the residual magnetism holding the particles to the matrix wires. These same concepts can probably be applied successfully however, with the experience gained from the pilot-plant operation and the quantitative background provided by the reentrainment modeling studies.

The complex relationship involving matrix length, packing density, particle susceptibility, particle size, and particle mass concentration needs considerably more attention. Matrix cleaning is obviously more difficult with higher packing densities or longer matrices. Higher particle concentrations will require more frequent cleaning, and the difficulty of cleaning is most probably related to particle size and susceptibility. If parallel, cyclical systems are to be applied to fine particle control, all of these factors will have a strong effect on the duty cycle of the individual magnets and the design of the auxiliary cleaning apparatus. The economic viability of the process could well hinge on the successful demonstration of either a cyclical system with reasonable duty cycles and simple mechanical construction, or preferably a continuously operating system based on the carousel principle described in Section 4 or some other innovative design.

SECTION 7

ECONOMIC COMPARISON OF HGMS AND CONVENTIONAL CONTROL TECHNOLOGY

BASIS OF ECONOMIC COMPARISON

To compare the capital cost and power requirements of alternate methods of fine particle control, one must insure that the estimates are based on equipment that will achieve comparable results in a specific application. The design of particulate control equipment is usually highly specific to the particular application. For example, the design parameters of an electrostatic precipitator (ESP) for a coal-fired boiler might be quite different from those for a basic oxygen furnace because of differences in particulate and gas stream characteristics. HGMS performance data are currently available only for the collection of particulate that originated in basic oxygen and electric arc steel-making furnaces. Estimates of capital cost and energy requirements derived from these data should therefore be compared only to estimates for conventional technology applied to BOF's or EAF's. Even for a singular type of application, differences will certainly exist in the actual cost and energy requirements of equipment designed for specific furnaces. The estimates presented in this report are therefore intended to serve as an approximate economic comparison of HGMS with conventional control technology applied only to steel-making furnaces.

The preliminary nature of this analysis combined with the uncertainty that would have been introduced by comparing different existing industrial applications (many of which are retrofits) ruled out an inquiry to the iron and steel industry to determine actual cost and energy requirements of existing BOF and EAF particulate control equipment. Instead the analysis was based on a study conducted by the

Industrial Gas Cleaning Institute, (IGCI) for EPA in 1971 [88]. The published report of this study contains actual vendor quotations for high-efficiency electrostatic precipitators and venturi scrubbers designed to control particulate emissions from a typical basic oxygen furnace. At the time the study was conducted there were no baghouses in use on BOF's in the United States. Electric arc furnaces were not specifically addressed in the IGCI report. Although the particulate matter emitted from the two types of furnaces is similar, the cost and energy requirements for comparable control efficiencies could be somewhat different.

The IGCI study reports flange-to-flange control device costs, total installed capital costs, and operating costs in 1971 dollars. Since information on HGMS auxiliary equipment (ducts, dampers, collected dust handling equipment, etc.) and installation costs are not yet established for particulate control applications, the comparison presented here is limited to flange-to-flange device costs and operating power requirements. Also since HGMS collection of airborne particulate has been demonstrated only on bench-scale and pilot-scale equipment, the scale-up factor is very large. The full-scale HGMS estimates were based on modules consisting of commercially available magnets (complete with power supplies and cooling equipment) arranged in a multi-path parallel flow configuration for cyclical operation. A 70-percent duty cycle was assumed. A continuously operating system might offer better utilization of magnetized volume and hence lower capital costs, but the application of continuous units to gas streams has not yet been demonstrated.

All equipment costs reported here have been escalated from their original reported date of applicability to mid-1977 using the Marshall and Swift equipment cost index [89].

COST AND ENERGY ESTIMATES FOR CONVENTIONAL TECHNOLOGY

The IGCI study considered several alternative designs. Electrostatic precipitators are installed only in open-hood BOF systems to avoid explosion hazards. Wet scrubbers and, presumably, high gradient magnetic separators can function safely and effectively in either open-hood or closed-hood systems. To allow better comparison, the ESP and venturi scrubber with the most nearly comparable design features (open-hood system, largest gas flows, equal collection efficiencies) were selected. A summary of the ESP and scrubber designs is presented in Table 9. The 99.9 percent collection efficiency specified by the IGCI is a very stringent requirement which in most cases will exceed the EPA new source performance standards for basic oxygen furnaces [90]. The designs reported by the IGCI may be optimistic in that higher pressure drop requirements have been reported for wet scrubbers operating at equivalent or lower collection efficiencies [91,92].

COST AND ENERGY ESTIMATES FOR HGMS

The mathematical model that was used to analyze the pilot-scale HGMS experimental results also provides a quantitative approach to the optimization of process operating conditions for a particular application. The process cannot be completely optimized, however, until additional information is developed on alternative magnet designs oriented directly to gas-stream application and until a wider experimental data base is obtained to further verify the model. The HGMS units presently in service in the clay industry are basically of a singular design: 2.13-m diameter iron-bound solenoids that require 400-500 kW to produce applied fields on the order of 2 T over a pole gap compatible with a 50-cm matrix. For fine particle collection in gas streams, much lower fields may be sufficient, and the approach to cost-optimized design could be significantly different. Also, because of the large quantities of gas that must be cleaned, matrix pressure drop is a more critical parameter that could also affect magnet design and matrix configuration.

To conduct this analysis cost estimates were obtained from a commercial vendor [93] for large iron-bound solenoids of the conventional design with modifications that would make them more compatible with large gas flows and with the operating conditions proven effective in the pilot-scale tests. The estimates are summarized in Table 10. Power requirements

TABLE 9. DESIGN AND COST SUMMARY OF CONVENTIONAL BOF CONTROL EQUIPMENT

Control Device	Electrostatic Precipitator		Wet Scrubber	
System of Units	SI	English	SI	English
Process Gas Flow	481 m^3/s(1)	1,020,000 ACFM(1)	309 m^3/s(2)	655,000 ACFM(2)
Outlet Particulate Loading	0.011 g/m^3(1)	0.0046 gr/ACF(1)	0.016 g/m^3(2)	0.0072 gr/ACF(2)
Total Mass Collection Efficiency	99.9%	99.9%	99.9%	99.9%
Pressure Drop	- -	- -	10.5 kPa(3)	42 in. H_2O(3)
Total Power Requirement	1525 kW(4)	2045 hp(4)	5605 kW(5)	7518 hp(5)
Flange-to-Flange Cost (1977 $)	$1,944,000		$640,000	

(1) At precipitator outlet: 343° C (650° F), -1.5 kPa (-6 in. H_2O) gauge, 11 percent water by volume.

(2) At scrubber outlet: 82° C (180° F), -11.2 kPa (-45 in. H_2O) gauge, 57.4 percent water by volume.

(3) Across scrubber and mist eliminator.

(4) Report does not state explicitly what this includes. It definitely includes precipitator energization and pressure drop, but may also include some duct pressure drop.

(5) Report does not state explicitly what this includes. It definitely includes liquid pumping and scrubber pressure drop, but may also include some duct pressure drop.

TABLE 10. COST ESTIMATES FOR LARGE IRON-BOUND SOLENOIDS APPLICABLE TO FINE PARTICLE CONTROL

Matrix Diameter	3.15 m	3.15 m
Matrix Length	15 cm	30 cm
Field Capability	0.4 T	0.4T
Cost, (1977)	$320,000	$370,000

of these units were scaled from existing data on 2.13-m diameter by 50-cm matrix length units. Several factors can influence magnet power requirements, but with similarly designed solenoids to a good approximation the power requirement for a given field is directly proportional to the diameter and to the length of the cylindrical magnetized volume. Reported data for the 2.13-m units and estimates for the two larger units are shown in Figure 49. References for the data are indicated on the figure.

The operating temperature and gas volume of the IGCI electrostatic precipitator were taken as operating conditions for the HGMS. Theoretically higher temperatures will have an adverse effect on HGMS performance by increasing gas viscosity and decreasing particle magnetic susceptibility. A correction was made for the viscosity difference but the temperature dependence of particle susceptibility has not yet been determined. The design was also based on basic oxygen furnace dust since that was the basis of the IGCI designs. The electric arc furnace dust used in the pilot-scale tests would require a more expensive design in terms of capital investment and/or power requirements because of the lower magnetic susceptibility of the dust. This does not necessarily mean that all electric arc furnaces would be more expensive to control or that the design developed here would be appropriate for all BOFs. Since the composition of the dust varies from furnace to furnace, the magnetic susceptibility most probably does also.

Since the IGCI designs stipulated 99.9 percent collection efficiency without stating the particle size distribution, the HGMS design was

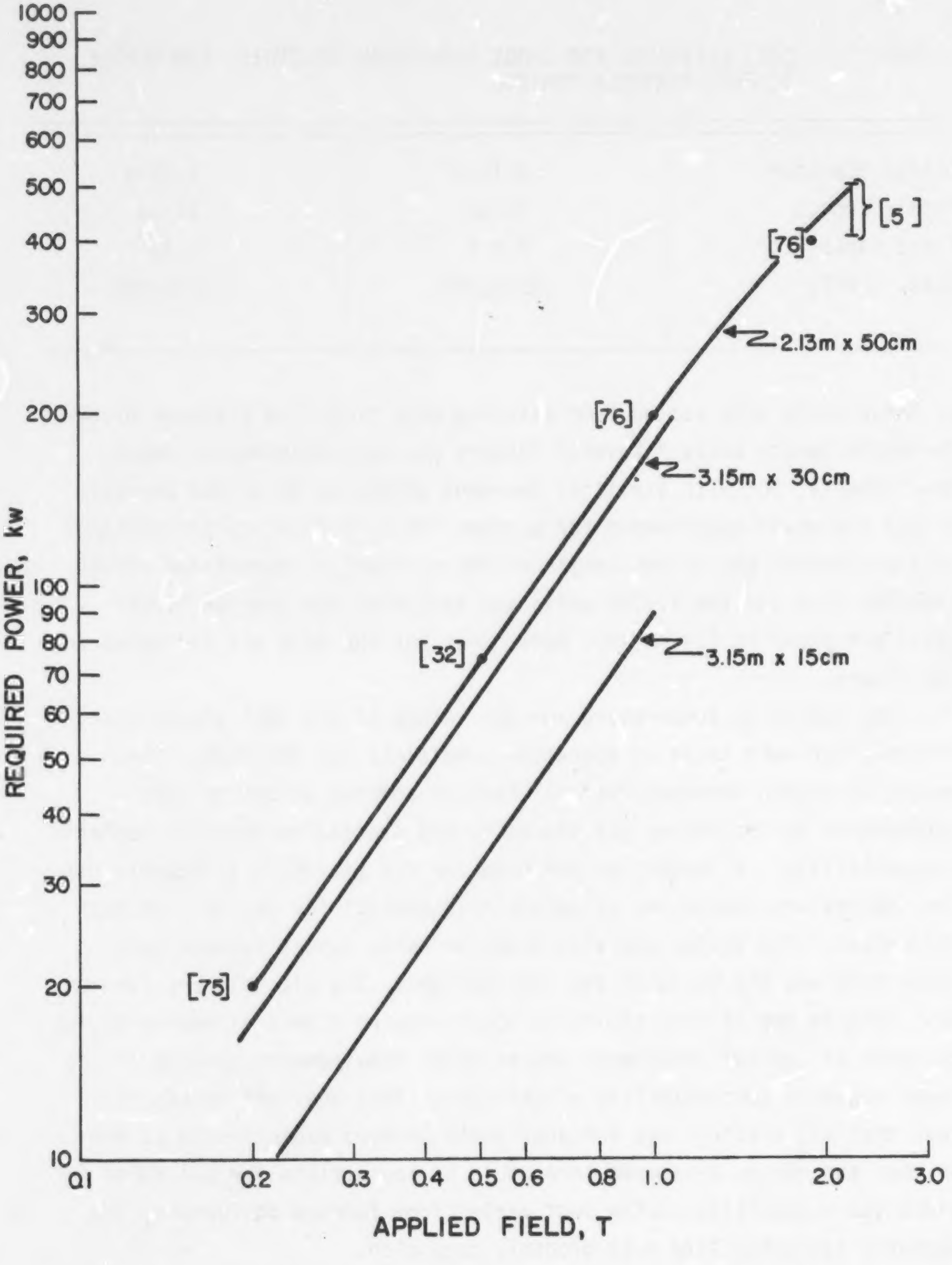

Figure 49. Reported and estimated power requirements for iron-bound solenoids of various configuration.

based on a reasonably comparable specification of 99.9 percent collection of 1.0 μm BOF particles. The procedure for estimating flange-to-flange costs and power requirements is outlined below.

(1) Basis: 99.9 percent collection of 1.0 μm particles

(2) Design equation:

$$P = \exp\left[-\frac{EFLR_c}{a(1-F)}\right] \tag{34}$$

(3) Determination of operating parameters: Seven of the 3.15-m diameter units will handle the 481 m^3/s gas flow with a superficial gas velocity of 8.8 m/s. With BOF dust and the same matrix material used in the pilot-scale experiments, $E = 0.09$ and $a = 25$ μm. For either $F = 0.005$, $L = 30$ cm or $F = 0.010$, $L = 15$ cm, the field requirement is determined as follows.

particle diameter	1.0 μm
required collection efficiency	99.9%
from Equation (34), R_c =	1.27
from Equation (18), K =	2.94
log K =	0.47
from Figure 50, log W =	-0.64
W =	0.229
from Equation (16), H_o =	3.5×10^5 A/m
B_o =	0.44 T

For additional reference, with these operating parameters the calculated collection efficiency of 0.5 μm particles is 98.7 percent.

(4) Calculation of power requirements:

(a) With a shorter, more dense matrix ($L = 15$ cm, $F = 0.010$): From Figure 49 power per magnet is 27.5 kW for a total magnet power requirement of 192 kW. From Equation (35)

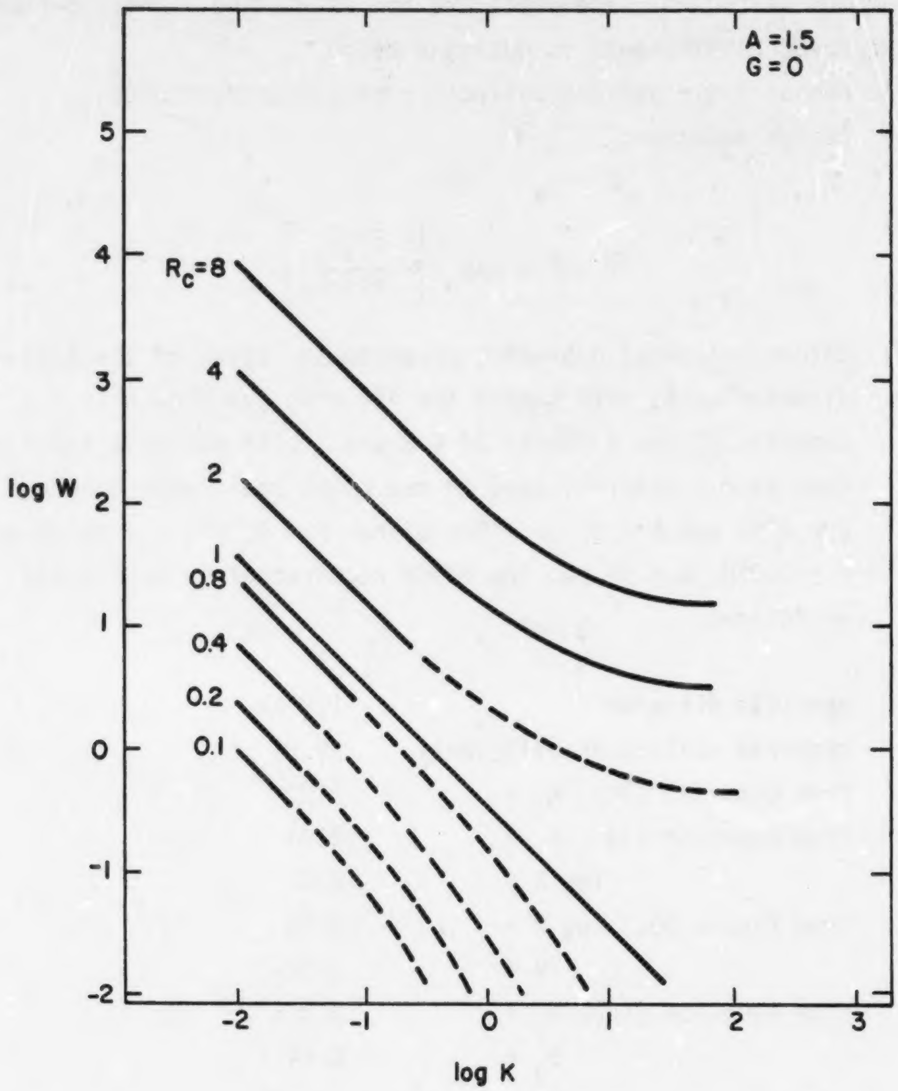

Figure 50. Lines of constant capture radius with inertial forces included and A=1.5.

corrected for lower gas density at 343° C, matrix pressure drop is 1.1 kPa (4.4 in. H_2O). With 60 percent fan efficiency, fan power is 885 kW. Total power requirement is thus 1077 kW.

(b) With a longer, less dense matrix (L = 30 cm, F = 0.005): From Figure 49 power per magnet is 55 kW for a total magnet power requirement of 385 kW. From Equation (35) corrected for lower gas density at 343° C matrix pressure drop is 0.9 kPa (3.5 in. H_2O). With 60 percent efficiency, fan power in 702 kW. Total power requirement is thus 1087 kW.

(5) Calculation of capital cost: Since the power requirements of the two alternatives considered are virtually identical, the shorter, more dense matrix is clearly superior because of the lower cost of the magnets. With a 70 percent duty cycle, a total of ten magnets would be required for a total flange-to-flange cost of $3,200,000.

COMPARISON OF HGMS AND CONVENTIONAL TECHNOLOGY

The estimated cost and energy requirements of the HGMS device are compared with conventional technology in Table 11. Since the assumed gas temperature, pressure, and water content were not the same in the wet scrubber as in the electrostatic precipitator and HGMS, normalization of costs and energy requirements by the actual gas flow in each device does not provide a direct comparison. To refer the estimates to an equivalent application the scrubber gas volume was corrected to the operating gas conditions of the precipitator and HGMS.

Table 11 indicates that on a flange-to-flange basis the scrubber has the lowest capital cost. This may be misleading, however, since the scrubber would require an associated water treatment system not required by either the precipitator or HGMS. With the design utilized for these estimates the capital cost of the HGMS is somewhat higher than the precipitator but still well within the economic ballpark considering the accuracy of the estimates. The estimates of power requirement show that the scrubber requires several times more energy than either the precipitator or the HGMS to do a comparable job. The HGMS is estimated to

TABLE 11. COMPARISON OF HGMS AND CONVENTIONAL TECHNOLOGY

Device	ESP	Scrubber	HGMS
Collection Efficiency, %	99.9	99.9	99.9
Flange-to-Flange Cost, $\$/m^3/s$	4042	2762	6653
$/CFM	1.91	1.30	3.14
Power Requirement, $kW/m^3/s$	3.2	24.2	2.2
hp/1000 CFM	2.0	15.3	1.4

All estimates are referred to clean gas at 343° C (650° F), -1.5 kPa (-6 in. H_2O) gauge, 11 percent water by volume.

be more efficient than the precipitator in terms of energy utilization. Again, however, the accuracy of the estimates must be considered. Also the precipitator estimate may include some unintended contribution for duct pressure drop.

Several general conclusions about optimization of the HGMS process can be drawn from the above results. First, it would appear that matrix length should be kept short at the expense of other variables to achieve the most cost effective designs. The limiting factors of this situation might be good flow distribution and homogeneity of the applied magnetic field, both of which become more difficult to achieve as the aspect ratio of the matrix increases.

The relative importance of capital and operating costs can vary with individual applications according to the company's amoritization methods, tax situation and so forth. Compared to the precipitator system, however, the HGMS estimates of Table 11 imply a need to lower capital costs perhaps at the expense of power requirement if necessary. One way to accomplish this reduction would be to increase the superficial gas velocity and thus reduce the required number of magnets. Since the fan power requirement is already considerably higher than the magnet power requirement, this increase in velocity might be accompanied by a reduction in matrix packing density to lower pressure drop and an increase in the applied field of each magnet to maintain the high collection efficiency. Another approach would be to cool the gas further before cleaning it. The volume of gas cleaned could be reduced allowing a smaller number of magnets to handle the flow. This savings would of course be at least partially offset by the investment required to accomplish the additional gas cooling.

While these adjustments could in principle lead to a more optimum design, they also point to a potential problem. The loading time of the collection matrix (time between cleanings) is apparently directly proportional to the mass of the matrix and inversely proportional to the gas velocity and to the particulate concentration. Other factors such as applied field and particle susceptibility may also be important. With a matrix density of 0.010, a matrix length of 15 cm, and a superficial velocity of 8.8 m/s (the design used to obtain the economic estimates above), a matrix cleaning a dirty gas concentration of 10 g/m^3 (4.4 gr/ft^3) would collect its own mass of dust in 2.2 minutes. By the time the matrix collected its own mass, increased pressure drop or decreased collection efficiency would probably dictate that the matrix be cleaned. To achieve a 70 percent duty cycle would then require that the matrix be cleaned and returned to service in slightly under 1 minute. In batchwise operation the gas flow and magnetic field would be temporarily shut off to allow in-situ matrix cleaning. The large iron-bound solenoids in commercial use are reported to have a field decay time on the order of 60-90 seconds although technology has now been developed that accelerates this decay time to 5 to 10 seconds [5]. Damper systems to accomplish the necessary flow switching in this relatively short time frame could be relatively costly and subject to maintenance problems. The indicated optimization technique of increasing gas velocity and decreasing matrix density would shorten the loading time and the cleaning time required to maintain a 70 percent duty cycle. The reduction of gas temperature would also shorten the loading and required cleaning times by creating a more concentrated dust stream.

This analysis points to the need of additional developmental work in the design of magnets, matrices, and cleaning systems specifically geared to application in high velocity gas streams with moderate and high dust concentrations. The short estimated cycle times provide a strong incentive to develop continuously operating rather than cyclic systems.

The comparison of alternate BOF emission control methods suggests that HGMS is a viable alternative for fine particle control in systems where the particulate has a relatively high magnetic susceptibility. In addition to reasonable projected capital cost and energy requirements the process offers other potential advantages over conventional technology. The high throughput suggests smaller space requirements than electrostatic precipitators or baghouses. This could be important in any application but especially perhaps in a retrofit situation. Stainless steel wool is a common, relatively inexpensive material which is resistant to high temperature and corrosive environments. The lack of any sparking mechanism should make the process amenable to dry, combustible environments with proper design precautions. Unlike many wet scrubber systems the HGMS process would not turn an air pollution problem into a water pollution problem. Even if water should be employed to assist in matrix cleaning the quantity would be much less than in scrubber systems.

These attractive features of the HGMS process strongly support an argument for the continued development of the technology with early emphasis on identifying the most appropriate potential applications within the iron and steel industry as well as the ferroalloy industry. A program should be undertaken to demonstrate the fine particle control capability of HGMS with a pilot-scale device operating on a slipstream of one or more actual industrial processes. Continued research should also be supported to develop and test HGMS system designs specifically oriented toward gas stream applications so that capital costs and power requirements can be minimized and efficient, practical matrix cleaning systems can be demonstrated.

SECTION 9

REFERENCES

1. Oberteuffer, J.A., Magnetic Separation: A Review of Principles, Devices and Applications, IEEE Transactions on Magnetics, Vol. MAG-10, No. 2, June 1974, pp. 223-238.

2. Kolm, H., J. Oberteuffer, and D. Kelland, High Gradient Magnetic Separation, Scientific American, Vol. 233, No. 5, November 1975, pp. 47-53.

3. Luborsky, F.E., High Field-High Gradient Magnetic Separation: A Review, Magnetism and Magnetic Materials--1975, 21st Annual Conference, Philadelphia, American Institute of Physics Conference Proceedings 1976.

4. Oder, R.R., High Gradient Magnetic Separation Theory and Applications, IEEE Transactions on Magnetics, Vol. MAG-12, No. 5, September 1976, pp. 428-435.

5. Iannicelli, J., New Developments in Magnetic Separation, IEEE Transactions on Magnetics, Vol. MAG-12, No. 5, September 1976, pp. 436-443.

6. Franz, S.G., Magnetic Separator, U.S. Patent 2,074,085, March 16, 1937.

7. Jones, G.H., Magnetic Separators, U.S. Patent 3,346,116, October 10, 1967.

8. Oder, R.R., and C.R. Price, Brightness Beneficiation of Kaolin Clays by Magnetic Treatment, The Journal of the Technical Association of the Pulp and Paper Industry, Vol. 56, No. 10, October 1973, pp. 75-78.

9. Oder, R.R., The Magnetic Processing of Kaolin Clay, Pulp and Paper Magazine of Canada, Vol. 75, No. 10, October 1974, pp. T366-T369.

10. Iannicelli, J., Development of High Extraction Magnetic Filtration by the Kaolin Industry of Georgia, IEEE Transactions on Magnetics, Vol. MAG-12, No. 5, September 1976, p. 489.

11. Iammartino, N.R., New Tasks for Magnetism, Chemical Engineering, Vol. 81, No. 1, January 7, 1974, pp. 50-52.

12. Kelland, D.R., High Gradient Magnetic Separation Applied to Mineral Beneficiation, IEEE Transactions on Magnetics, Vol. MAG-9, No. 3, September 1973, pp. 307-310.

13. Lawver, J.E., and D.M. Hopstock, Wet Magnetic Separation of Weakly Magnetic Minerals, Minerals Science Engineering, Vol. 6, No. 3, July 1974, pp. 154-172.

14. Kelland, D.R., and E. Maxwell, Oxidized Taconite Beneficiation by Continuous High Gradient Magnetic Separation, IEEE Transactions on Magnetics, Vol. MAG-11, No. 5, September 1975, pp. 1582-1584.

15. Vives, D.L., L.J. Hirth, and W.H. Summerlin, Direct Reduction and Magnetic Beneficiation of Alabama Brown Ore with Lignite, IEEE Transactions on Magnetics, Vol. MAG-12, No. 5, September 1976, pp. 490-492.

16. Murray, H.H., Beneficiation of Selected Industrial Minerals and Coal by High Intensity Magnetic Separation, IEEE Transactions on Magnetics, Vol. MAG-12, September 1976, pp. 498-502.

17. Ergun, S., and E.H. Bean, Magnetic Separation of Pyrite from Coals, Report of Investigation No. 7181, U.S. Bureau of Mines, Pittsburgh, PA., September 1968.

18. Trindade, S.C., and H.H. Kolm, Magnetic Desulfurization of Coal, IEEE Transactions on Magnetics, Vol. MAG-9, No. 3, September 1973, pp. 310-313.

19. Oder, R.R., Pyritic Sulfur Removal from Coals by High Gradient Magnetic Separation, Proceedings of Second National Conference on Complete WateReuse, 1975, pp. 315-322.

20. Cohen, E. and J.A. Good, The Application of a Superconducting Magnet System to the Cleaning and Desulfurization of Coal, IEEE Transactions on Magnetics, Vol. MAG-12, No. 5, September 1976, pp. 503-506.

21. Maxwell, E., D.R. Kelland, and I.Y. Akoto, High Gradient Magnetic Separation of Mineral Particulates from Solvent Refined Coal, IEEE Transactions on Magnetics, Vol. MAG-12, No. 5, September 1976, pp. 507-510.

22. Lin, C.J., Y.A. Liu, D.L. Vives, M.J. Oak, G.E. Crow, and E.L. Huffman, Pilot-Scale Studies of Sulfur and Ash Removal from Coals by High Gradient Magnetic Separation, IEEE Transactions on Magnetics, Vol. MAG-12, No. 5, September 1976, pp. 513-521.

23. Monteiro, J.L.F., M. Saddy, and S.C. Trindade, Studies on Sulfur Recovery from Coal Wastes and Prospective Magnetic Separation Applications, IEEE Transactions on Magnetics, Vol. MAG-12, No. 5, September 1976, p. 522.

24. Fine, H.A., M. Lowry, L.F. Power, and G.H. Geiger, A Proposed Process for the Desulfurization of Finely Divided Coal by Flash Roasting and Magnetic Separation, IEEE Transactions on Magnetics, Vol. MAG-12, No. 5, September 1976, pp. 523-527.

25. Oder, R.R., Magnetic Desulfurization of Liquefied Coals: Conceptual Process Design and Cost Estimation, IEEE Transactions on Magnetics, Vol. MAG-12, No. 5, September 1976, pp. 532-537.

26. Liu, Y.A., and C.J. Lin, Assessment of Sulfur and Ash Removal from Coals by Magnetic Separation, IEEE Transactions on Magnetics, Vol. MAG-12, No. 5, September 1976, pp. 538-550.

27. Maxwell, E., D.R. Kelland, and I.Y. Akoto, Magnetic Separation of Solids from Liquified Coal, IEEE Transactions on Magnetics, Vol. MAG-12, No. 6, November 1976, p. 907.

28. Kazarian, R., Researchers Developing Method to Remove Impurities From Coal, National Science Foundation News, NSF PR77-50, May 10, 1977, pp. 1-3.

29. Marston, P.G., and J.A. Oberteuffer, The Application of High Gradient Magnetic Separation (HGMS) to the Treatment of Steel Industry Waste Waters, Second International Congress on Industrial Wastes, Stockholm, Sweden, February 1975.

30. Oberteuffer, J.A., I. Wechsler, P.G. Marston and M.J. McNallan, High Gradient Magnetic Filtration of Steel Mill Process and Waste Waters, IEEE Transactions on Magnetics, Vol. MAG-11, No. 5, September 1975, pp. 1591-1593.

31. Oberteuffer, J.A., Engineering Development of High Gradient Magnetic Separators, IEEE Transactions on Magnetics, Vol. MAG-12, No. 5, September 1976, pp. 444-449.

32. Harland, J.R., L. Nilsson and M. Wallin, Pilot-Scale High Gradient Filtration of Steel Mill Wastewater, IEEE Transactions, Vol. MAG-12, No. 6, November 1976, pp. 904-906.

33. deLatour, C., Magnetic Separation in Water Pollution Control, IEEE Transactions on Magnetics, Vol. MAG-9, No. 3, September 1973, pp. 314-316.

34. Oder, R.R., and B.I. Horst, Wastewater Processing with High Gradient Magnetic Separators, Proceedings of Second National Conference on Complete WateReuse, 1975, pp. 887-897.

35. deLatour, C. and H. Kolm, Magnetic Separation in Water Pollution Control-II, IEEE Transactions on Magnetics, Vol. MAG-11, No. 5, September 1975, pp. 1570-1572.

36. Ricci, L.J., Antipollution Processes Top Boston AIChE Meeting, Chemical Engineering, Vol. 82, No. 21, October 13, 1975, pp. 73-75.

37. Petrakis, L. and P.F. Ahnen, Use of High Gradient Magnetic Separation Techniques for the Removal of Oil and Solids from Water Effluents, IEEE Transactions on Magnetics, Vol. MAG-12, No. 5, September 1976, pp. 486-488.

38. Yadidia, R., A. Abeliovich, and G. Belfort, Algae Removal by High Gradient Magnetic Filtration, Environmental Science and Technology Vol. 11, No. 9, September 1977, pp. 913-916.

39. Melville, D., F. Paul, and S. Roath, High Gradient Magnetic Separation of Red Cells from Whole Blood, IEEE Transactions on Magnetics, Vol. MAG-11, No. 6, November 1975, pp. 1701-1704.

40. Kolm, H.H., Research Needs In Magnetic Separation, IEEE Transactions on Magnetics, Vol. MAG-12, No. 5, September 1976, pp. 450-454.

41. Kolm, H.H., The Large-Scale Manipulation of Small Particles, IEEE Transactions on Magnetics, Vol. MAG-11, No. 5, September 1975, pp. 1567-1569.

42. Ranz, W.E. and J.B. Wong, Impaction of Dust and Smoke Particles on Surface and Body Collectors, Industrial and Engineering Chemistry, Vol. 44, No. 6, June 1952, pp. 1371-1381.

43. Davies, C.N., The Separation of Airborne Dust and Particles, Proceedings of the Institute of Mechanical Engineering, Vol. 18, 1952, pp. 185-198.

44. Fuchs, N.A., The Mechanics of Aerosols, Pergamon Press, New York, 1964.

45. Strauss, W., Industrial Gas Cleaning, Pergamon Press, New York, 1966.

46. Loffler, F., Collection of Particles by Fiber Filters, in Air Pollution Control, Part 1, edited by W. Strauss, Wiley-Interscience, New York, 1971.

47. Bean, C.P., Theory of Magnetic Filtration, Bulletin of American Physical Society, Vol. 16, 1971, p. 350. (abstract only)

48. Watson, J.H.P., Magnetic Filtration, Journal of Applied Physics, Vol. 44, No. 9, September 1973, pp. 4209-4213.

49. Oberteuffer, J.A., High Gradient Magnetic Separation, IEEE Transactions on Magnetics, Vol. MAG-9, No. 3, September 1973, pp. 303-306.

50. Oder, R.R. and C.R. Price, HGMS: Mathematical Modeling of Commercial Practice, Magnetism and Magnetic Materials-1975, 21st Annual Conference, Philadelphia, American Institute of Physics Conference Proceedings, 1976.

51. Watson, J.H.P., Theory of Capture of Particles in Magnetic High-Intensity Filters, IEEE Transactions on Magnetics, Vol. MAG-11, No. 5, September 1975, pp. 1597-1599.

52. Cowen, C., F.J. Friedlaender, and R. Jaluria, High Gradient Magnetic Field Particle Capture on a Single Wire, IEEE Transactions on Magnetics, Vol. MAG-11, No. 5, September 1975, pp. 1600-1602.

53. Luborsky, F.E. and B.J. Drummond, High Gradient Magnetic Separation: Theory Versus Experiment, IEEE Transactions on Magnetics, Vol. MAG-11, No. 6, November 1975, pp. 1696-1700.

54. Cummings, D.L., D.A. Himmelblau, J.A. Oberteuffer, and G.J. Powers, Capture of Small Paramagnetic Particles by Magnetic Forces from Low Speed Fluid Flows, AIChE Journal, Vol. 22, No. 3, May 1976, pp. 569-575.

55. Aharoni, A., Traction Force on Paramagnetic Particles in Magnetic Separators, IEEE Transactions on Magnetics, Vol. MAG-12, No. 3, May 1976, pp. 234-235.

56. Luborsky, F.E., and B.J. Drummond, Buildup of Particles on Fibers in a High Field-High Gradient Separator, IEEE Transactions on Magnetics, Vol. MAG-12, No. 5, September 1976, pp. 463-465.

57. Cowen, C., F.J. Friedlaender, and R. Jaluria, Single Wire Model of High Gradient Magnetic Separation Processes I, IEEE Transactions on Magnetics, Vol. MAG-12, No. 5, September 1976, pp. 466-470.

58. Cummings, D.L., D.C. Prieve, and G.J. Powers, The Motion of Small Paramagnetic Particles in a High Gradient Magnetic Separator, IEEE Transactions on Magnetics, Vol. MAG-12, No. 5, September 1976, pp. 471-473.

59. Stekly, Z.J.J. and J.V. Minervini, Shape Effect of the Matrix on the Capture Cross Section of Particles in High Gradient Magnetic Separation, IEEE Transactions on Magnetics, Vol. MAG-12, No. 5, September 1976, pp. 474-479.

60. Birss, R.R., R. Gerber, and M.R. Parker, Theory and Design of Axially Ordered Filters for High Intensity Magnetic Separation, IEEE Transactions on Magnetics, Vol. MAG-12, No. 6, November 1976, pp. 892-894.

61. Uchiyama, S., S. Kondo, M. Takayasu, and I. Eguchi, Performance of Parallel Stream Type Magnetic Filter for HGMS, IEEE Transactions of Magnetics, Vol. MAG-12, No. 6, November 1976, pp. 895-897.

62. Cowen C., F.J. Friedlaender, and R. Jaluria, Single Wire Model of High Gradient Magnetic Separation Processes II, IEEE Transactions on Magnetics, Vol. MAG-12, No. 6, November 1976, pp. 898-900.

63. Clarkson, C.J., D. Kelland, and T.B. King, Model for Calculation of Capture Radii of High Gradient Magnetic Separator at Moderate Reynolds Numbers, IEEE Transactions on Magnetics, Vol. MAG-12, No. 6, November 1976, pp. 901-903.

64. Lawson, W.F., The Dynamics of Paramagnetic Particles Near a Magnetized Wire, M.S. Thesis, Department of Physics, West Virginia University, Morgantown, WV, 1976. (unpublished).

65. Lawson, W.F., W.H. Simons, and R.P. Treat, The Dynamics of a Particle Attracted by a Magnetized Wire, Journal of Applied Physics, Vol. 48, No. 8, August 1977, pp. 3213-3224.

66. Zebel, G., Deposition of Aerosol Flowing Past a Cylindrical Fiber in a Uniform Electric Field, Journal of Colloid Science, 20, 1965, pp. 522-543.

67. Krupp, H., Particle Adhesion, Advances in Colloid and Interface Science, Vol. 1, 1967, pp. 111-239.

68. Ketkar, A., and D.V. Keller, Adhesion of Micron-Sized Limestone Particles to a Massive Coal Substrate, Journal of Adhesion, Vol. 7, 1975, pp. 235-251.

69. Visser, J., On Hamaker Constants: A Comparison between Hamaker Constants and Lifshitz - Van der Waals Constants, Advances in Colloid and Interface Science, Vol. 3, 1972, pp. 331-363.

70. Marks' Standard Handbook for Mechanical Engineers, T. Baumeister, Editor-in-Chief, 7th edition, McGraw-Hill Book Company, New York, 1967.

71. Katari, V., G. Issacs and T.W. Devitt, Trace Pollutant Emissions from the Processing of Metallic Ores, EPA-650/2-74-115, October 1974.

72. Hedley, W.H., S.M. Mehta, C.M. Moscowitz, A.D. Snyder, H.H.S. Yu, and D.L. Zanders, Sources and Characterization of Fine Particulate Test Dusts, EPA-650/2-74-117, November 1974.

73. Dealy, J.O., and A.M. Killin, Engineering and Cost Study of the Ferroalloy Industry, EPA-450/2-74-008, May 1974.

74. Sears, F.W., and M.W. Zemansky, University Physics, Part 2, 3rd edition. Addison-Wesley Publishing Company, Inc., Reading, MA, 1964.

75. Oberteuffer, J.A. and M. Golay, A Review and Analytical Evaluation of the Application of High Gradient Magnetic Separation to Fine Particle Scrubbing, report submitted by Magnetic Engineering Associates under subcontract to Research Triangle Institute, December, 1975.

76. Sala Magnetics, Inc. Cambridge, MA, SMI Bulletin No. D052401-7527GB/775.

77. Guichard, J.C., Aerosol Generation Using Fluidized Beds, in Fine Particles-Aerosol Generation, Measurement, Sampling and Analysis, edited by B.Y.H. Liu, Academic Press, New York, 1976, pp.173-194.

78. Moreno, F. and D. Blann, Large Flow Rate Redispersion Aerosol Generator, in Fine Particles-Aerosol Generation, Measurement Sampling and Analysis, edited by B.Y.H. Liu, Academic Press, New York, 1976, pp. 195-218.

79. Willeke, S., C. Lo, and K.T. Whitby, Dispersion Characteristics of a Fluidized Bed, Aerosol Science, Vol. 5, 1974, pp. 449-455.

80. Ragland, J.W., D.H. Pontius, and W.B. Smith, Design, Construct, and Test a Field Usable Prototype System for Sizing Particles Smaller than 0.5 m Diameter , Special summary report submitted by Southern Research Institute to EPA under Contract No. 69-02-2114, Task 8, EPA Task Officer Bruce Harris, February 1976, (unpublished).

81. Blann, D.D., K.A. Green, and L.W. Anderson, Design, Fabrication, and Installation of a Particulate Aerodynamic Test Facility, EPA-650/2-74-103, October 1974.

82. Gotterba, J., Characterization and Optimization of the EPA High Mass Flowrate Aerosol Generator, Task report submitted by Aerotherm Corporation to EPA under Contract No. 68-02-1318, Task 28, EPA Task Officer Dale Harmon, July 1976, (unpublished).

83. Roulliard, E.E.A., Experimental Errors in Sampling Dust Laden Gas Streams, South African Council for Scientific and Industrial Research, Chemical Engineering Group, CSIR Special Report File No. 66/51/4510/2, Pretoria, December 1971.

84. Harris, D.B., Procedures for Cascade Impactor Calibration and Operation in Process Streams, EPA-600/2-77-004, January 1977.

85. Cushing, K.M., G.E. Lacey, J.D. McCain, and W.B. Smith, Particulate Sizing Techniques for Control Device Evaluations Cascade Impactor Calibrations, EPA-600/2-76-280, October 1976.

86. Hay, R.D., Magnetic Engineering Associates, Inc., Cambridge, MA, Personal communication, April 29, 1976.

87. Oder, R.R., Bechtel Corporation, San Francisco, CA, Personal communication, January 6, 1977.

88. Hardison, L.C. and C.A. Greathouse, Air Pollution Control Technology and Costs in Nine Selected Areas, final report of Industrial Gas Cleaning Institute to EPA under Contract No. 68-02-0301, National Technical Information Service, Springfield, Virginia, PB-222 746, September 1972.

89. Economic Indicators, Chemical Engineering, Vol. 84, No. 19, September 12, 1977, p. 7.

90. Federal Register, March 8, 1974, Vol. 39, p. 9308.

91. Steiner, B.A., Air-Pollution Control in the Iron and Steel Industry, International Metals Review, September 1976.

92. Delaney, E. L., Development Document for Effluent Limitations Guidelines and New Source Performance Standards for the Steel Making Segment of the Iron and Steel Manufacturing Point Source Category, EPA-440/1-74-024a, June 1974.

93. Wechsler, I. Sala Magnetics, Inc., Cambridge, MA, Personal communication, October 18, 1977.

SECTION 10

BIBLIOGRAPHY

1. Allen, J.W., Magnetic Separator, U.S. Patent 3,819,515, June 25, 1974.

2. Aubrey, W.M., J.M. Karpinski, and D.S. Cahn, Magnetic Separator Method and Apparatus, U.S. Patent 3,608,718, September 28, 1971.

3. Davis, C.W.V., Magnetic Separator, U.S. Patent 3,062,376, November 6, 1962.

4. Fraas, F., Alternating Field Magnetic Separator, U.S. Patent 3,988,240, October 26, 1976.

5. Fraas, F., The Matrix-Type Magnetic Separator, Report of Investigation No. 6722, U.S. Bureau of Mines, Pittsburgh, Pennsylvania, 1966.

6. Kolm, H.H., Magnetic Device, U.S. Patent 3,567,026, March 2, 1971.

7. Kolm, H.H., Process for Magnetic Separation, U.S. Patent 3,676,337, July 11, 1972.

8. Marston, P.G., Magnet Design and Its Effect on the Economics of High Gradient Magnetic Separation Processes, Proceedings of the High Gradient Magnetic Separation Symposium, Massachusetts Institute of Technology, Cambridge, Mass., May 1973. pp. 25-37.

9. Marston, P.G., I. Wechsler, and J.J. Nolan, Magnetic Separation Method, U.S. Patent 3,887,457, June 3, 1975.

10. Marston, P.G., and J.J. Nolan, Moving Matrix Magnetic Separator, U.S. Patent 3,920,543, November 18, 1975.

11. Marston, P.G., J.J. Nolan, and L.M. Lontai, Magnetic Separator and Magnetic Separation Method, U.S. Patent 3,627,678, December 14, 1971.

12. Nolan, J.J. and P.G. Marston, Flow Control Unit for Magnetic Matrix, U.S. Patent 4,025,432, May 24, 1977.

13. Nolan, J.J., P.G. Marston, and L.M. Lontai, Multiple Matrix Magnetic Separation Device and Method, U.S. Patent 3,770,629, November 6, 1973.

14. Oder, R.R., Method for Magnetic Beneficiation of Particle Dispersions, U.S. Patent 3,985,646, October 12, 1976.

15. Sakata, S., A. Yoshikawa, and A. Tasaki, Magnetic Separation of Aerosol Particles from Air Flow, Japan Journal of Applied Physics, Vol. 15, No. 10, 1976, pp. 2017-2018.

16. Watson, J.H.P. and D. Hocking, The Beneficiation of Clays Using a Superconducting Magnetic Separator, IEEE Transactions on Magnetics, Vol. MAG-11, No. 5., September 1975, pp. 1588-1590.

APPENDIX

DERIVATION OF THE EQUATIONS OF MOTION FOR A PARAMAGNETIC PARTICLE IN A NONUNIFORM MAGNETOSTATIC FIELD

The energy of a magnetostatic field established in a linear, homogeneous, and isotropic medium where $\vec{B}_o = \mu_o \vec{H}_o$ is given by

$$T_o = \frac{1}{2} \int \vec{H}_o \cdot \vec{B}_o \, d\nu \qquad \text{(A-1)}$$

where T_o = energy, joule
H_o = magnetic field strength, ampere/meter
B_o = magnetic flux density, tesla
μ_o = permeability of free space, $4\pi \times 10^{-7}$ henry/meter.
$d\nu$ = differential volume element.

The indicated integration is extended over all space. If a paramagnetic, spherical particle of volume V_1 (meter^3) and radius R (meter) is placed in the magnetic field, the potential energy is given by

$$U_m = -\frac{1}{2} \int_{V_1} \vec{M} \cdot \vec{B}_o \, d\nu \qquad \text{(A-2)}$$

where U_m = potential energy, joule
M = induced magnetization, ampere/meter.

The integration is over the volume of the particle, and within this volume

$$\vec{B} = \mu_o(\vec{H} + \vec{M}). \qquad \text{(A-3)}$$

The magnetic force F_m (newton) acting upon the paramagnetic particle is given by

$$\vec{F}_m = -\vec{\nabla}U_m = \frac{1}{2}\vec{\nabla}\int_{V_1}\vec{M}\cdot\vec{B}_o\,d\nu \qquad \text{(A-4)}$$

where in cylindrical coordinates

$$\vec{\nabla} = \frac{\partial}{\partial r}\hat{r} + \frac{1}{r}\frac{\partial}{\partial\theta}\hat{\theta} + \frac{\partial}{\partial z}\hat{z} \qquad \text{(A-5)}$$

Interchanging $\vec{\nabla}$ and $\int_{V_1}$ gives

$$\vec{F}_m = \frac{1}{2}\int_{V_1}\vec{\nabla}(\vec{M}\cdot\vec{B}_o)d\nu \qquad \text{(A-6)}$$

According to equation (A-3)

$$\vec{B} = \mu_o(\vec{H}+\vec{M}) = \mu\vec{H} \qquad r<R \qquad \text{(A-7)}$$

where $\mu = \mu_o\left(1 + \frac{|\vec{M}|}{|\vec{H}|}\right)$. (A-8)

Thus $\vec{M} = \left(\frac{\mu}{\mu_o} - 1\right)\vec{H} = \chi\vec{H}$ (A-9)

where $\chi = \frac{\mu}{\mu_o} - 1$. (A-10)

In the linear, homogeneous, and isotropic medium

$$\vec{B}_o = \mu_o\vec{H}_o \qquad r>>R \qquad \text{(A-11)}$$

and equation (A-6) then becomes

$$\vec{F}_m = \frac{1}{2}\int_{V_1} \vec{\nabla}(\chi\vec{H}) \cdot (\mu_o\vec{H}_o)d\nu = \frac{1}{2}\chi\mu_o\int_{V_1} \vec{\nabla}(\vec{H} \cdot \vec{H}_o)d\nu. \qquad \text{(A-12)}$$

The dielectric constant, μ, and the susceptibility, χ, are properties of the particle, which is also assumed to be linear, isotropic, and homogeneous. If the value of $\vec{H}$ is assumed to be relatively constant throughout the volume V_1 and approximately equal to $\vec{H}_o$, the integration can be performed to yield

$$\vec{F}_m = \frac{1}{2}\chi\mu_o\vec{\nabla}(\vec{H}_o \cdot \vec{H}_o)\int_{V_1} d\nu \qquad \text{(A-13)}$$

and finally,

$$\vec{F}_m = \frac{1}{2}\chi\mu_o\left(\frac{4}{3}\pi R^3\right)\vec{\nabla}(\vec{H}_o \cdot \vec{H}_o). \qquad \text{(A-14)}$$

The magnetic field of interest is a combination of the uniform background field $\vec{H}_o$ and the nonuniform field in the vicinity of a ferromagnetic wire. The geometric arrangement shown in Figure A-1 will be used to obtain the appropriate expression for the magnetic field strength.

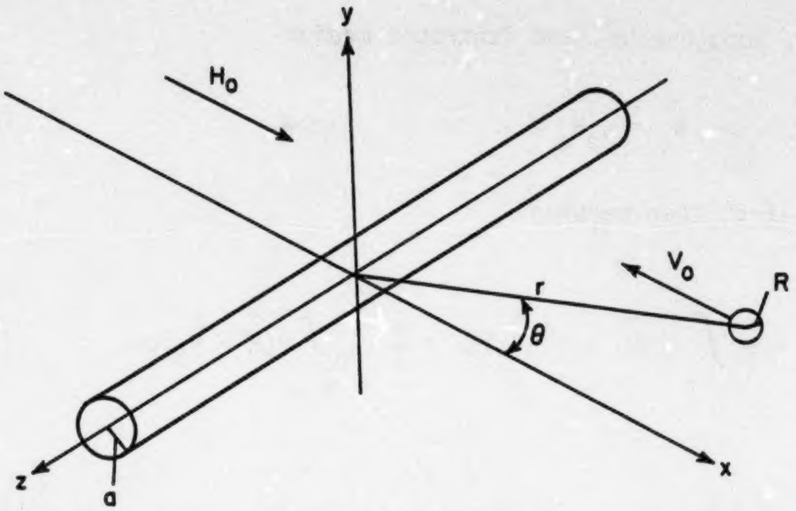

Figure A-1. Coordinate system for HGMS single-fiber model.

The radius of the cylindrical ferromagnetic wire is a (meter), and the radius of the spherical particle is R (meter). For r>>a the velocity of the particle is V_0 and parallel to but in the negative x direction. For r>>a, the magnetic field strength is H_0 and parallel to and in the positive x direction.

Since the magnetic field strength is a vector, we may define a magnetic potential Φ such that

$$\vec{H} = -\vec{\nabla}\,\Phi. \qquad \text{(A-15)}$$

As stated before for a linear, isotropic, and homogeneous medium,

$$\vec{B} = \mu\vec{H}. \qquad \text{(A-16)}$$

The magnetic flux density B is solenoidal, hence

$$\vec{\nabla} \cdot \vec{B} = 0. \qquad \text{(A-17)}$$

Introducing Equations (A-15) and (A-16) into (A-17) yields

$$\vec{\nabla} \cdot \mu\vec{H} = -\mu\vec{\nabla} \cdot \vec{\nabla}\, \Phi = -\mu\nabla^2\, \Phi = 0, \qquad \text{(A-18)}$$

where in cylindrical coordinates

$$\nabla^2\Phi = \frac{\partial^2\Phi}{\partial r^2} + \frac{1}{r}\,\frac{\partial\Phi}{\partial r} + \frac{1}{r^2}\,\frac{\partial^2\Phi}{\partial\theta^2} + \frac{\partial\ \Phi}{\partial z^2} = 0. \qquad \text{(A-19)}$$

Due to symmetry, $\frac{\partial^2\Phi}{\partial r^2} = 0$; and we are left with

$$\frac{\partial^2\Phi}{\partial r^2} + \frac{1}{r}\,\frac{\partial\Phi}{\partial r} + \frac{1}{r^2}\,\frac{\partial^2\Phi}{\partial\theta^2} = 0. \qquad \text{(A-20)}$$

A solution of the form

$$\Phi = r^n C_n(\theta) + r^{-n} C_n(\theta) \qquad \text{(A-21)}$$

can be shown to satisfy the partial differential equation where $C_n(\theta)$ are harmonic functions given by

C_n	$r^{-n}C_n(\theta)$	$r^n Cos_n(\theta)$
C_0	$\log r$	1
C_1	$r^{-1}(A_1 Cos\ \theta + B_1 Sin\ \theta)$	$r(A_2 Cos\ \theta + B_2 Sin\ \theta)$
C_2	$r^{-2}(A_1 Cos\ 2\theta + B_1 Sin\ 2\theta)$	$r^2(A_2 Cos\ 2\theta + B_2 Sin\ 2\theta)$
C_3	$r^{-3}(A_1 Cos\ \theta + B_1 Sin\ 3\theta)$	$r^3(A_2 Cos\ 3\theta + B_2 Sin\ 3\theta)$

where A_1, A_2, B_1, and B_2 are constants.

Inside the wire the magnetic potential is $\Phi_1(r, \theta)$. If only first order harmonic functions are considered and the origin is chosen as zero potential where $\Phi_1(0,0) = 0$, then the r^{-1} terms must disappear and the potential is given by

$$\Phi_1(r, \theta) = r(A\ Cos\ \theta + B\ Sin\ \theta) \qquad \text{(A-22)}$$

and

$$\vec{H}_1(r, \theta) = -(A\ Cos\ \theta + B\ Sin\ \theta)\hat{r} - (-A\ Sin\ \theta + B\ Cos\ \theta)\hat{\theta}. \qquad \text{(A-23)}$$

At the boundary of the wire the tangential component H_θ of $\vec{H}$ is zero for $\theta=0$. Evaluating $H_{1,\theta}(a,0)$ from Equation (A-23) yields

$$H_{1,\theta}(a,0) = -B = 0. \tag{A-24}$$

Therefore Equation (A-22) becomes

$$\Phi_1(r,\theta) = rA \operatorname{Cos} \theta. \tag{A-25}$$

Outside the wire the first order approximation for the magnetic potential is given by

$$\Phi_2(r,\theta) = r^{-1}(C \operatorname{Cos} \theta + D \operatorname{Sin} \theta) + r\,(E \operatorname{Cos} \theta + F \operatorname{Sin} \theta) \tag{A-26}$$

and

$$\begin{aligned}\vec{H}_2(r,\theta) = &-\left[-\frac{1}{r^2}(C \operatorname{Cos} \theta + D \operatorname{Sin} \theta) + (E \operatorname{Cos} \theta + F \operatorname{Sin} \theta)\right]\hat{r} \\ &-\left[r^{-1}(-C \operatorname{Sin} \theta + D \operatorname{Cos} \theta) + (-E \operatorname{Sin} \theta + F \operatorname{Cos} \theta)\right]\hat{\theta}.\end{aligned} \tag{A-27}$$

Outside the wire where $r \gg a$

$$\vec{H}_2(r,0) \to H_0\hat{r}. \tag{A-28}$$

Therefore,

$$H_{2,r}(r,0) = H_0 \qquad r \gg a \tag{A-29}$$

$$H_{2,\theta}(r,0) = 0 \qquad r \gg a. \tag{A-30}$$

Evaluating $H_{2,r}(r,0)$ and $H_{2,\theta}(r,0)$ from Equation (A-27) yields

$$H_{2,r}(r,0) = +\frac{C}{r^2} - E = H_o \qquad r>>a. \tag{A-31}$$

$$\therefore \; E = -H_o. \tag{A-32}$$

Also

$$H_{2,\theta}(r,0) = -\frac{D}{r} - F = 0 \qquad r>>a. \tag{A-33}$$

By choosing F = D = 0, the boundary condition $H_{2,\theta}(r,0) = 0$ is satisfied and Equation (A-26) becomes

$$\Phi_2(r,\theta) = r^{-1}C \operatorname{Cos}\theta - rH_o \operatorname{Cos}\theta. \tag{A-34}$$

Other information necessary to specify A in Equation (A-25) and C in Equation (A-34) is obtained from analysis of the conditions at the boundary of the ferromagnetic wire. Throughout the ferromagnetic wire the magnetization is parallel and in the positive x direction. Thus the tangential component M_t and normal component M_n are related to M by

$$\vec{M} = M_n\hat{r} + M_t\,\hat{\theta} \tag{A-35}$$

$$M_n = |\vec{M}| \;\operatorname{Cos}\theta \tag{A-36}$$

$$M_t = |\vec{M}| \operatorname{Sin}\theta. \tag{A-37}$$

It can be easily shown that the normal components of the magnetic flux density across the boundary of the wire must be equal or

$$B_{n1} = B_{n2} \cdot \tag{A-38}$$

Inside the wire

$$B_{n1} = \mu_o(H_{n1} + M_n) = - \mu \left. \frac{\partial \Phi_1}{\partial r} \right|_{r=a} . \tag{A-39}$$

Outside the wire

$$B_{n2} = \mu_o H_{n2} = -\mu \left. \frac{\partial \Phi_2}{\partial r} \right|_{r=a} . \tag{A-40}$$

In addition, the tangential components of the magnetic field strength must be continuous and equal across the boundary of the wire or

$$H_{t1} = H_{t2} \cdot \tag{A-41}$$

Inside the wire

$$H_{t1} = H_{1,\theta} = - \frac{1}{r} \left. \frac{\partial \Phi_1}{\partial \theta} \right|_{r=a} . \tag{A-42}$$

Outside the wire

$$H_{t2} = H_{2,\theta} = - \frac{1}{r} \left. \frac{\partial \Phi_2}{\partial \theta} \right|_{r=a} . \tag{A-43}$$

Equations (A-38) and (A-41) with the substitutions indicated by Equations (A-39), (A-40), (A-42), and (A-43) are solved to yield values for A and C so that the equations for the magnetic potential finally become

$$\Phi_1 = (-H_o + \frac{M}{2}) r \text{ Cos } \theta \tag{A-44}$$

and

$$\Phi_2 = \frac{a^2 M}{2r} \text{ Cos } \theta - H_o r \text{ Cos } \theta . \tag{A-45}$$

To determine the force on the particle in the magnetic field, we need the magnetic field outside the wire or

$$\vec{H}_2 = - \vec{\nabla}\Phi_2 \tag{A-46}$$

where

$$\vec{H}_2 = \frac{\partial\Phi_2}{\partial r} \hat{r} + \frac{1}{r} \frac{\partial\Phi_2}{\partial\theta} \hat{\theta} + \frac{\partial\Phi_2}{\partial z} \hat{z} \tag{A-47}$$

or

$$\vec{H}_2 = \left(\frac{a^2 M}{2r^2} \text{ Cos } \theta + H_o \text{ Cos } \theta\right)\hat{r} - \frac{1}{r}\left(-\frac{a^2 M}{2r} \text{ Sin } \theta + H_o r \text{ Sin } \theta\right)\hat{\theta} . \tag{A-48}$$

Recall that

$$\vec{F}_m = \frac{1}{2} \chi \mu_o \left(\frac{4}{3} \pi R^3\right) \vec{\nabla}(\vec{H}_2 \cdot \vec{H}_2) \tag{A-14}$$

or

$$\vec{F}_m = (F_r \hat{r} + F_\theta \hat{\theta}) . \tag{A-49}$$

Performing the appropriate operations with the results from Equations (A-44) and (A-45) yields

$$F_r = -\chi\mu_o(\frac{4}{3}\pi R^3)\frac{a^2M}{r^3}(\frac{a^2M}{2r^2} + H_o \text{ Cos } 2\theta) \quad \text{(A-50)}$$

and

$$F_\theta = -\chi\mu_o(\frac{4}{3}\pi R^3)\frac{a^2MH_o \text{ Sin } 2\theta}{r^3} . \quad \text{(A-51)}$$

The equation of motion for the particle in the air stream and in the magnetic field can be obtained for the coordinate system established in Figure A-1.

The air stream velocity has components

$$\vec{V}_o = V_{or}\hat{r} + V_{o\theta}\hat{\theta} \quad \text{(A-52)}$$

where assuming potential flow,

$$V_{or} = -V_o(1 - \frac{a^2}{r^2}) \text{ Cos } \theta \quad \text{(A-53)}$$

and

$$V_{o\theta} = V_o(1 + \frac{a^2}{r^2}) \text{ Sin } \theta . \quad \text{(A-54)}$$

The Lagrangian form of the equation of motion in cylindrical coordinates is

$$\left[m\frac{d^2r}{dt^2} - m\,r\left(\frac{d\theta}{dt}\right)^2\right]\hat{r} + \left[m\,r\frac{d^2\theta}{dt^2} + 2\,m\frac{dr}{dt}\frac{d\theta}{dt}\right]\hat{\theta} = \vec{F}_a + \vec{F}_m \quad \text{(A-55)}$$

where $\vec{F}_a$ are the aerodynamic forces and $\vec{F}_m$ are the magnetic forces. The aerodynamic forces are assumed to be adequately expressed by Stokes law

$$\vec{F}_a = 6 \pi \eta R \vec{V} \qquad \text{(A-56)}$$

where $\vec{V}$ is the relative velocity of the fluid and the particle. Substituting for the aerodynamic and magnetic forces and rearranging yields for the radial component $(\hat{r})$

$$\frac{(\frac{4}{3} \pi R^3)\rho_p}{6 \pi \eta R}\left[a\frac{d^2(\frac{r}{a})}{dt^2} - r(\frac{d\theta}{dt})^2\right] + a\frac{d(\frac{r}{a})}{dt}$$

$$= V_o\left[1 - \frac{1}{(\frac{r}{a})^2}\right]\text{Cos } \theta - \frac{\chi\mu_o(\frac{4}{3} \pi R^3)M}{6 \mu \eta Ra(\frac{r}{a})^3}\left[\frac{M}{2(\frac{r}{a})^2} + H_o \text{ Cos } 2\theta\right] \qquad \text{(A-57)}$$

where ρ_p is the particle density.

Defining $r_a = \frac{r}{a}$ and

$$\left(\frac{V_m}{a}\right) = \frac{2}{9}\left[\frac{\chi \mu_o M H_o R^2}{\eta a^2}\right], \qquad \text{(A-58)}$$

Equation (A-57) can be rearranged to

$$\frac{2 \rho_p R^2}{9\eta}\left[\frac{d^2 r_a}{dt^2} - r_a(\frac{d\theta}{dt})^2\right] + \frac{dr_a}{dt}$$

$$= \frac{V_o}{a}(1 - \frac{1}{r_a^2}) \text{ Cos } \theta - \frac{V_m}{a}\frac{1}{r_a^3}\left(\frac{M}{2 H_o r_a{}^2} + \text{Cos } 2 \theta\right). \qquad \text{(A-59)}$$

Correspondingly, the angular component $(\hat{\theta})$ is given by

$$\frac{2\,\rho_p\,R^2}{9\,\eta}\left[r_a\frac{d^2\theta}{dt^2} + 2\left(\frac{dr_a}{dt}\right)\left(\frac{d\theta}{dt}\right)\right] + r_a\,\frac{d\theta}{dt} = - \frac{V_o}{a}\left(1 + \frac{1}{r_a^2}\right)\text{Sin}\,\theta - \frac{V_m}{a}\,\frac{\text{Sin}\,2\theta}{r_a^3}\,. \tag{A-60}$$

Equations (A-59) and (A-60) constitute the equations of motion for a paramagnetic particle under the influence of inertial, viscous, and magnetic forces.